TAMPEREEN TEKNILLINEN YLIOPISTO
TAMPERE UNIVERSITY OF TECHNOLOGY

Erman Acar

Statistical Reconstruction Methods for 3D Imaging of Biological Samples with Electron Microscopy

Julkaisu 1545 • Publication 1545

Tampere 2018

Tampereen teknillinen yliopisto. Julkaisu 1545
Tampere University of Technology. Publication 1545

Erman Acar

Statistical Reconstruction Methods for 3D Imaging of Biological Samples with Electron Microscopy

Thesis for the degree of Doctor of Science in Technology to be presented with due permission for public examination and criticism in Tietotalo Building, Auditorium TB109, at Tampere University of Technology, on the 18th of May 2018, at 12 noon.

Tampereen teknillinen yliopisto - Tampere University of Technology
Tampere 2018

Doctoral candidate: Erman Acar, M.Sc.
Laboratory of Signal Processing
Faculty of Computing and Electrical Engineering
Tampere University of Technology
Finland

Supervisors: Ulla Ruotsalainen, Professor
Laboratory of Signal Processing
Faculty of Computing and Electrical Engineering
Tampere University of Technology
Finland

Sari Peltonen, University Lecturer
Laboratory of Signal Processing
Faculty of Computing and Electrical Engineering
Tampere University of Technology
Finland

Pre-examiners: Lasse Lensu, Professor
Machine Vision and Pattern Recognition Laboratory
School of Engineering Science
Lappeenranta University of Technology
Finland

Jose Maria Carazo, Professor
Spanish National Bioinformatics Institute
National Center for Biotechnology
Autonomous University of Madrid
Spain

Opponent: Peter Horvath, Professor
Institute for Molecular Medicine
University of Helsinki
Finland

ISBN 978-952-15-4134-6 (printed)
ISBN 978-952-15-4141-4 (PDF)
ISSN 1459-2045

Abstract

Electron microscopy has emerged as the leading method for the in vivo study of biological structures such as cells, organelles, protein molecules and virus like particles. By providing 3D images up to near atomic resolution, it plays a significant role in analyzing complex organizations, understanding physiological functions and developing medicines. The 3D images representing the electrostatic potential distribution are reconstructed by utilizing the 2D projection images of the target acquired by electron microscope. There are two main 3D reconstruction techniques in the field of electron microscopy: electron tomography (ET) and single particle reconstruction (SPR). In ET, the projection images are acquired by rotating the specimen for different angles. In SPR, the projection images are obtained by analyzing the images of multiple objects representing the same structure. Then, the tomographic reconstruction methods are applied in both methods to obtain the 3D image through the 2D projections.

Physical and mechanical limitations can prevent to acquire projection images that cover the projection angle space completely and uniformly. Incomplete and non-uniform sampling of the projection angles results in anisotropic resolution in the image plane and generates artifacts. Another problem is that the total applied dose of electrons is limited in order to prevent the radiation damage to the biological target. Therefore, limited number of projection images with low signal to noise ratio can be used in the reconstruction process. This affects the resolution of the reconstructed image significantly. This study presents statistical methods to overcome these major challenges to obtain precise and high resolution images in electron microscopy.

Statistical image reconstruction methods have been successful in recovering a signal from imperfect measurements due to their capability of utilizing a priori information. First, we developed a sequential application of a statistical method for ET. Then we extended the method to support projection angles freely distributed in 3D space and applied the method in SPR. In both applications, we observed the strength of the method in projection gap filling, robustness against noise, and resolving the high resolution details in comparison with the conventional reconstruction methods. Afterwards, we improved the method in terms of computation time by incorporating multiresolution reconstruction. Furthermore, we developed an adaptive regularization method to minimize the parameters required to be set by the user. We also proposed the local adaptive Wiener filter for the class averaging step of SPR to improve the averaging accuracy.

The qualitative and quantitative analysis of the reconstructions with phantom and experimental datasets has demonstrated that the proposed reconstruction methods outperform the conventional reconstruction methods. These statistical approaches provided better image accuracy and higher resolution compared with the conventional algebraic and transfer domain based reconstruction methods. The methods provided in this study contribute to enhance our understanding of cellular and molecular structures by providing 3D images of those with improved accuracy and resolution.

Preface

This study has been carried out at the Signal Processing Laboratory of Tampere University of Technology.

I owe my deepest gratitude to my supervisors Prof. Ulla Ruotsalainen and Sari Peltonen for their support and guidance during the studies.

I would like to thank Prof. Holland Cheng, Dr. Toshio Moriya, Dr. Lassi Paavolainen, M.Sc. Ali Abdollahzadeh, Dr. Uygar Tuna, and Mo A. Baikoghli for their collaboration and contribution.

I express my sincere thanks to the pre-examiners Prof. Lasse Lensu and Prof. Jose Maria Carazo for their valuable comments.

The financial support provided by the TekesFiDiPro and Finnish Cultural Foundation is gratefully acknowledged.

Tampere 14.3.2018

Erman Acar

List of Symbols and Abbreviations

a_{db}	the contribution of the b^{th} voxel to the d^{th} projection data
β	regularization parameter
$\delta(\,)$	Dirac delta function
$F()$	Fourier transform
$\mathrm{med}()$	median filtering
p_d	d^{th} projection data
v_b	the random number of electrons scattered inside the b^{th} voxel
λ_b	mean of the b^{th} voxel value, v_b
λ_d	mean of the d^{th} projection data, p_d

1D, 2D, 3D	One, two, three dimensional
aMAPEM	Adaptive maximum a posteriori probability expectation maximization
amMAPEM	Adaptive multiresolution maximum a posteriori probability expectation maximization
ART	Algebraic reconstruction technique
CCD	Charge coupled device
CR	Contrast ratio
CTF	Contrast transfer function
DF	Direct Fourier inversion
EM	Electron microscopy
ET	Electron tomography
FBP	Filtered back projection
FR	Fourier reconstruction
FRC	Fourier ring correlation
FSC	Fourier shell correlation
FSMSE	Fourier shell mean squared error
FWHM	Full width at half maximum
HEVLP	Hepatitis E virus like particle
laWF	Local adaptive Wiener filter
MAPEM	Maximum a posteriori probability expectation maximization
MLEM	Maximum likelihood expectation maximization
mMAPEM	Multiresolution maximum a posteriori probability expectation maximization
MRP	Median root prior
MSE	Mean squared error
NCC	Normalized cross correlation
NLOO	Noise compensated leave one out
NMSD	Normalized mean squared difference
PET	Positron emission tomography
PSF	Point spread function
SIRT	Simultaneous iterative reconstruction technique

sMAPEM	Sequential maximum a posteriori probability expectation maximization
SNR	Signal to noise ratio
SPECT	Single photon emission computed tomography
SPR	Single particle reconstruction
STEM	Scanning transmission electron microscopy
TEM	Transmission electron microscope
VLP	Virus like particle
WBP	Weighted back projection
WF	Wiener filter

Contents

List of Included Publications

This thesis is a compound thesis and is based on the following publications. The articles are reprinted with the permission of the copyright holders.

P1 L. Paavolainen*, E. Acar*, U. Tuna, S. Peltonen, T. Moriya, P. Soonsawad, V. Marjomäki, R. H. Cheng, and U. Ruotsalainen, **"Compensation of missing wedge effects with sequential statistical reconstruction in electron tomography"**, PLoS One, vol. 9, no. 10, p. e108978, October 2014 (*:equal contribution).

P2 T. Moriya, E. Acar, R. H. Cheng, and U. Ruotsalainen, **"A Bayesian approach for suppression of limited angular sampling artifacts in single particle 3D reconstruction"**, Journal of Structural Biology, vol. 191, no. 3, pp. 318–31, June 2015.

P3 E. Acar, S. Peltonen, and U. Ruotsalainen, **"Adaptive multiresolution method for MAP reconstruction in electron tomography"**, Ultramicroscopy, vol. 170, pp. 24–34, August 2016.

P4 E. Acar, M. A. Baikoghli, M. Stark, S. Peltonen, U. Ruotsalainen, R. H. Cheng, "**Multiresolution MAPEM Method for 3D Reconstruction of Symmetrical Particles in Electron Microscopy"**, In: Eskola H., Väisänen O., Viik J., Hyttinen J. (eds) EMBEC & NBC 2017. IFMBE Proceedings, vol 65. Springer, Singapore.

P5 A. Abdollahzadeh*, E. Acar*, S. Peltonen, and U. Ruotsalainen, "**Local adaptive wiener filtering for class averaging in single particle reconstruction**", In: Sharma P., Bianchi F. (eds) Image Analysis. SCIA 2017. Lecture Notes in Computer Science, vol 10270. Springer, Cham. (*:equal contribution)

Chapter 1

Introduction

3D images of biological samples play an important role in developing effective vaccines and antivirals against the related diseases. Improving the accuracy and resolution of these images enhances our understanding of the mechanisms of virus assembly and entry to the target cell. Electron microscopy (EM) is the leading technology to obtain high resolution 3D images of the biological organisms to investigate their structure and function in their native context. The 3D images reconstructed using EM enable taking cross sections through any selected region and analyzing the internal structure of the target slice by slice. Electron tomography (ET) and single particle reconstruction (SPR) are the two major EM techniques that reconstruct 3D images from the 2D projections. The methods suffer from the missing projection images, low signal to noise ratio of the images, uneven distribution of the projection angles, and the imprecise projection angles. These problems are explained in more detail by demonstrating the methods to handle these challenges in the following subsections.

1.1. Electron Tomography

In electron tomography, 2D projection images of the target are acquired with transmission electron microscope (TEM) from different angles of view. Typically, the specimen is rotated around a single axis with fixed 1−2° angular intervals [1]. For each angle, a projection image is acquired as it is shown in Figure 1-1 and these images are used to reconstruct the sample in 3D afterwards.

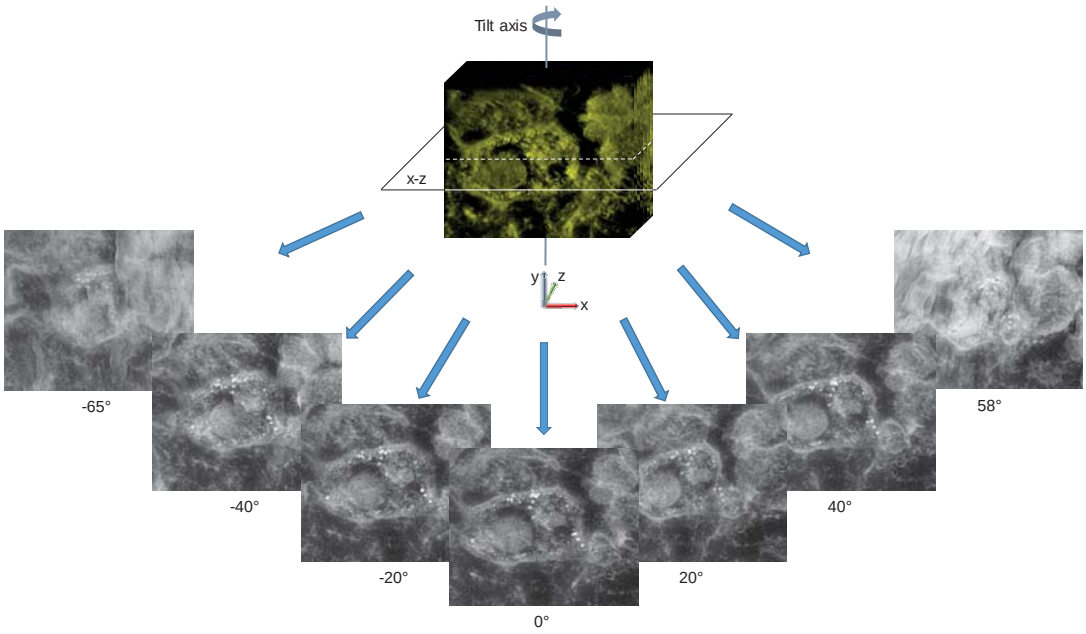

Figure 1-1. Data acquisition with single tilt axis geometry. The specimen is rotated around the single tilt axis (y-axis).

1.1.1. Sample Preparation

The specimen requires special treatment before imaging in order to protect it from the radiation and high vacuum conditions in the electron microscope. Rapid freezing of the specimen has been the most preferred preparation technique since it provides the best structure preservation among the other techniques. Due to the rapid freezing, ice is kept in vitreous state without being crystalized. This helps avoiding the damage due to crystallization. If a thin sample (<500 nm) is used, as it is the case in small bacteria, virus etc. imaging, the sample is submerged into liquid ethane or propane. Then the sample is directly placed in a microscope that is capable of keeping the sample cold. If a thick sample (500 nm–200 μm) is used, as it is the case in bacteria, eukaryotic cell, tissue etc. imaging, the bulk specimen is frozen by using high pressure freezing techniques. Then, the thin sections are cut from the frozen specimen and placed in the electron microscope. In addition to cryo based preparation techniques, there are also staining techniques to protect the specimen. However, these techniques are not preferable especially when high resolution is desired, since staining limits the maximum attainable resolution.

1.1.2. Data Acquisition

The structure of the sample holder and mechanical restrictions prevent tilting the specimen beyond ±60-70°. Moreover, at the high tilt angles, the electrons have to travel longer path than in the zero tilt case due to the slab shaped structure. This reduces the quality of the images at high tilt angle. Therefore, the projections cannot be acquired in the complete 180° tilt angle range.

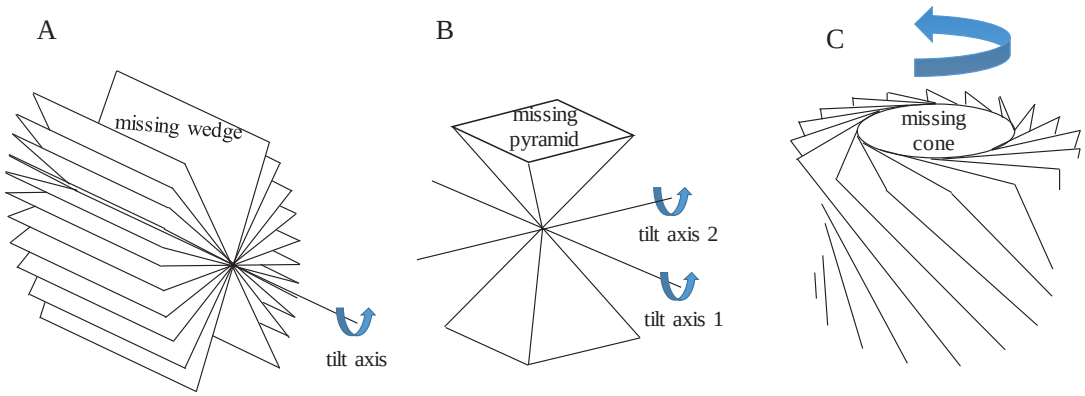

Figure 1-2. A. Single tilt axis data acquisition B. Double tilt axis data acquisition C. Conical tilt axis data acquisition

The missing projection data results in elongated images of the objects in the electron beam direction. This problem is referred to as the 'missing wedge problem' due to the shape of the missing information in the Fourier space (Figure 1-2 A). In order to reduce the missing information, double tilt axis [1-2] and conical tilt axis [4] data acquisition have been proposed. In double tilt case, the specimen is rotated 90 degrees and a second tilt series is acquired around the second tilt axis perpendicular to the first acquisition (Figure 1-2 B). As a result, the missing wedge is reduced to a missing pyramid. In the conical tilt case, the specimen is tilted to its maximum position and then rotated to complete a 360° turn acquisition (Figure 1-2 C). This way the missing information is reduced to a missing cone shape in frequency domain. However, double tilt and conical tilt axis data acquisition have not been as widespread as the single tilt case since they are technically more demanding and they require more complicated projection image alignment methods before the reconstruction.

1.1.3. Image Formation with Electron Microscope

The electron microscope can be operated in different modes to utilize different contrast mechanisms during the formation of the microscope image. For example, the scattered electrons are detected to form the image in the dark field imaging mode. However, detection of the transmitted electrons plays the major role in the in bright field imaging mode. The bright field mode is used more conventionally compared with the dark field mode in the electron microscopy for life sciences. In the bright field imaging mode, the specimen is illuminated by a parallel beam of electrons accelerated under high voltage. The electrons passing through the specimen and the objective aperture form the image in the back focal plane.

There are two image contrast mechanisms, namely amplitude contrast and phase contrast, in the image formation process. The amplitude contrast is generated mainly due to the electrons blocked from reaching the detector. The phase contrast is generated due to the phase shift arising from the electron specimen interaction [5].

1.1.4. Alignment of Projection Images

Alignment of the projections plays an important role in reconstructing high resolution images from TEM tilt series. The inaccuracy of the projection angles decreases the resolution of the reconstructed image and introduces artifacts and blur to the image. Although the automated data acquisition procedures provide the geometric relationship between the sample and its projections coarsely, a more accurate alignment is still needed afterwards [6], [7]. The purpose of projection alignment is to estimate this relationship more precise than the initially provided mechanical values. The projections can be aligned by using either a marker based or a markerless approach.

In the marker based approach, colloidal gold particles are spread over the specimen in the preparation stage. Since these particles are denser than the surrounding tissue, it is easy to detect and use them as reference points in the projection images. First, the projection images are aligned coarsely by using cross-correlation between consecutive images. Then the gold particles are detected and tracked automatically in each projection image for finer alignment [8], [9]. Although high contrast gold particle images provide easily detectable and robust feature points, they generate artifacts in the reconstructions occluding the surrounding biological tissue. In order to compensate these artifacts, Song et al. presented different types of interpolation methods for the neighborhood of the gold particles [10].

Even though marker based approaches provide accurate and robust alignment of projections, in some cases it is not possible or preferable to use gold particles. In these cases, the cross correlation between the consecutive projection images can be used for translational alignment [6]. In a different approach, instead of using the whole projection image, automatically extracted feature points are tracked to find the alignment parameters [9], [11]. The accuracy of this approach depends on the feature point detection precision. Errors are more tolerable if high number of feature points is used. The third approach to the alignment problem uses the whole 3D volume and iteratively refines the translation and rotation parameters of the alignment. In this approach, first the projections are aligned coarsely with cross correlation method. Then the 3D volume is reconstructed with this initial alignment. The virtual projections from the reconstructed volume are compared with the measured projections and the alignment parameters are updated according to this comparison. This procedure is repeated until the geometry providing the measured projections is obtained [12]. Although this approach is computationally expensive, it provides robust alignment especially for the cases mentioned above that the other approaches are not applicable.

1.1.5. Tomographic Image Reconstruction

Tomographic reconstruction is the mathematical procedure to visualize the internal structure of targets in 3D using their 2D projections. This enables analyzing the target by taking cross sectional images through the 3D volume. In the single tilt axis geometry, the reconstructed volume

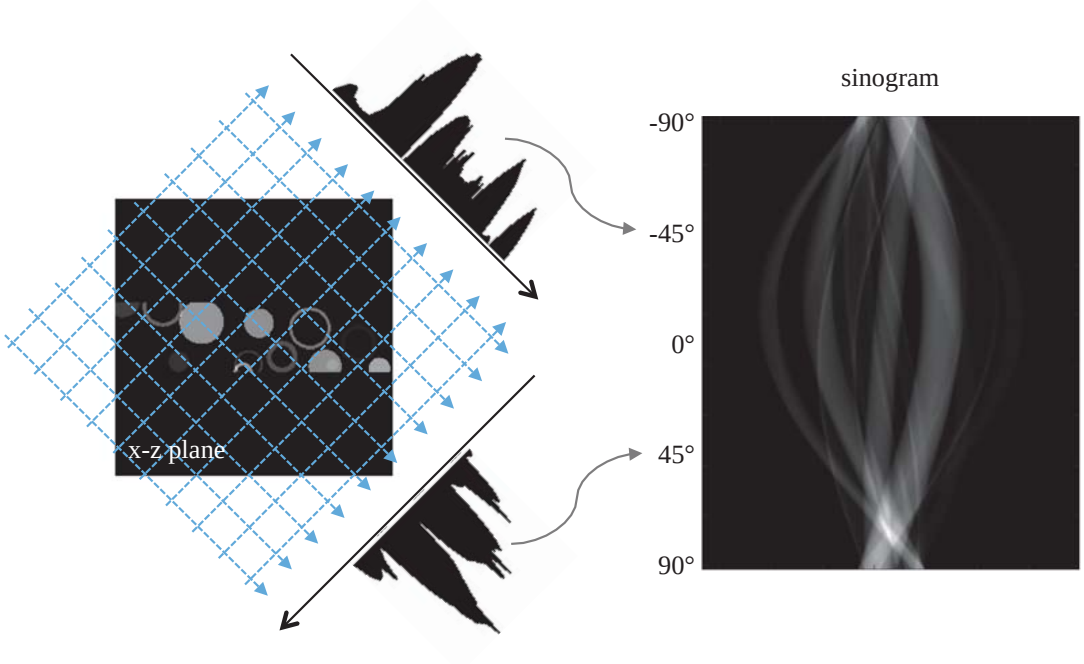

Figure 1-3. The construction of sinogram is illustrated.

can be decomposed into 2D slices and each slice can be reconstructed independently using parallel processing techniques. The projection data is organized as a stack for different projection angles. This stack is called sinogram. The construction of sinogram data is illustrated in Figure 1-3. In this case, the problem is reduced to 2D reconstruction from 1D projections. A large number of well established methods are available for this reduced problem. However, in the double tilt ET, conical tilt ET and SPR cases, more sophisticated reconstruction algorithms are required to support projection angles distributed freely in the 3D space. These algorithms are computationally intensive in general. The tomographic reconstruction algorithms will be explained in detail in Chapter 2 focusing on the methods conventionally used in the field of electron microscopy.

1.1.6. Noise Reduction

Several strategies have been proposed to reduce the noise in the reconstructions. Noise can be filtered from the projections before reconstruction or filtering can be applied to the reconstructed 3D volume. Classical low pass filtering techniques have been frequently used for noise reduction in ET. These filters smooth the data while suppressing the high frequencies. This yields loss of resolution and contrast in the reconstructed volumes. More sophisticated filters should be designed such that they preserve edges while smoothing the noise. For that purpose, noise and the actual signal should be discriminated. A simple approach to this discrimination is based on the assumption that the signal contains features spread over the neighboring regions whereas noise does not. Therefore, the similarity between the neighboring pixels has been widely utilized in noise reduction. Wavelet filters used wavelet basis functions to measure this proximity for different scales

and locations [13]. Bilateral filtering replaces each pixel with a weighted average of its neighbors using weights reflecting the similarity in terms of the density information in addition to the spatial relationship [14]. Nonlinear anisotropic diffusion filter uses the gradient of the image to detect edges and applies smoothing to the edge-free regions more than the edge regions [15]. The disadvantage of these filters is their parameter dependency. A parameter independent filter widely used in tomographic reconstruction is the median filter. It replaces each pixel with the median value in a small neighborhood [16]. It has been shown that it preserves edges better than the standard low pass filters [17].

1.2. Single Particle Reconstruction

Single particle reconstruction is a technique to obtain high-resolution images of macromolecular structures such as proteins or viruses by analyzing their images acquired with TEM. The applied dose of electrons with TEM is limited in order to prevent the radiation damage to the biological target. Therefore, the images of the particles usually have a very poor SNR. The technique merges several images of the particle with the same view to obtain an image with higher quality. Once the images are obtained with the estimated angles of view, the particle can be reconstructed in 3D to reveal the internal structure with the tomographic reconstruction methods.

1.2.1. Sample Preparation

The preparation of the sample starts with the purification of the protein structure. Then the purified protein solution is applied to a grid of tiny holes in a carbon film, which is supported by a metal frame. The particles are supposed to distribute uniformly with random orientations throughout the grid holes. In order to fix the particles, the grid is plunged into a cryogen. So that, the particles are flash-frozen and covered by thin vitreous ice. This layer does not only fix the particles, but also prevents them from the radiation damage to some extent. The alternative method for the cryo-EM is to apply negative staining. In this technique, the specimen is embedded into a heavy metal salt solution. This solution fills the space around the particles, but does not penetrate inside of them. Therefore, these specimens reveal the envelope of the particles with good contrast. Cryo-EM is more preferable than negative staining considering the artifacts arising from the interaction of the particles with the stain. However, in the case of particles, which cannot be purified to homogeneity, high contrast images are required to be able to discriminate the particles from the other contaminants. Therefore, in these cases negative staining may still be more preferable until the instrumentation technology is developed enough to produce high contrast images without staining.

1.2.2. Data Acquisition

In the early applications of cryo-EM, the images of the particles were acquired by a photographic film. Then, the film was scanned and digitized by high-quality scanners. Although this

method provided relatively high resolution, it was tedious to use in practice. It is also possible and more practical to acquire the images with the charge coupled device (CCD) cameras although the resolution is not as high as using the film. Recently, the direct-detection cameras have been introduced to the field and they improved the image quality. These cameras detect the electrons directly without converting them into photons, as it is the case in CCD cameras. This way, the detection sensitivity is improved significantly. Another advantage of direct detectors is that they enable data acquisition in the movie mode due their short response time. This feature is utilized by the researchers to correct the image blurring arising from the tiny movements during the imaging. With these new improvements in the data acquisition technology, it has been possible to obtain reconstructions at near-atomic resolution.

1.2.3. Contrast Transfer Function Correction

Contrast transfer function (CTF) describes the how the image contrast is transferred by the electron microscope with respect to the spatial frequency. Its shape depends on imaging parameters such as the spherical aberration coefficient of the objective lens, electron acceleration voltage, and defocus value. A typical CTF curve is presented in Figure 1-4. The first zero crossing of the curve is important in terms of the resolution of the generated image. There are specialized image processing algorithms to estimate the CTF and compensate for its effects (phase flipping [18], Wiener filtering [19], etc). Even in this case there exists a limit of recoverable information, which is the point where the curve saturates to zero as it is shown in Figure 1-4.

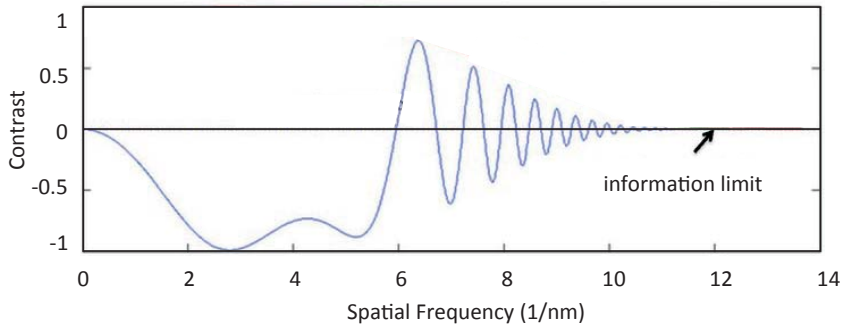

Figure 1-4. A typical CTF curve is presented with respect to spatial frequency.

1.2.4. Class averaging

Several individual particle images can be combined, in order to obtain the image of a particle from a certain point of view with an improved SNR. The images of the structurally identical particles with the same orientation can be averaged to improve SNR. First, the particle images are detected through the micrograph images and isolated individually. Then these isolated individual micrograph images are classified according to their orientation so that each class consists of the particle images from the same point of view. The particles inside each class are aligned with each other by

calculating the cross correlation in between, conventionally. In order to classify the particles with respect to their orientation, it is required to use some advanced statistical methods, such as multi-variate statistical analysis and hierarchical ascendant classification [20], K-means clustering [21], and likelihood optimization [22].

It is also a common practice to low pass filter the images to reduce the effect of noise on the alignment and classification steps. The CTF estimation and correction can also be applied together at this step. Once the images are classified, aligned and CTF corrected, they can be merged by using Wiener filter (WF) [23]. It is the optimal filter in the least-squares sense to merge these images assuming that they are stationary. It is easier to satisfy this assumption locally rather than globally [19][24]. Therefore, the local adaptive application of the Wiener filter (laWF), we developed for class averaging, provided successful solutions in merging the individual particle images [P5]. laWF utilizes a sliding window and calculates the Wiener filter coefficients patch by patch instead of using the whole image. The raw projection images for an experimental dataset of 50S ribosomal subunit and the class averages calculated with WF and laWF are illustrated visually in Figure 1-5.

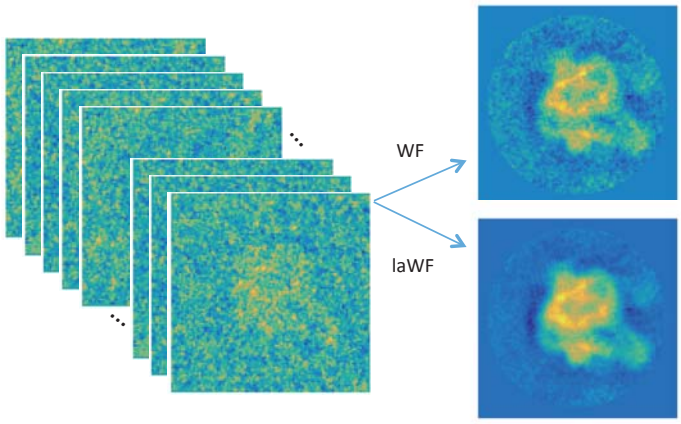

Figure 1-5 Class averaging with WF and laWF methods using an experimental dataset of 50S ribosomal subunit

There are two major methods to assign the projection angles to the images. One is the common lines method [25] and the other one is the iterative projection-matching algorithm [26]. Common lines method is based on the Fourier slice theorem. Fourier transform of the 2D projection images intersect each other through a line in the transform domain. This common line is detected and utilized to find the relative orientation in between the particles. The iterative projection-matching algorithm uses the simulated projections from a low-resolution 3D initial model. These projections are compared with the measured projections for the angle assignment. The assignment of the angles can be refined iteratively until convergence.

1.2.5. Tomographic Image Reconstruction

In the common practice of the particle classification, small number of classes (around 100 classes) with the highest quality class-average images is selected. This sparse sampling of the projection angles reduces the resolution of the 3D reconstruction. Since the particles are randomly oriented, the distribution of the projection angles and SNR level of the projection images can be uneven. Some particles may have 'preferred orientations'. For these reasons, there may be blocks of missing information in the Fourier domain yielding artifacts in the reconstructed image.

In order to compensate for the missing projection angles, the specimen can be tilted to acquire additional projections. These projections with the known tilt angle are utilized to improve the angle classification accuracy and the resolution of the reconstruction result. Random conical tilt reconstruction is a widely used application of this approach to obtain images of the protein molecules [27]. Despite the extra tilt, there still exists missing information in the Fourier space. This missing region is called "missing cone". The missing cone produces artifacts in the reconstruction result. The sparse sampling of the projection angles and the missing cone are visualized in Figure 1-6. It is important to compensate for the sparse sampling gaps or the missing cone to improve the resolution and accuracy of the 3D reconstruction.

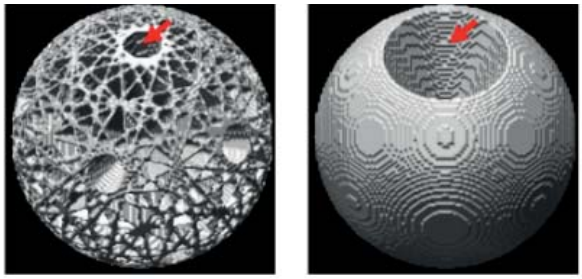

Figure 1-6. The distribution of the projection angles for sparse sampling (left) and random conical tilt (right) case. The locations of the projection angles are painted by gray on the surface of a sphere. The red arrows indicate the locations of the missing information blocks [P2].

Several software packages implementing different versions of back-projection and algebraic 3D reconstruction methods are available publically in the field of SPR [18], [28]–[32]. Although these methods provide simple and efficient ways of 3D reconstruction, they can produce some artifacts due to this information gap [33]. It is known that back-projection methods are sensitive to the missing information in tomographic reconstruction. It is also reported that algebraic methods do not fill the missing information blocks in the frequency domain [34]. On the other hand, the statistical reconstruction methods we developed can provide a compensation for the missing information [P2, P4].

1.3. Objectives and the Outline of the Thesis

The main objective of this thesis is to improve the accuracy and resolution of the 3D tomographic images of the biological samples reconstructed with electron microscopy in both ET and SPR. The major challenges we focus on are the incompleteness, nonuniform distribution and the low SNR of the projection data. In order to achieve our goal, we discover and extend the potential of statistical reconstruction methods following the steps below:

- developing the methods to compensate for different range and distribution of missing projection images
- analyzing and improving the robustness of the methods against different noise levels and acquisition geometries
- extending the methods to support projection angles distributed freely in the 3D space
- decreasing the computation time of the methods
- improving the usability of the methods by minimizing the number of parameters to be set by the user
- designing filters to improve the accuracy of the average projection images in SPR for the 3D reconstruction

The thesis is organized as follows: First, the tomographic reconstruction methods will be covered focusing on the ones widely used in the field of electron microscopy. Next, the statistical reconstruction methods will be presented covering the methods developed by the author. Then, the methods used to evaluate the reconstruction results will be described. Finally, the results of the publications constructing basis for this thesis will be summarized and the thesis will be concluded.

Chapter 2

Tomographic Reconstruction

Tomographic reconstruction is the mathematical procedure of obtaining images of internal structures of objects in 3D through their 2D projections. The formation of these projection images with electron microscope can be modeled considering quantum and relativistic aspects of the illumination of the specimen, interaction of electrons with the specimen, microscopy optics, and the detector physics. However, this would be cumbersome in terms of computational aspects. Therefore, it is required to make some assumptions on the image formation process to have a computationally feasible mode. Here, we consider bright field imaging mode and parallel beam of electrons. Moreover, we assume that the electrons do not interact with each other and we ignore multiple scattering of the electrons based on the thin shape of the specimen. Considering these assumptions, the image formation can be expressed as:

$$p^{\mathrm{raw}} = C - \{\mathrm{PSF} * p\} \tag{2-1}$$

where the raw projection image is represented by p^{raw}, C is the data that would be measured in case there was no specimen, PSF is the overall point spread function of the imaging system, $*$ is the convolution operation. C and PSF can be measured or estimated separately to obtain p in equation (2-1). We will refer p as the projection image which represents the number of electrons scattered while passing through the specimen. The intensity of the projection image is proportional to the cumulative electrostatic potential of the target on the pathway from the electron gun to the detector. This relation can be expressed by the ray transform of the target $v(x, y, z)$ as follows:

$$p(\boldsymbol{s}_{\boldsymbol{\tau}}) = \int v(x, y, z)\, d\tau \qquad \boldsymbol{\tau} \perp \boldsymbol{s} \tag{2-2}$$

where $\boldsymbol{\tau}$ is the projection direction which is perpendicular to the projection image plane $\boldsymbol{s}$.

Various methods have been proposed for the reconstruction of v from a set of projection images. This chapter reviews these methods by focusing on the ones commonly used in the field of electron microscopy. The reconstruction methods can be categorized into three groups as: algebraic methods, transform domain methods, and statistical methods. The algebraic and transform domain methods will be presented in the following two subsections. The statistical methods will be explained in the next chapter by covering the methods developed by the author.

2.1. Algebraic Reconstruction Methods

The relation between an arbitrary 2D object, $v(x,y)$, and its 1D parallel beam projections is expressed by the ray transform as follows:

$$p(s,\theta) = \int\limits_{(s,\theta)\,\text{line}} v(x,y)dl \tag{2-3}$$

where $v(x,y)$ represents the target and $p(s,\theta)$ is the projection of the target in the s-axis for the projection angle θ. For the single tilt axis case, the relation between the (x,y) slice and the s-axis can be expressed as:

$$s = x\cos\theta + y\sin\theta\ . \tag{2-4}$$

This relation is illustrated geometrically in Figure 2-1. Using equation (2-4) with the line integral in equation (2-3), the projection operation can be written as:

$$p(s,\theta) = \iint\limits_{-\infty}^{+\infty} v(x,y)\delta(x\cos\theta + y\sin\theta - s)dxdy \tag{2-5}$$

where $\delta(\cdot)$ is the Dirac delta function. The expression in equation (2-5) is called the Radon transform and it is referred to as the forward problem in tomographic imaging. The reconstruction of the object from its projections is regarded as the inverse problem. Theoretically, the Radon transform is invertible in its continuous form if infinite number of projections is available. However, only a finite number of projections can be measured in discrete form practically. This can be expressed as:

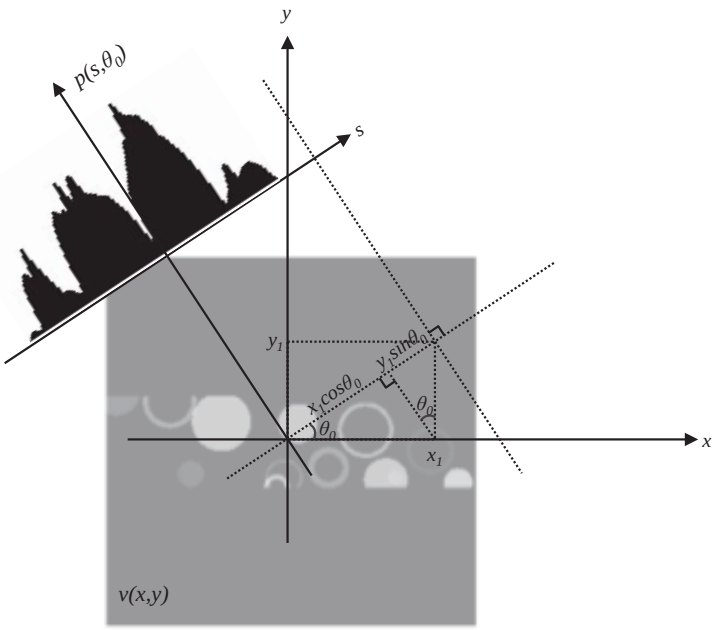

Figure 2-1. Projection data generation geometry via Radon transform

$$p_d = \sum_b a_{db} v_b \tag{2-6}$$

where v_b is the b^{th} voxel of the discretized target volume, p_d is the d^{th} projection data, a_{db} is the contribution of the b^{th} voxel to the d^{th} projection data. The set of all measurements discretized as in equation (2-6) can be expressed in matrix form as:

$$\mathbf{p} = \mathbf{A}\mathbf{v} \tag{2-7}$$

where $\mathbf{p}$ is the projection data constructed by concatenating the projection images in vector form, $\mathbf{v}$ is the vector form of the object to be reconstructed, and $\mathbf{A}$ is the projection matrix. The elements of the projection matrix $\mathbf{A}$ are the interpolation weights representing the contribution of each voxel to the projection data.

Finding $\mathbf{v}$ given $\mathbf{A}$ and $\mathbf{p}$ in equation (2-7) can be considered as a discrete inverse problem. An inverse problem is called well-posed if the solution exists uniquely for each $\mathbf{p}$ and the solution depends on $\mathbf{p}$ continuously (i.e. stability). Otherwise, the problem is called ill-posed. The projection matrix, $\mathbf{A}$, is usually rectangular. Therefore, the problem is either over-determined or under-determined which implies that either the solution does not exist or it is not unique. Moreover, the solution may not necessarily depend on $\mathbf{p}$ continuously. Therefore, small changes in $\mathbf{p}$ may change the solution drastically.

In order to obtain an approximate solution for the equation (2-7), algebraic reconstruction methods try to minimize the following cost function:

$$C(\mathbf{v}) = |\mathbf{Av} - \mathbf{p}|^2 . \tag{2-8}$$

For the overdetermined case where the number of projections exceeds the number of voxels, the cost function, $C(\mathbf{v})$, can be minimized in a least squared sense as:

$$\hat{\mathbf{v}} = \left(\mathbf{A^T A}\right)^{-1}\mathbf{A^T p} . \tag{2-9}$$

The size of the projection matrix, $\mathbf{A}$, is very large in general. Therefore, the calculation of its inverse is impractical. The iterative approaches are used to obtain a practical solution for the problem.

2.1.1. Simultaneous Iterative Reconstruction Technique (SIRT)

Simultaneous Iterative Reconstruction Technique (SIRT) is a practical approach to minimize the expression in equation (2-8). It uses the gradient descent method in the minimization problem as follows:

$$\mathbf{v}^{\mathrm{i}+1} = \mathbf{v}^{\mathrm{i}} - \alpha^{\mathrm{i}}\mathbf{A}^{\mathrm{T}}\left(\mathbf{Av}^{\mathbf{i}} - \mathbf{p}\right) = \mathbf{v}^{\mathrm{i}} - \alpha^{i}(\mathbf{A^T Av}^{\mathrm{i}} - \mathbf{A}^{\mathrm{T}}\mathbf{p}) \tag{2-10}$$

where $\mathbf{v}^{\mathbf{i}}$ is the voxel values at ith iteration. The iterations are usually initialized with zero. α^{i} is the relaxation parameter at ith iteration. It can be set to a constant value throughout the whole iterations [35]. An alternative way is to calculate it via steepest descent algorithm for faster convergence. In this case, the relaxation parameter is calculated as:

$$\alpha^{\mathrm{i}} = \arg\min_{\alpha>0} C\left(\mathbf{v}^{\mathrm{i}} - \alpha\nabla C\left(\mathbf{v}^{\mathrm{i}}\right)\right) . \tag{2-11}$$

The expression in equation (2-8) can be improved to regularize noise and consider the CTF of the microscope as:

$$C(\mathbf{v}) = (1-\mu)|\mathbf{SAv} - \mathbf{p}|^2 + \mu|\mathbf{Bv}|^2 \tag{2-12}$$

where $|\mathbf{Bv}|^2$ is the regularization term in which $\mathbf{B}$ represents the discrete Laplacian or higher order derivatives. $\mathbf{S}$ stands for the CTF of the microscope. It approximates the point spread function, which is the inverse Fourier transform of the CTF, in a space invariant way. μ is the Lagrange

multiplier adjusting the weight of the regularization term. This expression given in equation (2-12) can be minimized iteratively as:

$$\mathbf{v^{i+1}} = \mathbf{v^{i}} - \alpha^{\mathrm{i}}\left\{(1-\mu)\left((\mathbf{SP})^{\mathrm{T}}(\mathbf{SP})\mathbf{v}^{\mathrm{i}} - (\mathbf{SP})^{\mathrm{T}}\mathbf{p}\right) + \mu\mathbf{B}^{\mathrm{T}}\mathbf{B}\mathbf{v}^{\mathrm{i}}\right\}. \tag{2-13}$$

The implementation expressed in equations (2-12) and (2-13) is available in the SPIDER software package [36]. However, it has several different implementations available [37]–[39].

2.1.2. Algebraic Reconstruction Technique (ART)

Algebraic Reconstruction Technique (ART) is a similar reconstruction method in terms of the formulation. However, it is different from SIRT in terms of the data block used to update the reconstructed volume throughout the iterations. SIRT updates the reconstructed volume simultaneously using all the projection data available. In ART, the updates are realized by using equations for each element of the projection vector, $\mathbf{p}$, one by one. This improves the convergence speed of the algorithm. An implementation of ART is available in the Xmipp software package [31].

The algebraic reconstruction methods are applicable to various data acquisition geometries. However, they do not fill the missing information in the Fourier domain with a meaningful information. This yields artifacts in the reconstructed volume.

2.2. Transform Domain Reconstruction Methods

The transform domain reconstruction methods are based on the Fourier slice theorem. The theorem indicates that the Fourier transform of a projection for an angle θ equals to the central section of the Fourier transform of the original object at angle θ [40]. This theorem, also known as central slice theorem, is illustrated in Figure 2-2 for 2D case. It can be expressed mathematically as:

$$P(w,\theta_0) = V(w\cos\theta_0, w\sin\theta_0) \tag{2-14}$$

where w represents the spatial frequency, $P(w,\theta_0)$ is the 1D Fourier transform of the projection data for projection angle θ_0, and V is the 2D Fourier transform of the image to be reconstructed. Transform domain reconstruction methods can be grouped into two as: filtered back projection (FBP) and direct Fourier inversion (DF) methods.

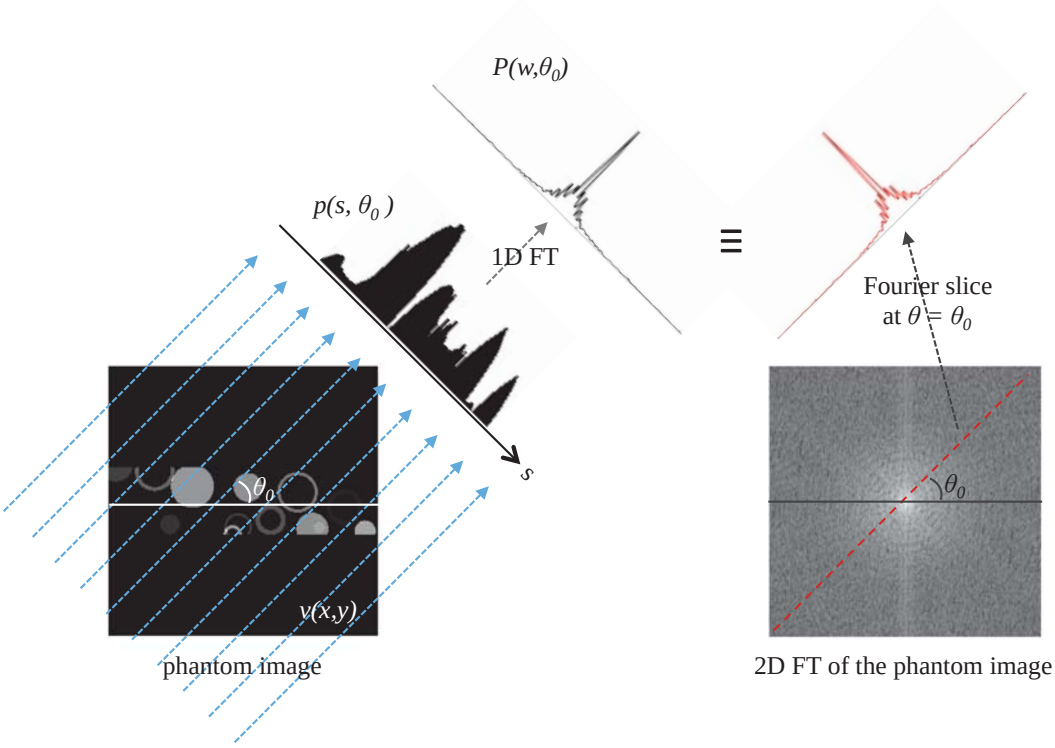

Figure 2-2. Fourier slice theorem is illustrated for a 2D slice image

2.2.1. Filtered Back Projection (FBP)

FBP methods construct filters to account for the particular distribution of projection data. The algorithm can be expressed for 3D case as:

i) Calculate the 2D Fourier transform of the projection images.
ii) Multiply Fourier transform of each projection with the weighting filter (i.e, Colsher filter [41]).
iii) Take 2D inverse Fourier transform of the filtered projections.
iv) Apply backprojection to the filtered projections in real space to reconstruct the volume.

For the single tilt axis geometry with equiangular space between the projection angles, the FBP algorithm can be expressed for a 2D slice as follows:

$$v(x,y) = \int_0^{\pi} F^{-1}[\,|R|\,F[p(s,\theta)]\,]\;d\theta \tag{2-15}$$

where $|R|$ is the ramp filter and F represents the Fourier transform. It can be used together with a smoothing filter (e.g. Hamming, Hanning filters) in order not to exaggerate the noise located at high

frequencies. The FBP methods are quite fast, easy to implement and use. It is hard to calculate the optimum filter weights especially for the uneven distribution of the projection angles in the 3D case. However, a filter referred as exact filter is available in the field for the 3D case [42]. Various implementations of the FBP methods are also available with a general name of weighted back projection (WBP) in the commonly used electron microscopy software packages [37].

2.2.2. Direct Fourier Inversion (DF)

Direct Fourier inversion methods aim to fill the Fourier space based on the projections directly. Once the 3D Fourier domain is filled by using Fourier slice theorem, the object can be reconstructed by taking the 3D inverse Fourier transform. If accurate measurements of the projection data are available for infinitely many projection angles, the object can be reconstructed perfectly. This is hard to apply in practice due to the following reasons:

i) The number of projections is limited. The Fourier space is not sampled uniformly. The sampling is dense at the central regions corresponding to low frequencies and it is sparse at the borders corresponding to high frequencies.
ii) The measurements are imperfect. The noise contaminates the projections and the projection angles may not be accurate.
iii) It requires interpolation between the Cartesian and polar coordinate systems in the Fourier domain. This introduces some artifacts to the reconstruction due to interpolation errors.

However, with the increasing computation power, it is possible to use tens of thousands of projection images which enable the DF algorithm to yield more accurate results.

Chapter 3

Statistical Reconstruction Methods

The statistical reconstruction methods have provided successful results in emission tomography (i.e. positron emission tomography – PET, and single photon emission computed tomography - SPECT) by reconstructing 3D images from noisy projection data [43]–[45]. They have been available in the SPR software packages and they are getting increasing interest in 3D refinement and 3D classification [44]–[50].

The formation of the projection data was expressed in the previous chapter as:

$$p_d = \sum_b a_{db} v_b \tag{3-1}$$

where p_d is the d^{th} projection data, a_{db} represents the contribution of the b^{th} voxel to the d^{th} projection data, and v_b is the random number of electrons scattered inside the b^{th} voxel of the discretized target volume while traveling along the beam direction. The reconstruction methods to calculate v_b algebraically based on the equation (3-1) were covered in chapter 2. These methods cannot provide exact solutions since the measurements are noisy and a_{db} values are the approximate values. They try to fit the reprojection of v_b values to the noisy measurements, p_d in the least squares sense. The solution they provide for v_b can contain negative values. The statistical reconstruction methods we present in this chapter assume v_b to be drawn from a Poisson distribution with mean λ_b, which is nonnegative by definition. Since v_b values are just outcomes of the random event, they are inherently noisy. The interest of these statistical methods is not to find out how many electrons were scattered during a particular acquisition period but the

mean values of these entities. These mean values can be expressed as follows by taking the expected value of both sides in the equation (3-1):

$$\lambda_d = \sum_b a_{db}\lambda_b \tag{3-2}$$

where λ_d is the mean of the d^{th} projection data, p_d. Since we have p_d values instead of λ_d, we cannot solve equation (3-2) as equation (3-1). Therefore, we need to use the statistical link between the measurements, Data, and the image to be reconstructed, Img, via the Bayes' rule as:

$$P(\mathrm{Img}|\mathrm{Data}) = \frac{P(\mathrm{Data}|\mathrm{Img})P(\mathrm{Img})}{P(\mathrm{Data})} \tag{3-3}$$

where $P(\mathrm{Img}|\mathrm{Data})$is the a posteriori probability density function, $P(\mathrm{Data}|\mathrm{Img})$ is the likelihood of observing the measured projection data, given the image to be reconstructed. $P(\mathrm{Img})$ and $P(\mathrm{Data})$ represent the a priori probability distributions for the image and the measured data, respectively. $P(\mathrm{Data})$ can be excluded from the expression assuming that it is constant. The maximum a posteriori probability expectation maximization (MAPEM) method estimates the image parameters, $\boldsymbol{\lambda}$, which maximize the a posteriori probability $P(\mathrm{Img}|\mathrm{Data})$ [53]–[55]. With these modifications, the MAPEM method can be expressed as:

$$\begin{aligned} P(\mathrm{Img}|\mathrm{Data}) &\simeq \underbrace{P(\mathrm{Data}|\mathrm{Img})}_{L(\boldsymbol{\lambda})}\ \underbrace{P(\mathrm{Img})}_{P(\boldsymbol{\lambda})} \\ \boldsymbol{\lambda}_{\mathrm{MAPEM}} &= \underset{\boldsymbol{\lambda}}{\mathrm{argmax}}\{\quad L(\boldsymbol{\lambda}) \qquad P(\boldsymbol{\lambda}) \quad\}\,. \end{aligned} \tag{3-4}$$

$L(\boldsymbol{\lambda})$ and $P(\boldsymbol{\lambda})$ are the likelihood and the penalization functions of the image $\boldsymbol{\lambda}$, respectively. If a priori information is not used, the penalization function is assumed to be constant. Then, the method maximizing only the likelihood function, $L(\boldsymbol{\lambda})$, is referred as the maximum likelihood expectation maximization (MLEM) method [53], [54]. The likelihood expression can be written as follows assuming the Poisson distribution:

$$L(\boldsymbol{\lambda}) = \prod_{db} e^{-\lambda_b a_{db}} \frac{(\lambda_b a_{db})^{v_b a_{db}}}{(v_b a_{db})!}\ . \tag{3-5}$$

Taking the natural logarithm of the expression does not affect the solution since it is a monotonically increasing function. Then the equation can be rewritten as:

$$\ln\big(L(\boldsymbol{\lambda})\big) = \sum_d \sum_b [v_b a_{db} \ln(\lambda_b a_{db}) - \lambda_b a_{db} - \ln(v_b a_{db}!)] \ . \tag{3-6}$$

In order to maximize the likelihood, the derivative of the expression in equation (3-6) can be taken with respect to λ_b [58]. By equating the result to zero, the parameters maximizing the likelihood can be obtained as:

$$\hat{\lambda}_b = \frac{\sum_d v_b a_{db}}{\sum_d a_{db}} \ . \tag{3-7}$$

The equation (3-7) cannot be used directly since the term $v_b a_{db}$ is not available. However, its conditional expected value can be calculated and employed in an expectation maximization algorithm [57] iteratively. This expected value can be expressed as:

$$E\left[v_b a_{db} | p_d, \lambda_b^{\langle k \rangle} a_{db}\right] = p_d \frac{\lambda_b^{\langle k \rangle} a_{db}}{\sum_{b'} \lambda_{b'}^{\langle k \rangle} a_{db'}} \ . \tag{3-8}$$

Using equation (3-8) inside equation (3-7), the MLEM method for estimation of $\boldsymbol{\lambda}$ can be expressed as:

$$\lambda_b^{\langle k+1 \rangle} = \frac{\lambda_b^{\langle k \rangle}}{\sum_d a_{db}} \sum_d \frac{p_d a_{db}}{\sum_{b'} \lambda_{b'}^{\langle k \rangle} a_{db'}} = \lambda_b^{\langle k \rangle} C_b^{L\langle k \rangle} \tag{3-9}$$

where $C_b^{L\langle k \rangle}$is the likelihood term. MLEM method produces unbiased but noisy images [59]. This can result in checkerboard artifacts especially with high number of iterations [60]. In order to control noise during the iterations, a regularization term, $C_b^{P\langle k \rangle}$, is included in MAPEM reconstruction in addition to the likelihood term. This regularization term represents $P(\mathrm{Img})$ in equation (3-4). Then, the iterative update equation of the MAPEM can be expressed as:

$$\lambda_b^{\langle k+1 \rangle} = \lambda_b^{\langle k \rangle} C_b^{L\langle k \rangle} C_b^{P\langle k \rangle} \ . \tag{3-10}$$

It is common to assume that the pixel values of the reconstructed image are locally monotonic. Among different implementations of this prior information, Median Root Prior (MRP) [17] has been successful in penalizing noise while preserving the edges. With MRP, the regularization term is expressed as:

$$C_b^{P\langle k\rangle} = \left(1 + \beta\left(\frac{\lambda_b^{\langle k\rangle} - \mathrm{med}(\lambda_b^{\langle k\rangle})}{\mathrm{med}(\lambda_b^{\langle k\rangle})}\right)\right)^{-1} \tag{3-11}$$

where $\mathrm{med}()$ is the operator representing the median filtering and the strength of this filter is controlled by the regularization parameter β. It needs to be in the range [0,1] to keep the intensity values positive throughout the iterations. The strength of the regularization filter increases with the increasing β. The stronger filter reduces noise more. However, it reduces the resolution at the same time. The selection of the β is a compromise between the resolution and the noise level of the reconstructed image. Therefore, it requires to be adjusted according to the data and the application manually. We develop automated ways to adjust this parameter in this study to make the method easier to use.

3.1. Sequential MAPEM Reconstruction Method

The sequential maxi mum a posteriori probability expectation maximization (sMAPEM) is developed in this study for ET [P1] and the extended to SPR [P2] to compensate for the missing projections and imperfect measurements. The method uses a sequence of regularization parameters instead of using a single constant one throughout all the iterations. A predefined number of iterations are realized for each regularization parameter. The result of each regularization stage initializes the next one. The regularization parameters are selected to be in the decreasing order. So that, the noise is highly suppressed by the high values of regularization parameters and a coarse but robust estimate of the image is obtained at the first regularization stages. Then, the resolution and contrast of the image are enhanced by decreasing the regularization parameters in the following regularization stages.

Although the sMAPEM method provides better accuracy and noise suppression than the conventional methods (i.e. WBP, SIRT, DF), it has a long computation time. Moreover, the method requires some parameters, namely the regularization parameters and the number of iterations per each regularization stage, to be set properly for the quality of the reconstructed image. Adaptive regularization and multiresolution reconstruction methods were developed as a solution for these problems.

3.2. Adaptive Regularization

Adaptive MAPEM (aMAPEM) was developed by the author as a solution for the regularization parameter selection problem of sMAPEM [P3]. The method is based on the idea of adjusting the regularization parameter, β, pixel-wise considering the local noise contamination, instead of using a single constant one for the whole image throughout the iterations. aMAPEM uses higher β

values for the regions with high variance of intensities than the regions with low variance. Therefore, in these regions the prior information is used more strongly. Since we assume Poisson distribution for the image intensities, the parameter of this distribution also equals to the variance of the intensities reconstructed. In order to keep the regularization parameter, β, in the range [0,1], we normalized the intensity values and used as the local regularization parameter as:

$$\beta_b^{\langle k \rangle} = \frac{\lambda_b^{\langle k \rangle}}{\max\limits_b \lambda_b^{\langle k \rangle}} . \tag{3-12}$$

Then the overall regularization term can be expressed as:

$$C_b^{P\langle k \rangle} = \left(1 + \beta_b^{\langle k \rangle} \left(\frac{\lambda_b^{\langle k \rangle} - \mathrm{med}(\lambda_b^{\langle k \rangle})}{\mathrm{med}(\lambda_b^{\langle k \rangle})} \right) \right)^{-1} . \tag{3-13}$$

3.3. Multiresolution Reconstruction

One problem of the developed MAPEM methods was their long computation time. In order to improve the convergence speed of MLEM, multiresolution reconstruction grids [61] and multiresolution detector space [62] were used previously in positron emission tomography (PET) and scanning transmission electron microscopy (STEM) [63]. It was also utilized in discrete tomography that reconstructs images composed of a few different intensity levels [64]. The author incorporated this method with MAPEM reconstruction of biological targets with electron microscopy. The developed multiresolution MAPEM (mMAPEM) method was used in SPR [P4] and also in ET together with adaptive regularization (adaptive multiresolution MAPEM, amMAPEM) [P3]. The multiresolution approach enabled MAPEM to proceed with regularization weight varying from strong to weak likewise in sMAPEM. Instead of decreasing the regularization parameter, the image size is changed. This multiresolution implementation is computationally more efficient and more robust against noise due to the binning.

In addition to the regularization parameter, the window size of the regularization filter with respect to the image size affects the strength of the penalization. In multiresolution reconstruction we change the image size and apply binning to the projection data step by step while keeping the filter size fixed. We increase the image size with respect to the filter size and reduce the binning factor of the projection data sequentially. The result of each resolution stage initializes the next one. This way, coarse but robust estimates of the images are obtained at the initial steps by suppressing the noise by binning and median filter used for the regularization. The binning reduces noise by averaging the intensity values in a local neighborhood at the expense of spatial resolution. In the proceeding steps, the image grid size is increased to enhance the resolution. The iterations

of the resolution stages are terminated when the normalized mean squared difference (NMSD) between the consecutive images goes lower than a threshold value. The flow diagram of the method is shown in Figure 3-1.

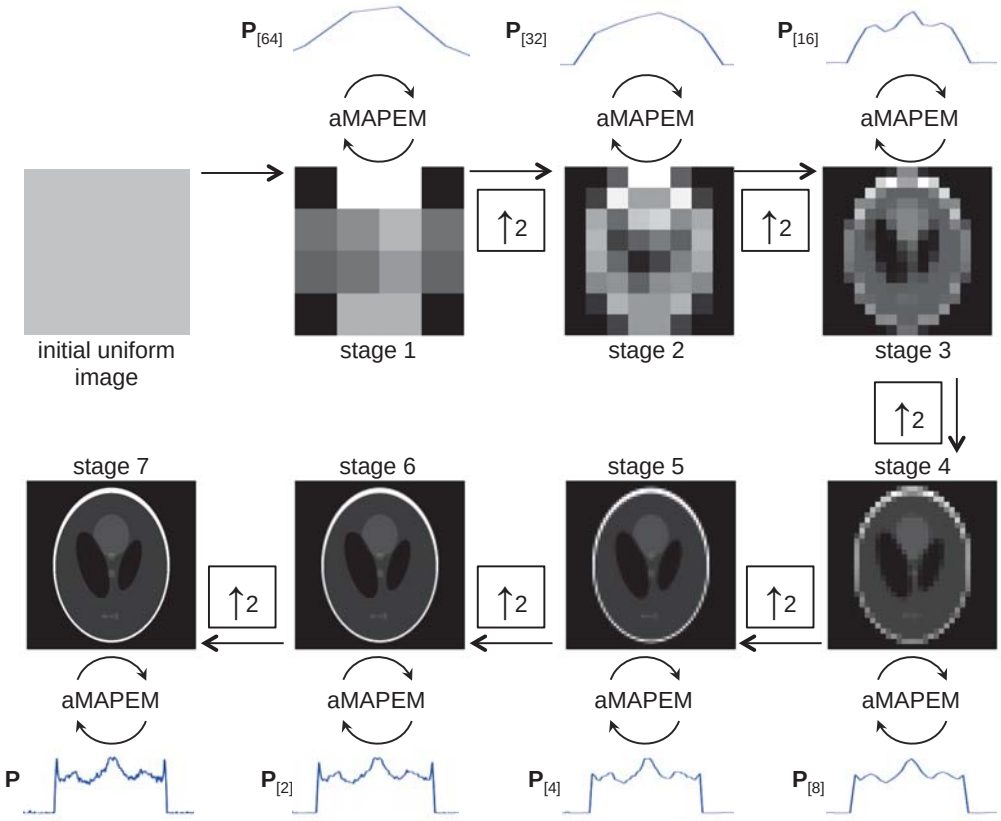

Figure 3-1. The flow diagram of the multiresolution reconstruction method. $\mathbf{P}_{[X]}$ is obtained by binning every X radial samples of the original projection data, **P**. The method is initialized with a uniform image of positive values. In the first stage, a 4x4 image is reconstructed using aMAPEM method with the projection data $\mathbf{P}_{[64]}$. In the following stages, the number of binned pixels is decreased to quarter and the radial projection samples are decreased to half. Each stage is initialized by the resulting image of the previous one after rescaling the image size and the intensity range. The final image is reconstructed at the last stage using the original projection data **P**.

Chapter 4

Evaluation of the Reconstruction Accuracy

The deviation of an image from the ideal case can be summarized assuming the imaging system is linear shift invariant as follows:

$$I^m = I * \mathrm{PSF} + n \tag{4-1}$$

where I^m is the measured image, I is the image one would obtain in the ideal imaging conditions, $*$ is the convolution operation, PSF is the point spread function representing the blurring effect of the whole image formation process, n is the additive noise component. PSF is analogous to the impulse response which describes the response of an imaging system to point source. The effect of PSF and noise on the measured image is visualized in Figure 4-1. The resolution of the image decreases with the increasing PSF width and noise level. In general, it is difficult to directly measure the PSF and noise effecting on the image formation process separately. However, their influence is measured indirectly by means of the evaluation methods.

The evaluation methods can be grouped into two as reference based and reference free methods considering the existence of a ground truth model in the calculations. The methods comparing the reconstruction result with an available ground truth model by means of some quantitative measures will be presented under the group of reference based evaluation methods. The methods evaluating the reconstruction results without using a ground truth will be presented under the reference free methods section.

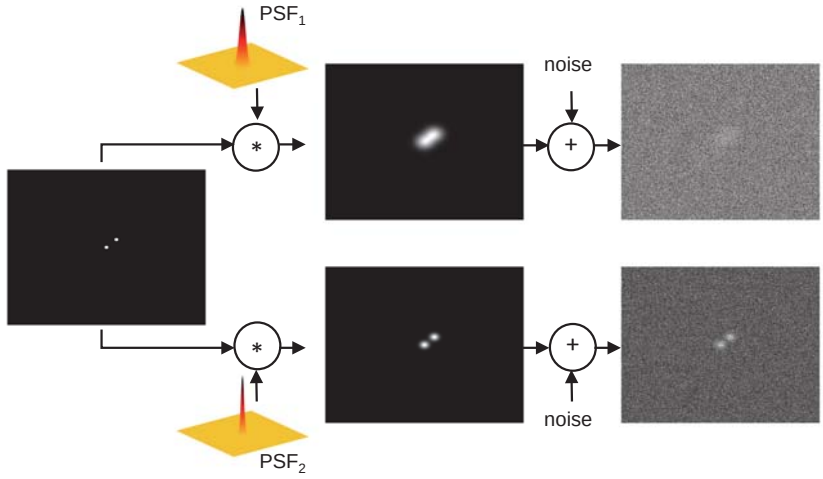

Figure 4-1. The effect of point spread function (PSF) and noise on image formation. With a narrow PSF and low noise contamination, it is still possible to resolve the two dots on the bottom row. However, they are indistinguishable on the upper row because of the wider PSF and higher Gaussian noise contamination.

4.1. Reference Based Evaluation

The reference based evaluation methods are used in the simulation experiments by using the numerical phantom as the ground truth. The reliability of the evaluations depends on how realistically the image formation process and the biological tissue are simulated. In Figure 4-2 A-D, the numerical phantoms designed to mimic the biological structures are presented. It is also possible to design a phantom to analyze a particular aspect of the reconstruction methods. For example, the phantom in Figure 4-2 E-F is used to analyze the missing wedge effects in frequency domain. The continuity of the circular lines in the reconstruction results gives information about the sensitivity to the missing wedge.

It is also possible to use reference based evaluation methods with experimental datasets if some information is available about the sample partially or entirely. Gold particles are one of the structures that have known dimensions in the specimen. Their known dimensions can be used as a reference for the evaluation of the reconstruction accuracy in electron microscopy. The particles are spread over the specimen before imaging in order to have some reference points for the accurate alignment of the projection images (see Figure 4-3). They ideally have a spherical shape with known radius. The deformations in their image give an idea about the resolution and homogeneity of the resolution throughout the image plane. The boundary between the biological tissue and the gold particle can be used for edge analysis. The intensity ratio between the gold particle region and the biological tissue can be used to assess the image contrast.

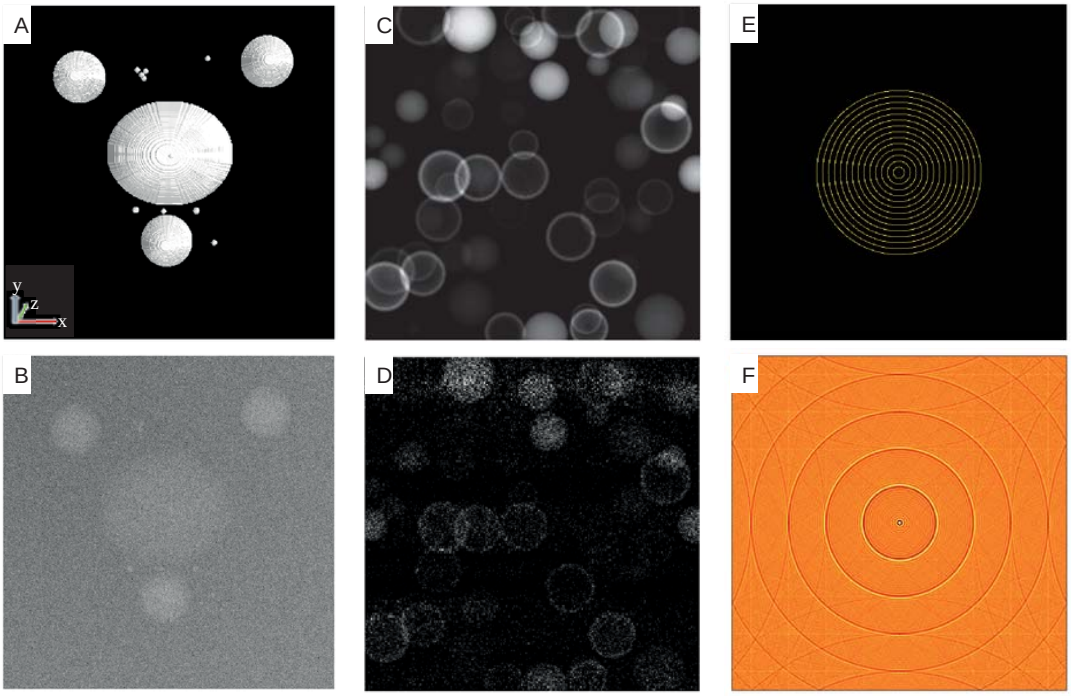

Figure 4-2. Numerical phantoms generated for the evaluation of tomographic reconstruction methods. A: The phantom mimicking cell vesicles, virus, and gold particles. B: The simulated zero-tilt projection image of the phantom in A. C: The phantom composed of spherical and hollow objects with different size and densities. D: The simulated zero-tilt projection image of the phantom in C. E: The frequency domain image of the phantom designed for missing wedge analysis. The continuity of the circular lines is observed for the missing wedge effects. F: The spatial domain view of the phantom in E.

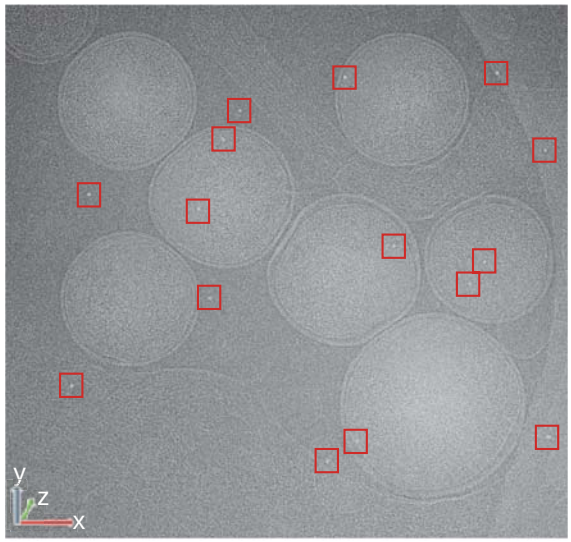

Figure 4-3. The gold particles on the zero tilt projection image of an experimental dataset [65][66]. The particles are shown by red squares.

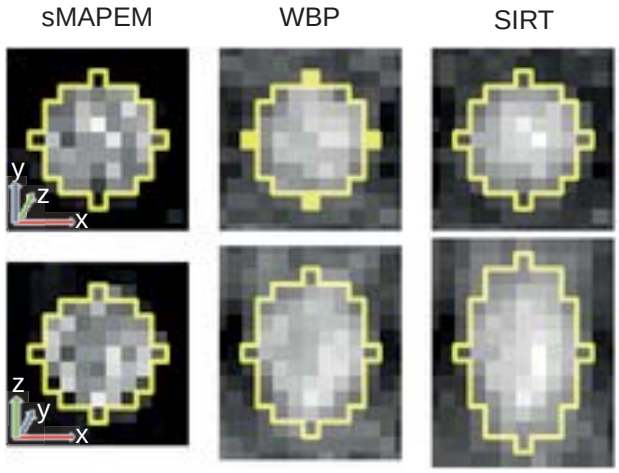

Figure 4-4. Sample images from the ellipsoid fitting method on a numerical phantom dataset [P1]. The upper row shows the central x-y slice images; the lower row shows the central x-z slice images. The columns show the images for sMAPEM, WBP and SIRT from left to right. The yellow contours show the borders of the ellipsoids fitted. The gold particle looks elongated in the z direction for the WBP and SIRT images due to the missing wedge. However, it preserves its circular shape in sMAPEM images because of the gap filling capability of the method.

In publication P1, we developed an ellipsoid fitting method in order to determine the boundary between the biological tissue and the gold particle in an objective way. We found the parameters of the ellipsoid maximizing the normalized cross correlation between the gold particle and the fitted ellipsoid. Some of the fitted ellipsoids are presented in Figure 4-4. We compared the radius of the fitted ellipsoid with the known radius of the gold particle to analyze the resolution of the images. The elongation of the particle image in x, y, and z dimensions provided us information about loss of resolution due the missing projection images and imperfections in the whole imaging process. We also used the boundaries of the ellipsoid to evaluate the contrast ratio of the images by calculating the ratio between the intensities of the gold particle region and the surrounding biological tissue.

4.1.1. Pixel Intensity Based Measures

The intensity values of the reconstruction results and the ground truth can be compared by means of mean squared error (MSE) and normalized cross correlation (NCC) as:

$$\mathrm{MSE} = \frac{1}{N^2}\sum_{i,j=1}^{N}(I_1(i,j) - I_2(i,j))^2 \tag{4-2}$$

$$\mathrm{NCC} = \frac{\sum_{i,j=1}^{N} I_1(i,j) I_2(i,j)}{\sum_{i,j=1}^{N} I_2(i,j)^2} \tag{4-3}$$

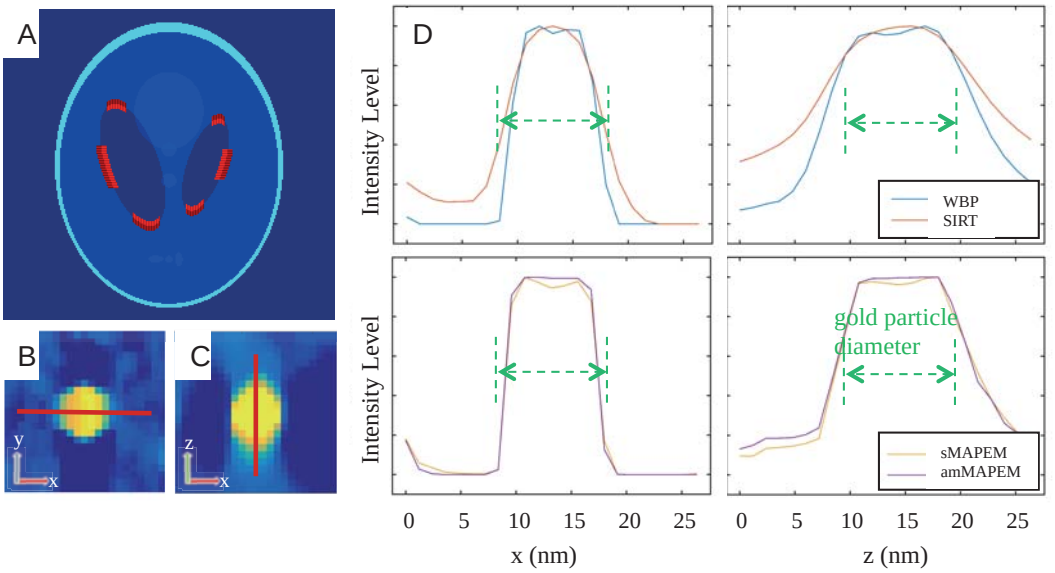

Figure 4-5. Edge analysis for the evaluation of image reconstruction methods. A: Red lines show the location of edges in x and y directions on Shepp-Logan phantom image. B-C: The red lines show the location of the line profile taken through the gold particles in the x and z directions consecutively. The images are taken from an experimental dataset of a cell vesicle [P3]. D: Line profiles taken from reconstruction result of different methods [P3]. The sharpness of the edges gives an idea about resolution of the images. The distortion in the z direction is more than the one in x direction because of the elongation due to the missing wedge.

where I_1 is the reconstruction result, I_2 is the ground truth, and N is the number of pixels. The calculations can be performed over the whole image or considering a particular region of interest.

The image can also be evaluated by comparing the contrast ratio (CR) between two different regions of interest. It can be calculated as:

$$\mathrm{CR} = \frac{\sum_{i,j\epsilon \mathrm{in}} I(i,j)}{\sum_{i,j\epsilon \mathrm{out}} I(i,j)} \tag{4-4}$$

where in and out are the inner and the outer regions of interest, respectively.

Since the summation of the intensity values is used in the calculation of contrast ratio, the effect of noise is reduced and the evaluation is focused on the effect of point spread function. However, MSE and NCC are more sensitive to the noise compared with the CR.

Figure 4-6. Calculation of full width at half maximum (FWHM). A. The profile taken through an edge on the image plane. B: The derivative of the edge in A representing the line spread function. FWHM is the width of the spread of the line at the half of its maximum intensity value.

4.1.2. Edge Analysis

The resolution characteristics of an imaging system can be analyzed using the edges laying throughout the image plane in different orientations. The sample edges that can be utilized for the analysis are shown on a phantom and experimental dataset in Figure 4-5. The sharpness of the edges gives an idea about the distortion introduced during the whole image reconstruction procedure with respect to the edge orientation.

The derivative of the line profile at the edge location may be used as a measure of edge spread function of the imaging procedure. The edge spread function can be summarized numerically by its full width at half maximum (FWHM) value. The calculation of FWHM is presented in Figure 4-6. In practice, a Gaussian curve is fitted to the edge spread function to get more reliable results.

4.2. Reference-Free Evaluation

There exist some reference free evaluation methods in the field of molecular electron microscopy to estimate the level of details that can be seen reliably. These methods evaluate the consistency of reconstruction results in the frequency domain as a one-dimensional function of spatial frequency.

Fourier Shell Correlation (FSC) is one of these measures commonly used in the field of molecular electron microscopy. The method splits the projection images into two halves. Two volumes are reconstructed using each half of the data independently. Then, the correlation between these two volumes is calculated in the frequency domain shell by shell. This way, the maximum spatial resolution that the volumes are consistent is revealed. The calculation of FSC can be expressed as:

$$\mathrm{FSC}(r) = \frac{\sum_{r_i \in r} F_1(r_i)\,.\,F_2(r_i)^*}{\sqrt{\sum_{r_i \in r} |F_1(r_i)|^2 .\ \sum_{r_i \in r} |F_2(r_i)|^2}} \tag{4-5}$$

where F_1 and F_2 are the Fourier transform of the volumes reconstructed using each half of the projection dataset. r_i is the i^{th} voxel at radius r. Typically, FSC curve decreases with the increasing spatial frequency. The resolution limit of the reconstruction is indicated by using various cut-off thresholds proposed (typically 0.5 or 0.143 [67]). The FSC measure is referred to as Fourier Ring Correlation (FRC) in 2D applications. In the subtomogram averaging based applications, 3D images of the identical particles are averaged to obtain the final reconstruction result with improved SNR. In this case, the accuracy of the result is evaluated by calculating FSC between two volumes obtained by averaging two independent subsets.

Chapter 5

Results

This chapter summarizes the results of the experiments conducted in publications P1-P5 with some of the datasets used in the publications. The default parameters recommended by the developers were used for the reference reconstruction methods unless stated otherwise. In publications P1 and P3, sMAPEM and amMAPEM were applied in ET and they were compared with the conventional reconstruction methods WBP and SIRT using the Dataset I and Dataset II, which are described in the Table 5-1. Figure 5-1 demonstrates some of the results. The visual comparison presented in Figure 5-1 shows that the missing wedge results in severe artifacts in WBP and SIRT reconstruction results. However, these artifacts are suppressed well in sMAPEM and amMAPEM reconstructions. The images also show that amMAPEM can suppress noise better than the sMAPEM method.

The numerical analysis of the results is presented in Figure 5-2. They are in line with the visual analysis. For the Dataset I, the line profiles are taken from a circular object and the FSC was calculated using the reconstructed volume completely. For the Dataset II, the line profile is taken from an isolated gold particle and the FSC is calculation was carried out using 5 randomly selected gold particles. The FSC curve presented is the average of these 5 FSC curves. The amMAPEM method provides more accurate results than the other reference methods. The reader may refer to [P3] for further results and experiments with different datasets.

We also compared the computation times of the methods for a single slice of the reconstructed volumes [P3]. The methods were implemented in MATLAB. The computations were carried on an Intel(R) Core(TM) i5 @ 3.20 GHz desktop computer with Windows 64 bit operating system. The computation times are given in the Table 5-2. Since the number of projection images is higher and the image sizes are bigger in Dataset II, it has a longer computation time. The number of iterations of the amMAPEM method is determined adaptively. The method requires more number of

iterations for the higher noise levels. Therefore, its computation time increases with the increasing noise level. Since the other methods use fixed parameter settings, their computation times are same for all noise levels. amMAPEM produces results in significantly shorter time than the sMAPEM method.

Table 5-1. The description of the datasets used in the experiments.

Dataset:	Projection Data:	Definition:
Dataset I [P3]	121 projection images with size 256x256 pixels. The images were simulated with 1° angular step in the range ±60°	The phantom dataset comprised of spherical objects. The projection images were contaminated by a mixture of Poisson and Gaussian noise to yield a final SNR level of 10.
Dataset II [P3]	131 projection images with size 1024x1024 pixels. Acquired with 1° angular step in the range ±65°	The experimental dataset of a freeze-substituted VeroE6 cultured cell infected with the SARS-CoV (The Cell Centered Database [68], [69]).
Dataset III [P2]	The conical tilt sampling case: 180 projections in a 60° conical tilt range with 2° angular steps were simulated.	The phantom dataset of 50s ribosomal subunit provided by the Protein Data Bank (PDB code: 1JJ2). The size of the model was 112 x 112 x 112 with isotropic voxel size of 3.26 Å/voxel. The projection images were contaminated by a mixture of Gaussian and Poisson noise. The resulting noise levels were set to different SNR values as 10.0, 5.0, 1.0, and 0.5.
Dataset IV [P2]	The sparse uniform sampling case: 91 projections with 15° angular steps were simulated.	
Dataset V [P4]	64 asymmetric Euler angles were used to simulate projections from the 3D model of the particle. The images were 182x182 pixels.	The phantom dataset of Hepatitis E Virus Like Particle (HEVLP, T=3). The size of the model was 182 x 182 x 182 with isotropic voxel size of 3.01 Å/voxel. The simulated projection images were contaminated by mixture of Gaussian and Poisson noise to yield an SNR value of 0.5.
Dataset VI [P5]	200 particle images for a single class. Image size was 100 × 100 pixels with isotropic pixel size of 3.26 Å/pixel. The images were CTF-corrected with ACE2 [70] algorithm.	The experimental dataset was comprised of 10,000 images randomly selected among 82,575 images of the 50S ribosomal subunit [41]. The particle images were classified into 196 classes using reference-based cross-correlation method. The classes with large number of particle images (more than 200 projections) were used in the experiments.

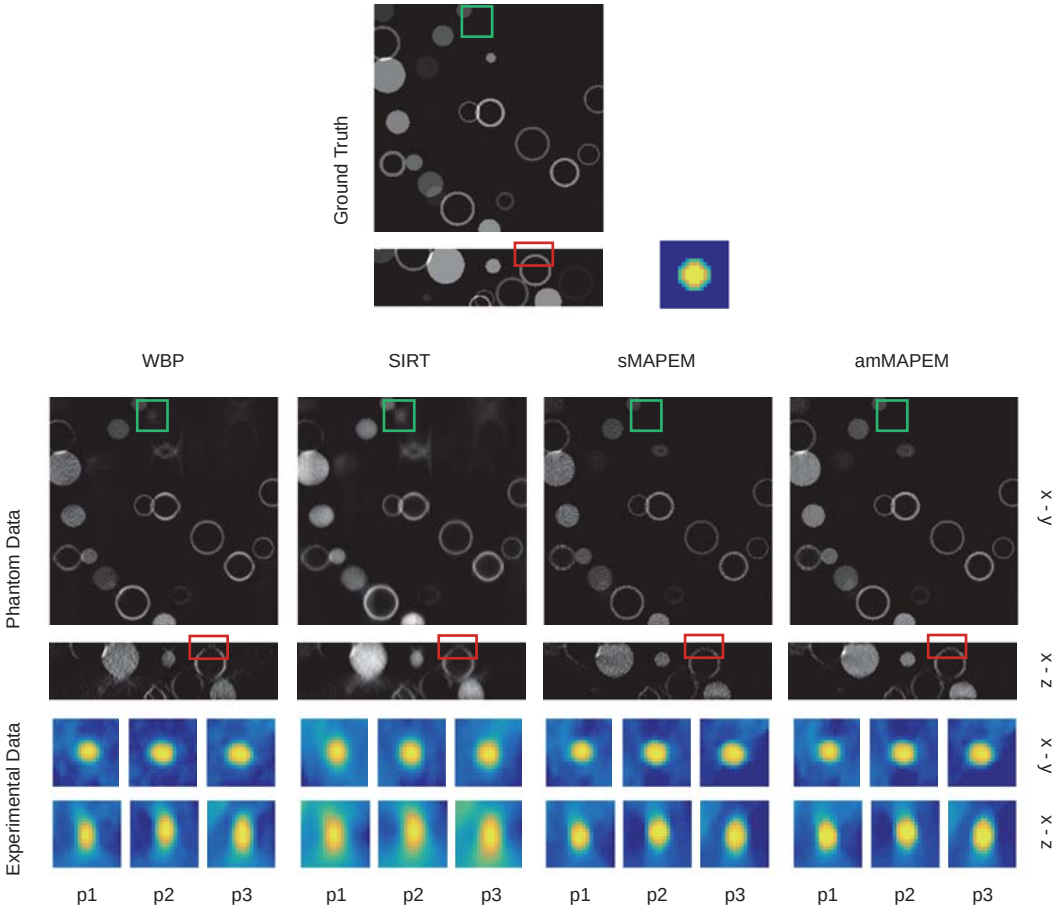

Figure 5-1. The x-y and x-z slice images from the reconstruction results. Top: The ground truth images are presented. Middle: The slice images for the Dataset I are presented. The tip of the objects elongated in the z-direction appears as an artifact in the x-y slices of the WBP and SIRT reconstructions (green rectangles). These artifacts do not exist for the x-y slices taken from sMAPEM and amMAPEM reconstructions. The deformation of the hollow spheres is shown by is shown by red rectangles. The circular shape is preserved in sMAPEM and amMAPEM reconstructions better than in the WBP and SIRT. sMAPEM images look noisier than the amMAPEM images. Bottom: The randomly selected three gold particle (p1-p2-p3) images cropped from the x-y and x-z slices of the Dataset II reconstructions are presented. sMAPEM and amMAPEM reconstructions have less elongation artifacts compared with the WBP and SIRT reconstructions.

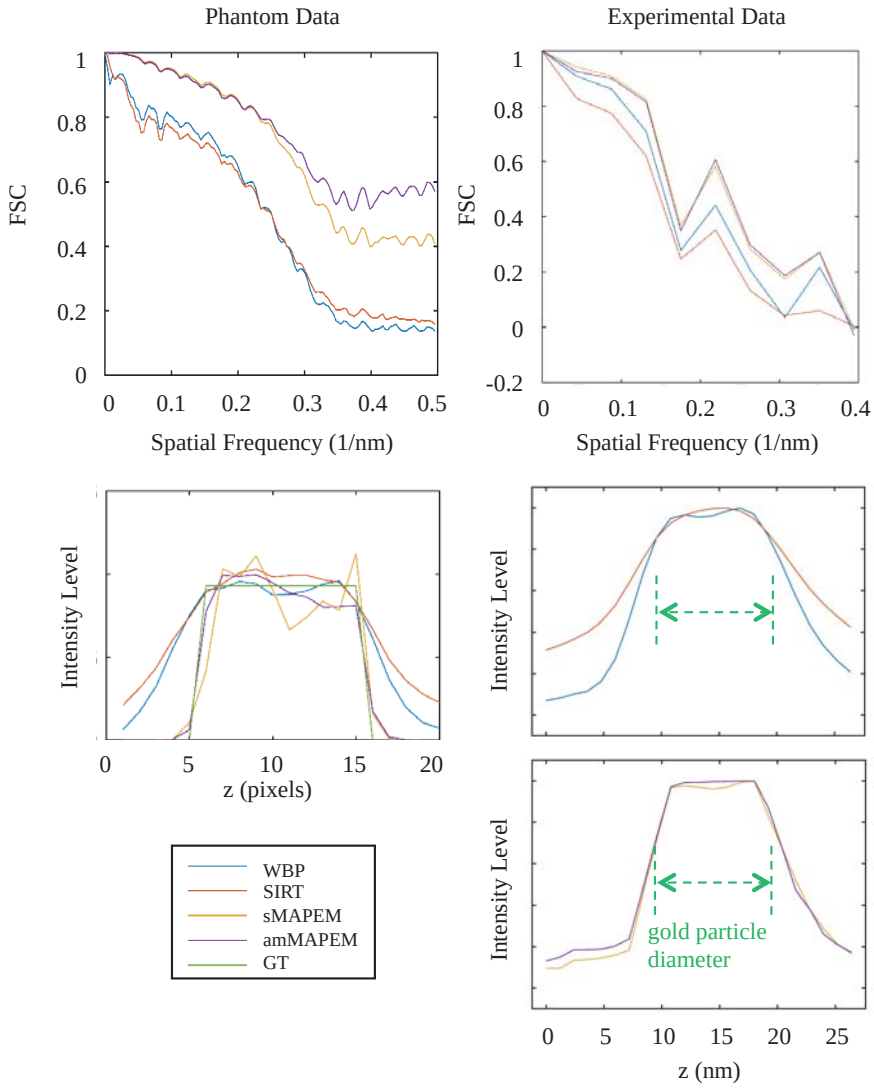

Figure 5-2. The FSC curves (top) and the line profiles (bottom) for the Dataset I and II. The profiles at the right middle and right bottom belong the same particle. The FSC values are clearly higher for sMAPEM and amMAPEM than for WBP and SIRT. The sMAPEM and amMAPEM profiles are closer to the ground truth than the WBP and SIRT profiles. The high intensity plateau is flatter for amMAPEM compared with sMAPEM due to the superiority of amMAPEM on noise suppression.

Table 5-2. The computation times for different reconstruction methods.

	Computation Time (sec.)	
	Dataset I slice	Dataset II slice
WBP	0.15	4.8
SIRT	11	321
sMAPEM	1360	17804
amMAPEM	245 (SNR 50) 289 (SNR 10) 612 (SNR 1)	3361

In publication P2, the proposed reconstruction methods were extended to support 3D Euler angles and adapted for 3D reconstruction in the field of SPR. sMAPEM method was compared with the Fourier domain reconstruction method implemented in XMIPP 3.1 (Direct Fourier - DF [31]) using Dataset III and Dataset IV described in Table 5-1. Figure 5-3 A and B present some of the results. The numerical analysis of the results is presented in Figure 5-4 A and B. sMAPEM is superior to DF in terms of compensating for noise and missing projection artifacts.

In publication P4, the multiresolution MAPEM (mMAPEM) method was developed for the reconstruction of symmetrical particles by improving the sMAPEM method in terms of computation time and accuracy. mMAPEM method was compared with the Fourier Reconstruction (FR) method implemented in EMAN2 [18], using phantom (Dataset V in Table 5-1) and experimental datasets. Icosahedral symmetry was imposed during the reconstruction in the image domain. Figure 5-3 C presents some of the results. The numerical analysis of the results is presented in Figure 5-4 C. mMAPEM produced more accurate and less noisy images compared to FR.

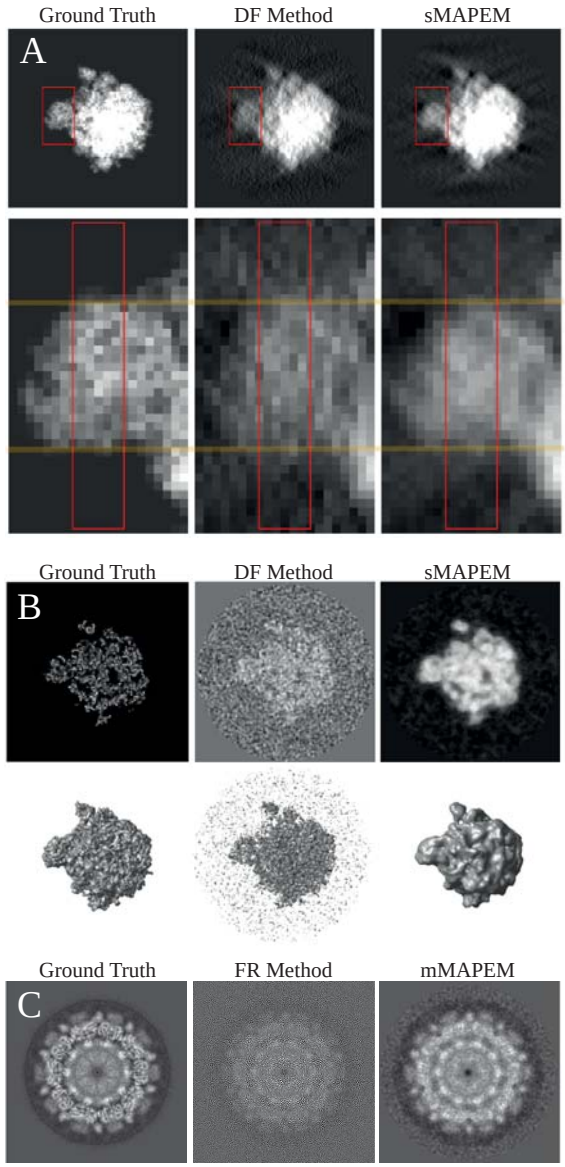

Figure 5-3. The visual analysis of the results in SPR. A: The projection images from the 50s ribosomal subunit phantom reconstructions for the random conical tilt case (Dataset III). A region of interest (red box on top) is shown in detail at the bottom. The sMAPEM images are closer to the ground truth image than the DF images. B: The reconstruction results of the 50s ribosomal subunit phantom reconstructions for the sparse angular sampling (15°) with SNR 1.00 (Dataset IV). The slice images are shown on top and the surface rendering images are shown on the bottom. The noise decreased the visibility of the details for the DF method while they are still visible to some extent in sMAPEM images. C: The slice images from the reconstruction result of the Dataset V. The mMAPEM image looks less noisy and shows more details than the FR image.

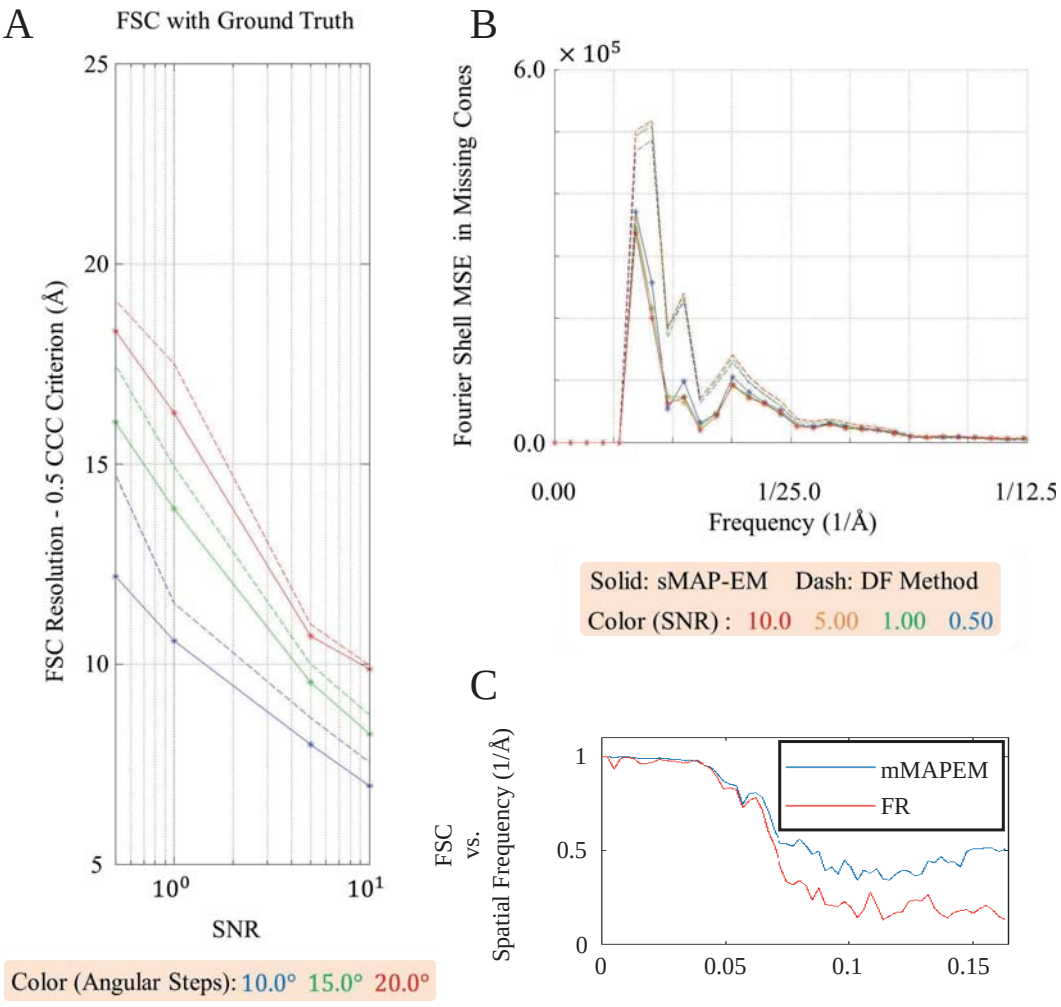

Figure 5-4. The numerical analysis of the results in SPR. A: FSC resolution analysis of sMAPEM and DF for equally distributed angular sampling. 0.5 cutoff frequencies of the FSC curves were used as the resolution criteria. The sMAPEM gives better resolution than the DF method for all SNR levels. B: Information filling in the missing cone. Fourier shell mean squared error (FSMSE, the MSE in the missing region of the frequency domain calculated over frequency bands) is calculated in the missing cone for DF and sMAPEM methods. FSMSE is lower for sMAPEM than for DF. C: The FSC analysis of the reconstruction results of the Dataset V. mMAPEM produces higher FSC values than the FR method.

In publication P5, the author proposed a local adaptive Wiener filtering method (laWF) in order to improve the class averaging accuracy of SPR. Figure 5-5 presents the comparison of the proposed laWF method with the conventional Wiener filter using the Dataset VI described in table 5-1. The images were divided into subsets composed of different number of images to be averaged. The figure shows that the laWF provides more accurate and less noisy images than the conventional WF.

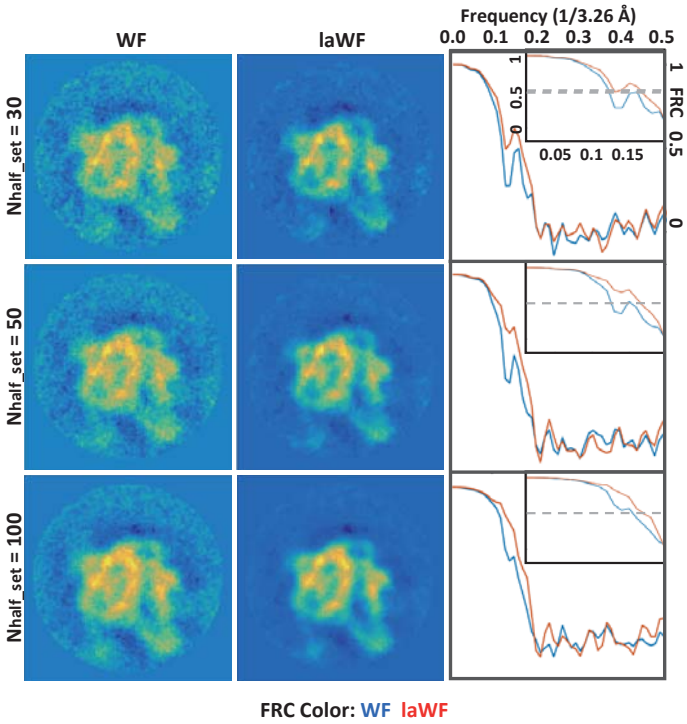

Figure 5-5. Analysis of merging different number of projection images with WF and laWF. Nhalf-set is the number of images merged in each of two independent subgroups. The FRC curves were calculated between these two independent groups. laWF outperforms WF.

Chapter 6

Summary of Publications

6.1. Publication 1

L. Paavolainen*, E. Acar*, U. Tuna, S. Peltonen, T. Moriya, P. Soonsawad, V. Marjomäki, R. H. Cheng, and U. Ruotsalainen, “Compensation of missing wedge effects with sequential statistical reconstruction in electron tomography”, PlosONE, 2014. (*: equal contribution)

Publication 1 introduced sMAPEM in ET to reconstruct biological samples in 3D by compensating the missing wedge artifacts. We compared the method with the conventional reconstruction methods WBP and SIRT by using synthetic datasets and an experimental dataset of a multivesicular body. We simulated a cell phantom dataset by considering different levels of noise and range of projection angles. For the analysis of the reconstructed images in terms contrast and resolution isotropy, we developed an ellipsoid fitting based evaluation method. The evaluation method utilized the gold particles randomly located inside the reconstructed volume for the numerical analysis. Although the method used the ground truth in the simulated cell phantom dataset, it was also possible to use it without ground truth in the experimental dataset case. In order to have a closer look at the projection gap filling capability of sMAPEM, we generated another synthetic dataset in frequency domain. In addition to numerical analyses, we used central slice and 3D surface rendering images for visual evaluation. With these numerical and the visual analysis of results, it was shown that the sMAPEM method suppresses the effects of the missing projections significantly. It produces better results than the conventional methods in terms of resolution isotropy, noise robustness and image contrast.

The author developed the sMAPEM method for ET together with U. Tuna and U. Ruotsalainen. He performed all the sMAPEM reconstructions in the publication. He equally contributed to the design of the experiments, analysis of the results and writing the manuscript with

L. Paavolainen. The preliminary version of the manuscript was published in L. Paavolainen's doctoral thesis [71]. Here, we present the version improved and extended with more datasets reconstructed to reveal different capabilities of the methods.

6.2. Publication 2

T. Moriya, E. Acar, R. H. Cheng, and U. Ruotsalainen, "A Bayesian approach for suppression of limited angular sampling artifacts in single particle 3D reconstruction", Journal of Structural Biology, 2015.

In Publication 2, we extended sMAPEM to support projection angles arbitrarily oriented in 3D space so that, we could utilize the method to provide a solution for the problems arising from the limited sampling of the projection angles in the field of SPR. In order to analyze the problem in detail, we simulated cryo-EM datasets of even and conical projection angle distributions for different angular sampling sparsity and projection image noise levels. Using these simulated datasets and an experimental dataset of cryo-EM, we compared our method with the direct Fourier method in terms of reconstruction accuracy and resolution. We established a criterion to select the final regularization weight of the sMAPEM using the simulated dataset of evenly distributed projection angles. We developed a quantitative analysis method to assess the information filled in the missing cone of the conical tilt sampling simulations in the frequency domain. This analysis has shown that the sMAPEM method can fill the unmeasured angular space with meaningful information. The results of quantitative and qualitative evaluations demonstrated that the sMAPEM method provides better reconstruction results than the direct Fourier method for all noise levels and projection angle sampling strategies.

The author contributed in extending the sMAPEM implementation into the field of SPR. He took part in designing the study and analysis of the results. He also contributed to the preparation of the manuscript by writing and preparing figures.

6.3. Publication 3

E. Acar, S. Peltonen, and U. Ruotsalainen, "Adaptive multiresolution method for MAP reconstruction in electron tomography", Ultramicroscopy, 2016.

In Publication 3, amMAPEM method was developed to provide a solution for regularization parameter selection and long computation time problems of sMAPEM. The proposed adaptive regularization method adjusted the strength of penalization according to local noise contamination. The computation time was reduced significantly by employing multiresolution approach in the reconstruction. The method was compared with WBP, SIRT, and sMAPEM in terms of reconstruction accuracy and computational efficiency. In the comparisons, we utilized a simulated biological phantom and two experimental datasets of ET. The evaluation results demonstrated that the amMAPEM method reconstructs images more accurately than WBP, SIRT, and sMAPEM methods. It was shown that the amMAPEM method outperforms sMAPEM also considering its computation time since it can reconstruct the images significantly faster due to the multiresolution

scheme used during the computations. Moreover, amMAPEM was superior to sMAPEM in terms of its usability in the field of ET since it does not require the user to perform additional analysis of the sample and the imaging environment to set the regularization parameter.

The author is the founder of the amMAPEM method implemented the method. He, designed and conducted the experiments, evaluated the results. He prepared the manuscript in collaboration with S Peltonen and U. Ruotsalainen .

6.4. Publication 4

E. Acar, M. A. Baikoghli, M. Stark, S. Peltonen, U. Ruotsalainen, R. H. Cheng, “Multiresolution MAPEM Method for 3D Reconstruction of Symmetrical Particles in Electron Microscopy”, In: Eskola H., Väisänen O., Viik J., Hyttinen J. (eds) EMBEC & NBC 2017. IFMBE Proceedings, vol 65. Springer, Singapore.

Publication 4 introduces mMAPEM method into the field of SPR for the reconstruction of symmetrical particles. The method utilized the symmetry of the particle by replicating the input projection images in the spatial domain by calculating the symmetrical Euler angles considering the geometry of the structure. We simulated a cryo-EM dataset of HEV for different number of projection images and noise levels. We also reconstructed an experimental dataset of cryo-EM for subsets of class average images with different noise levels. We compared the reconstruction results with the results of FR method by means of visual and numerical evaluations. The results have shown that the mMAPEM can reconstruct images more accurately than FR by providing robustness against noise and compensation for the limited angular sampling.

The author is the founder of the mMAPEM method. He implemented the method and conducted the reconstructions. He designed the study in collaboration with R. H. Cheng from the Molecular and Cellular Biology Department of the University of California, Davis. The phantom and the experimental data were provided by M. A. Baikoghli, M. Stark, and R. H. Cheng. He evaluated the results and prepared the manuscript in collaboration with the other coauthors.

6.5. Publication 5

A. Abdollahzadeh*, E. Acar*, S. Peltonen, and U. Ruotsalainen, “Local adaptive wiener filtering for class averaging in single particle reconstruction”, In: Sharma P., Bianchi F. (eds) Image Analysis. SCIA 2017. Lecture Notes in Computer Science, vol 10270. Springer, Cham. (*:equal contribution)

Publication 5 introduces local adaptive Wiener filter for the class averaging step of single particle reconstruction. Instead of using the whole image plane to estimate Wiener filter coefficients, the coefficients are calculated locally inside sliding windows throughout the image plane. The aim of this approach is to satisfy the stationarity condition for the Wiener filter better in local compared with the general case. The results are compared with the conventional Wiener filter using simulated and experimental datasets. The results of qualitative and quantitative comparison

show that the proposed method, LA-Wiener filter, is superior to the conventional one while calculating the class averages in the single particle reconstruction (SPR) applications.

This paper is extension of the masters thesis study supervised by the author [72]. The author provided guidance to define the research problem and to design the experiments. He also equally contributed to the preparation of the datasets, evaluation of the results. A. Abdollahzadeh prepared the manuscript in collaboration with the other coauthors.

Chapter 7

Discussion and Conclusion

The aim of this study was to develop a reconstruction algorithm that is capable of compensating for the incomplete and non-uniform distribution of projections freely distributed in 3D space, measurement imperfections, and noise. Furthermore, we aimed to minimize the number of parameters set by the user. Another goal was to reduce the computation time. In order to compensate for the imperfect and incomplete projection measurements, we utilized the power of statistical modeling and regularization based on prior information about the data. We developed sMAPEM for ET [P1] and then extended the method to support 3D projection geometry in SPR [P2]. Then, we improved the method in terms of accuracy, computation time and usability by employing adaptive and multiresolution reconstruction methods (amMAPEM) [P3]. We also used the 3D extended multiresolution reconstruction method in SPR (mMAPEM) for reconstruction of symmetrical particles [P4]. Furthermore, we developed the laWF for the class averaging step of the SPR to suppress noise effectively [P5]. The reader may refer [73] to access the code available for the developed methods.

There have been several attempts to recover the missing projection data in tomography. Interpolation [74], image inpainting [75], total variation and directional smoothing [76] methods have been be used previously for that purpose. The methods, which fill the missing region using the data available around the edges of the information gap, produce poor results for large missing wedge sizes and high noise levels. Recently, compressed sensing method was applied to ET to reduce artifacts arising from the missing wedge [77] [78]. The method assumes that the image is sparse in the gradient space. This assumption holds for ET of metals and nanoparticles; however, it is hard to assume that for the biological targets most of the time. We utilized statistical reconstruction methods to compensate for the incomplete and noisy projections in this study. The power of the methods arises from the priori information imposed during the iterations. The median filter realizing this prior regularizes the iterations and suppresses the artifacts arising from the

missing information and the noise. Another advantage of this filter is its capability of preserving the edges while filtering out the noise.

The strength of the regularization filter is adjusted by a scalar regularization parameter. In order to improve the visual quality of the reconstructed image, the value of the regularization parameter is required to be properly set considering the noise level, sample variation, image size, filter size, and validity of the prior information. There have been previous attempts to optimize regularization parameter based on the SNR analysis of the data [79]–[81]. These methods analyze the reconstruction results with different regularization parameters to find the optimum one. This requires multiple reconstructions and increases the computational cost of the overall reconstruction process. In sMAPEM we used sequence of parameters covering a wide range to obtain a solution as general as possible [P1]. This was also computationally expensive. The adaptive regularization method we developed in this study requires neither multiple reconstructions and extra analysis, nor a priori information about the data and the imaging system [P3].

Parallel computing plays an important role in decreasing the reconstruction time. In order to calculate the reconstructions in a shorter time, GPU and SIMD extensions of the processors have been utilized before [82], [83]. We used a computer grid for the MAPEM reconstructions in this study. For the single tilt axis geometry, we split the volume into slices and reconstructed each slice independently in parallel. For the SPR applications, we calculated the forward and backward projections in parallel at each iteration. Furthermore, we developed the multiresolution reconstruction for MAPEM [P3, P4]. The method decreased the computation time significantly and helped suppressing the noise throughout the iterations. Ordered subsets method is another way of decreasing the computation time in tomographic reconstruction [84]. The method splits the projection data into subsets. At each iteration, the reconstructed image is updated using these subsets instead of using all the projection data available. When there is a large block of missing projections and the SNR is low, the method can exaggerate the noise throughout the iterations. Therefore, we preferred multiresolution method in this study.

Simulations with numerical phantoms provide information about the capabilities of the reconstruction methods to some extent. It is hard to simulate all aspects of the data acquisition and the interaction of the electrons with the target. Gold particles can be utilized to detect some artifacts in the reconstruction of the experimental datasets. However, the information they provide and their applicability are limited. FSC have been the gold standard for the evaluation of the reconstructions with the experimental datasets. Therefore, we used FSC in this study as the reference free evaluation method. Another reference free evaluation method that is used in molecular electron microscopy is the noise-compensated leave one out (NLOO) method [85]. The method reconstructs the volume excluding one projection image at a time. Then, the projection of the reconstructed volume in the direction of the angle excluded is calculated. This calculated projection is compared with the measured one via FRC. By repeating this analysis for all the projection angles, the resolution is evaluated with respect to tilt angle. The FSC and NLOO methods give similar results for small tilt intervals. NLOO can be more reliable than FSC for bigger intervals. However, NLOO is computationally more expensive than FSC, since it requires reconstruction for each tilt angle while two reconstructions are enough for FSC.

In conclusion, the MAPEM reconstruction methods developed in this study can compensate for the missing projections and noise. The reconstructions with phantom and experimental datasets have demonstrated that the proposed methods provide better accuracy and resolution than the conventional reconstruction methods. The multiresolution reconstruction shortened the computation time and the adaptive regularization improved the usability of the methods. The proposed laWF method increased the class averaging accuracy in SPR. The methods provided in this study are useful to enhance our understanding of complex biological structures from molecular to cellular level, which can enable developing effective vaccines against viral diseases.

References

[1] J.-J. Fernandez, “Computational methods for electron tomography,” *Micron*, vol. 43, no. 10, pp. 1010–1030, 2012.

[2] D. N. Mastronarde, “Dual-axis tomography: an approach with alignment methods that preserve resolution.,” *J. Struct. Biol.*, vol. 120, no. 3, pp. 343–52, Dec. 1997.

[3] P. Penczek, M. Marko, K. Buttle, and J. Frank, “Double-tilt electron tomography.,” *Ultramicroscopy*, vol. 60, no. 3, pp. 393–410, Oct. 1995.

[4] S. Lanzavecchia, F. Cantele, P. L. Bellon, L. Zampighi, M. Kreman, E. Wright, and G. A. Zampighi, “Conical tomography of freeze-fracture replicas: a method for the study of integral membrane proteins inserted in phospholipid bilayers.,” *J. Struct. Biol.*, vol. 149, no. 1, pp. 87–98, 2005.

[5] O. Öktem, “Handbook of Mathematical Methods in Imaging,” O. Scherzer, Ed. New York, NY: Springer New York, 2015, pp. 937–1031.

[6] J. (Joachim) Frank, Ed., *Electron tomography : methods for three-dimensional visualization of structures in the cell*. Albany, NY: Springer, 2006.

[7] F. Amat, D. Castaño-Diez, A. Lawrence, F. Moussavi, H. Winkler, and M. Horowitz, “Alignment of cryo-electron tomography datasets.,” *Methods Enzymol.*, vol. 482, no. C, pp. 343–67, 2010.

[8] S. Brandt, J. Heikkonen, and P. Engelhardt, “Multiphase method for automatic alignment of transmission electron microscope images using markers.,” *J. Struct. Biol.*, vol. 133, no. 1, pp. 10–22, 2001.

[9] F. Amat, F. Moussavi, L. R. Comolli, G. Elidan, K. H. Downing, and M. Horowitz, “Markov random field based automatic image alignment for electron tomography.,” *J. Struct. Biol.*, vol. 161, no. 3, pp. 260–75, Mar. 2008.

[10] K. Song, L. R. Comolli, and M. Horowitz, “Removing high contrast artifacts via digital inpainting in cryo-electron tomography: an application of compressed sensing.,” *J. Struct. Biol.*, vol. 178, no. 2, pp. 108–20, May 2012.

[11] S. S. Brandt and U. Ziese, “Automatic TEM image alignment by trifocal geometry.,” *J. Microsc.*, vol. 222, no. Pt 1, pp. 1–14, Apr. 2006.

[12] S. S. Brandt and V. Kolehmainen, “Structure-from-motion without correspondence from tomographic projections by Bayesian inversion theory.,” *IEEE Trans. Med. Imaging*, vol. 26, no. 2, pp. 238–48, Feb. 2007.

[13] W. C. Moss, S. Haase, J. M. Lyle, D. A. Agard, and J. W. Sedat, “A novel 3D wavelet-based filter for visualizing features in noisy biological data.,” *J. Microsc.*, vol. 219, no. Pt 2, pp. 43–9, Aug. 2005.

[14] W. Jiang, M. L. Baker, Q. Wu, C. Bajaj, and W. Chiu, “Applications of a bilateral denoising filter in biological electron microscopy,” *J. Struct. Biol.*, vol. 144, no. 1–2, pp. 114–122, Oct. 2003.

[15] M. Maiorca, E. Hanssen, E. Kazmierczak, B. Maco, M. Kudryashev, R. Hall, H. Quiney, and L. Tilley, “Improving the quality of electron tomography image volumes using pre-reconstruction filtering.,” *J. Struct. Biol.*, vol. 180, no. 1, pp. 132–42, Oct. 2012.

[16] J. Astola, P. Heinonen, and Y. Neuvo, “On root structures of median and median-type filters,” *IEEE Trans. Acoust.*, vol. 35, no. 8, pp. 1199–1201, Aug. 1987.

[17] S. Alenius and U. Ruotsalainen, “Generalization of median root prior reconstruction.,” *IEEE Trans. Med. Imaging*, vol. 21, no. 11, pp. 1413–20, 2002.

[18] G. Tang, L. Peng, P. R. Baldwin, D. S. Mann, W. Jiang, I. Rees, and S. J. Ludtke, “EMAN2: an extensible image processing suite for electron microscopy.,” *J. Struct. Biol.*, vol. 157, no. 1, pp. 38–46, 2007.

[19] C. V. Sindelar and N. Grigorieff, “An adaptation of the Wiener filter suitable for analyzing images of isolated single particles,” *J. Struct. Biol.*, vol. 176, no. 1, pp. 60–74, Oct. 2011.

[20] M. van Heel, G. Harauz, E. V. Orlova, R. Schmidt, and M. Schatz, “A New Generation of the IMAGIC Image Processing System,” *J. Struct. Biol.*, vol. 116, no. 1, pp. 17–24, 1996.

[21] P. A. Penczek, J. Zhu, and J. Frank, “A common-lines based method for determining orientations for N > 3 particle projections simultaneously,” *Ultramicroscopy*, vol. 63, no. 3–4, pp. 205–218, Jul. 1996.

[22] S. H. W. Scheres, H. Gao, M. Valle, G. T. Herman, P. P. B. Eggermont, J. Frank, and J.-M. Carazo, “Disentangling conformational states of macromolecules in 3D-EM through likelihood optimization,” *Nat. Methods*, vol. 4, no. 1, pp. 27–29, 2007.

[23] N. Wiener, *Extrapolation, interpolation, and smoothing of stationary time series with engineering applications*. Technology Press of the Massachusetts Institute of Technology, 1964.

[24] F. Jin, P. Fieguth, L. Winger, and E. Jernigan, “Adaptive Wiener filtering of noisy images and image sequences,” in *Proceedings 2003 International Conference on Image Processing (Cat. No.03CH37429)*, vol. 2, p. III-349-52.

[25] R. A. Crowther, D. J. DeRosier, and A. Klug, “The Reconstruction of a Three-Dimensional Structure from Projections and its Application to Electron Microscopy,” *Proc. R. Soc. London A Math. Phys. Eng. Sci.*, vol. 317, no. 1530, 1970.

[26] P. A. Penczek, R. A. Grassucci, and J. Frank, “The ribosome at improved resolution: New techniques for merging and orientation refinement in 3D cryo-electron microscopy of biological particles,” *Ultramicroscopy*, vol. 53, no. 3, pp. 251–270, Mar. 1994.

[27] M. Radermacher, T. Wagenknecht, A. Verschoor, and J. Frank, “A new 3-D reconstruction scheme applied to the 50S ribosomal subunit of E. coli.,” *J. Microsc.*, vol. 141, no. Pt 1, p. RP1-RP2, 1986.

[28] M. Hohn, G. Tang, G. Goodyear, P. R. Baldwin, Z. Huang, P. A. Penczek, C. Yang, R. M. Glaeser, P. D. Adams, and S. J. Ludtke, “SPARX, a new environment for Cryo-EM image processing,” *J. Struct. Biol.*, vol. 157, pp. 47–55, 2007.

[29] S. H. W. Scheres, “RELION: implementation of a Bayesian approach to cryo-EM structure determination.,” *J. Struct. Biol.*, vol. 180, no. 3, pp. 519–530, Dec. 2012.

[30] T. R. Shaikh, H. Gao, W. T. Baxter, F. J. Asturias, N. Boisset, A. Leith, and J. Frank, “SPIDER image processing for single-particle reconstruction of biological macromolecules from electron micrographs.,” *Nat. Protoc.*, vol. 3, no. 12, pp. 1941–1974, 2008.

[31] S. H. W. Scheres, R. Núñez-Ramírez, C. O. S. Sorzano, J. M. Carazo, and R. Marabini, “Image processing for electron microscopy single-particle analysis using XMIPP,” *Nat. Protoc.*, vol. 3, no. 6, pp. 977–990, May 2008.

[32] M. Van Heel, R. Portugal, A. Rohou, C. Linnemayr, C. Bebeacua, R. Schmidt, T. Grant, and M. Schatz, “Four-dimensional cryo electron microscopy at quasi atomic resolution:’IMAGIC4D’.,” in *Crystallography of Biological Macromolecules.*, E. Arnold, D. M. Himmel, and M. G. Rossmann, Eds. New York: Wiley, 2011, pp. 624–628.

[33] A. H. Delaney and Y. Bresler, “Globally convergent edge-preserving regularized reconstruction: an application to limited-angle tomography.,” *IEEE Trans. Image Process.*, vol. 7, no. 2, pp. 204–21, 1998.

[34] P. A. Penczek, “Fundamentals of three-dimensional reconstruction from projections.,” *Methods Enzymol.*, vol. 482, no. C, pp. 1–33, 2010.

[35] P. Gilbert, “Iterative methods for the three-dimensional reconstruction of an object from projections,” *J. Theor. Biol.*, vol. 36, no. 1, pp. 105–117, Jul. 1972.

[36] J. Frank, M. Radermacher, P. Penczek, J. Zhu, Y. Li, M. Ladjadj, and A. Leith, “SPIDER and WEB: Processing and Visualization of Images in 3D Electron Microscopy and Related Fields,” *J. Struct. Biol.*, vol. 116, no. 1, pp. 190–199, 1996.

[37] M. Radermacher, “Weighted Back-Projection Methods,” in *Electron Tomography*, Boston, MA: Springer US, 1992, pp. 91–115.

[38] A. Zürner, M. Döblinger, V. Cauda, R. Wei, and T. Bein, “Discrete tomography of demanding samples based on a modified SIRT algorithm.,” *Ultramicroscopy*, vol. 115, pp. 41–9, Apr. 2012.

[39] D. Wolf, A. Lubk, and H. Lichte, “Weighted simultaneous iterative reconstruction technique for single-axis tomography.,” *Ultramicroscopy*, vol. 136, pp. 15–25, 2014.

[40] D. J. De Rosier and A. Klug, “Reconstruction of Three Dimensional Structures from Electron Micrographs,” *Nature*, vol. 217, no. 5124, pp. 130–134, 1968.

[41] N. R. Voss, D. Lyumkis, A. Cheng, P.-W. Lau, A. Mulder, G. C. Lander, E. J. Brignole, D. Fellmann, C. Irving, E. L. Jacovetty, A. Leung, J. Pulokas, J. D. Quispe, H. Winkler, C. Yoshioka, B. Carragher, and C. S. Potter, “A Toolbox for ab initio 3-D reconstructions in single-particle electron microscopy,” *J. Struct. Biol.*, vol. 169, no. 3, pp. 389–398, Mar. 2010.

[42] G. Harauz and M. van Heel, “Exact filters for general three-dimensional reconstruction,” *Optik (Stuttg).*, vol. 73, pp. 146–156, 1986.

[43] U. Tuna, A. Sohlberg, and U. Ruotsalainen, “Can We Reduce SPECT Acquisition Time Using MAP-EM Reconstruction?,” *J. Pattern Recognit. Intell. Syst.*, vol. 1 (3), pp. 54–63, 2013.

[44] J. A. Fessler and A. O. Hero, “Penalized maximum-likelihood image reconstruction using space-alternating generalized EM algorithms.,” *IEEE Trans. Image Process.*, vol. 4, no. 10, pp. 1417–29, 1995.

[45] T. Hebert and R. Leahy, “A generalized EM algorithm for 3-D Bayesian reconstruction from Poisson data using Gibbs priors.,” *IEEE Trans. Med. Imaging*, vol. 8, no. 2, pp. 194–202, 1989.

[46] S. H. W. Scheres, “A Bayesian View on Cryo-EM Structure Determination,” *J. Mol. Biol.*, vol. 415, no. 2, pp. 406–418, 2012.

[47] A. Kucukelbir, F. J. Sigworth, and H. D. Tagare, “A Bayesian adaptive basis algorithm for single particle reconstruction.,” *J. Struct. Biol.*, vol. 179, no. 1, pp. 56–67, Jul. 2012.

[48] D. Lyumkis, A. F. Brilot, D. L. Theobald, and N. Grigorieff, “Likelihood-based classification of cryo-EM images using FREALIGN.,” *J. Struct. Biol.*, vol. 183, no. 3, pp. 377–388, Sep. 2013.

[49] S. H. W. Scheres, “A Bayesian view on cryo-EM structure determination.,” *J. Mol. Biol.*, vol. 415, no. 2, pp. 406–418, 2012.

[50] F. J. Sigworth, P. C. Doerschuk, J. M. Carazo, and S. H. W. Scheres, “An introduction to maximum-likelihood methods in cryo-EM.,” *Methods Enzymol.*, vol. 482, no. C, pp. 263–294, 2010.

[51] S. H. W. Scheres, “Classification of structural heterogeneity by maximum-likelihood methods.,” *Methods Enzymol.*, vol. 482, no. C, pp. 295–320, 2010.

[52] W. Kühlbrandt, “Biochemistry. The resolution revolution.,” *Science*, vol. 343, no. 6178, pp. 1443–1444, Mar. 2014.

[53] H. Hurwitz, “Entropy reduction in Bayesian analysis of measurements,” *Phys. Rev. A*, vol. 12, no. 2, pp. 698–706, Aug. 1975.

[54] G. T. Herman, H. Hurwitz, A. Lent, and H.-P. Lung, “On the Bayesian approach to image reconstruction,” *Inf. Control*, vol. 42, no. 1, pp. 60–71, Jul. 1979.

[55] K. M. Hanson and G. W. Wecksung, “Bayesian approach to limited-angle reconstruction in computed tomography,” *Journal of the Optical Society of America*, vol. 73, no. 11. p. 1501, 1983.

[56] L. A. Shepp and Y. Vardi, “Maximum likelihood reconstruction for emission tomography.,” *IEEE Trans. Med. Imaging*, vol. 1, no. 2, pp. 113–22, 1982.

[57] A. P. Dempster, N. M. Laird, and D. B. Rubin, “Maximum Likelihood from Incomplete Data via the EM Algorithm,” *Journal of the Royal Statistical Society. Series B (Methodological)*, vol. 39. WileyRoyal Statistical Society, pp. 1–38, 1977.

[58] P. J. Green, “Bayesian reconstructions from emission tomography data using a modified EM algorithm,” *IEEE Trans. Med. Imaging*, vol. 9, no. 1, pp. 84–93, Mar. 1990.

[59] G. T. Herman and D. Odhner, “Performance evaluation of an iterative image reconstruction algorithm for positron emission tomography,” *IEEE Trans. Med. Imaging*, vol. 10, no. 3, pp. 336–346, 1991.

[60] J. You, J. Wang, and Z. Liang, “Range Condition and ML-EM Checkerboard Artifacts,” *IEEE Trans. Nucl. Sci.*, vol. 54, no. 5, pp. 1696–1702, Oct. 2007.

[61] M. V Ranganath, A. P. Dhawan, and N. Mullani, “A multigrid expectation maximization reconstruction algorithm for positron emission tomography.,” *IEEE Trans. Med. Imaging*, vol. 7, no. 4, pp. 273–8, 1988.

[62] A. Raheja and A. P. Dhawan, “Multiresolution expectation maximization reconstruction algorithm for positron emission tomography using wavelet processing,” in *Proceedings of the 20th Annual International Conference of the IEEE Engineering in Medicine and Biology Society*, 1998, vol. 2, pp. 759–762.

[63] S. V Venkatakrishnan, L. F. Drummy, M. A. Jackson, M. De Graef, J. Simmons, and C. A. Bouman, “A model based iterative reconstruction algorithm for high angle annular dark field-scanning transmission electron microscope (HAADF-STEM) tomography.,” *IEEE Trans. Image Process.*, vol. 22, no. 11, pp. 4532–44, 2013.

[64] A. Dabravolski, K. J. Batenburg, and J. Sijbers, “A multiresolution approach to discrete tomography using DART.,” *PLoS One*, vol. 9, no. 9, p. e106090, 2014.

[65] A. Iudin, P. K. Korir, J. Salavert-Torres, G. J. Kleywegt, and A. Patwardhan, “EMPIAR: a public archive for raw electron microscopy image data,” *Nat. Methods*, vol. 13, no. 5, pp. 387–388, Mar. 2016.

[66] A. Nans, M. Kudryashev, H. R. Saibil, and R. D. Hayward, “Structure of a bacterial type III secretion system in contact with a host membrane in situ.,” *Nat. Commun.*, vol. 6, p. 10114, 2015.

[67] M. van Heel and M. Schatz, “Fourier shell correlation threshold criteria.,” *J. Struct. Biol.*, vol. 151, no. 3, pp. 250–62, 2005.

[68] M. E. Martone, A. Gupta, M. Wong, X. Qian, G. Sosinsky, B. Ludäscher, and M. H. Ellisman, “A cell-centered database for electron tomographic data,” *J. Struct. Biol.*, vol. 138, no. 1–2, pp. 145–155, Apr. 2002.

[69] K. Knoops, M. Kikkert, S. H. E. van den Worm, J. C. Zevenhoven-Dobbe, Y. van der Meer, A. J. Koster, A. M. Mommaas, and E. J. Snijder, “SARS-coronavirus replication is supported by a reticulovesicular network of modified endoplasmic reticulum.,” *PLoS Biol.*, vol. 6, no. 9, p. e226, Sep. 2008.

[70] S. P. Mallick, B. Carragher, C. S. Potter, and D. J. Kriegman, “ACE: Automated CTF Estimation,” *Ultramicroscopy*, vol. 104, no. 1, pp. 8–29, 2005.

[71] L. Paavolainen, “Algorithms and software for biological multiscale image analysis,” Doctoral Thesis, Information Technology, University of Jyvaskyla, Finland, 2013.

[72] A. Abdollahzadeh, “Assessing Data Acquisition Approaches in Electron Tomography,” Master’s Thesis, Department of Signal Processing, Tampere University of Technology, Finland, 2016.

[73] “Methods and Models for Biological Signals and Images.” [Online]. Available: http://www.cs.tut.fi/sgn/m2obsi/.

[74] F. H. P. van Velden, R. W. Kloet, B. N. M. van Berckel, C. F. M. Molthoff, A. A. Lammertsma, and R. Boellaard, “Gap filling strategies for 3-D-FBP reconstructions of High-Resolution Research Tomograph scans.,” *IEEE Trans. Med. Imaging*, vol. 27, no. 7, pp. 934–42, 2008.

[75] M. Bertalmio, G. Sapiro, V. Caselles, and C. Ballester, “Image inpainting,” in *Proceedings of the 27th annual conference on Computer graphics and interactive techniques - SIGGRAPH ’00*, 2000, vol. 2, no. 5, pp. 417–424.

[76] I. Aganj, A. Bartesaghi, M. Borgnia, H. Y. Liao, G. Sapiro, and S. Subramaniam, “Regularization for inverting the Radon transform with wedge consideration,” in *2007 4th IEEE International Symposium on Biomedical Imaging: From Nano to Macro*, 2007, pp. 217–220.

[77] R. Leary, Z. Saghi, P. A. Midgley, and D. J. Holland, “Compressed sensing electron tomography.,” *Ultramicroscopy*, vol. 131, pp. 70–91, Aug. 2013.

[78] B. Goris, W. Van den Broek, K. J. Batenburg, H. Heidari Mezerji, and S. Bals, “Electron tomography based on a total variation minimization reconstruction technique,” *Ultramicroscopy*, vol. 113, pp. 120–130, Feb. 2012.

[79] P. Hansen, *Rank-deficient and discrete ill-posed problems: numerical aspects of linear inversion*. Society for Industrial and Applied Mathematics, 1998.

[80] K. Hämäläinen, A. Kallonen, V. Kolehmainen, M. Lassas, K. Niinimäki, and S. Siltanen, “Sparse Tomography,” *SIAM J. Sci. Comput.*, vol. 35, no. 3, pp. B644–B665, 2013.

[81] K. Niinimäki, M. Lassas, K. Hämäläinen, A. Kallonen, V. Kolehmainen, E. Niemi, and S. Siltanen, “Multi-resolution parameter choice method for total variation regularized tomography,” *ArXiv e-prints*, 2014.

[82] W. Xu, F. Xu, M. Jones, B. Keszthelyi, J. Sedat, D. Agard, and K. Mueller, “High-performance iterative electron tomography reconstruction with long-object compensation using graphics processing units (GPUs).,” *J. Struct. Biol.*, vol. 171, no. 2, pp. 142–53, 2010.

[83] J. I. Agulleiro, E. M. Garzón, I. García, and J. J. Fernández, “Vectorization with SIMD extensions speeds up reconstruction in electron tomography.,” *J. Struct. Biol.*, vol. 170, no. 3, pp. 570–5, 2010.

[84] H. M. Hudson and R. S. Larkin, “Accelerated image reconstruction using ordered subsets of projection data.,” *IEEE Trans. Med. Imaging*, vol. 13, no. 4, pp. 601–9, 1994.

[85] G. Cardone, K. Grünewald, and A. C. Steven, “A resolution criterion for electron tomography based on cross-validation.,” *J. Struct. Biol.*, vol. 151, no. 2, pp. 117–29, Aug. 2005.

Publications

Publication I

L. Paavolainen*, E. Acar*, U. Tuna, S. Peltonen, T. Moriya, P. Soonsawad, V. Marjomäki, R. H. Cheng, and U. Ruotsalainen, “Compensation of missing wedge effects with sequential statistical reconstruction in electron tomography”, PLoS One, vol. 9, no. 10, p. e108978, October 2014 (*:equal contribution).

OPEN ACCESS Freely available online

PLOS ONE

Compensation of Missing Wedge Effects with Sequential Statistical Reconstruction in Electron Tomography

Lassi Paavolainen[1☯], Erman Acar[2,3☯], Uygar Tuna[2], Sari Peltonen[2,3], Toshio Moriya[2,3], Pan Soonsawad[4,5], Varpu Marjomäki[1], R. Holland Cheng[4]*, Ulla Ruotsalainen[2,3]*

1 Department of Biological and Environmental Science/Nanoscience Center, University of Jyväskylä, Jyväskylä, Finland, 2 Department of Signal Processing, Tampere University of Technology, Tampere, Finland, 3 BioMediTech, Tampere University of Technology, Tampere, Finland, 4 Department of Molecular and Cellular Biology, University of California Davis, Davis, California, United States of America, 5 Department of Anatomy, Faculty of Dentistry, Mahidol University, Bangkok, Thailand

Abstract

Electron tomography (ET) of biological samples is used to study the organization and the structure of the whole cell and subcellular complexes in great detail. However, projections cannot be acquired over full tilt angle range with biological samples in electron microscopy. ET image reconstruction can be considered an ill-posed problem because of this missing information. This results in artifacts, seen as the loss of three-dimensional (3D) resolution in the reconstructed images. The goal of this study was to achieve isotropic resolution with a statistical reconstruction method, sequential maximum a posteriori expectation maximization (sMAP-EM), using no prior morphological knowledge about the specimen. The missing wedge effects on sMAP-EM were examined with a synthetic cell phantom to assess the effects of noise. An experimental dataset of a multivesicular body was evaluated with a number of gold particles. An ellipsoid fitting based method was developed to realize the quantitative measures elongation and contrast in an automated, objective, and reliable way. The method statistically evaluates the sub-volumes containing gold particles randomly located in various parts of the whole volume, thus giving information about the robustness of the volume reconstruction. The quantitative results were also compared with reconstructions made with widely-used weighted backprojection and simultaneous iterative reconstruction technique methods. The results showed that the proposed sMAP-EM method significantly suppresses the effects of the missing information producing isotropic resolution. Furthermore, this method improves the contrast ratio, enhancing the applicability of further automatic and semi-automatic analysis. These improvements in ET reconstruction by sMAP-EM enable analysis of subcellular structures with higher three-dimensional resolution and contrast than conventional methods.

Citation: Paavolainen L, Acar E, Tuna U, Peltonen S, Moriya T, et al. (2014) Compensation of Missing Wedge Effects with Sequential Statistical Reconstruction in Electron Tomography. PLoS ONE 9(10): e108978. doi:10.1371/journal.pone.0108978

Editor: Eve-Isabelle Pecheur, UMR Inserm U1052/CNRS 5286, France

Received May 9, 2014; **Accepted** August 25, 2014; **Published** October 3, 2014

Data Availability: The authors confirm that all data underlying the findings are fully available without restriction. All relevant data are within the paper and its Supporting Information files.

Funding: Funding provided by National Institute of Health (AI095382) http://www.nih.gov/, National Institute of Food and Agriculture http://www.csrees.usda.gov/, Tekes FiDiPro, (1913/31/2012) http://www.tekes.fi/en/fidipro/, Discovery Grant (UCDG178969) and Tampere University of Technology Internal Grant http://www.tut.fi/en/. The funders had no role in study design, data collection and analysis, decision to publish, or preparation of the manuscript.

Competing Interests: The authors have declared that no competing interests exist.

* Email: rhch@ucdavis.edu (RHC); ulla.ruotsalainen@tut.fi (UR)

☯ These authors contributed equally to this work.

Introduction

Electron tomography (ET) of cellular samples is a widely used technique for three-dimensional (3D) reconstruction of complex subcellular structures at a resolution enabling the detection of macromolecular complex organizations [1]. Generally, in tomography a 3D model of an object is reconstructed from a collection of two-dimensional (2D) projection images of the sample taken in multiple orientations. In its simplest form, either the sample or the radiation source and detector are rotated around a single axis for full 180 or 360 degrees with fixed intervals (typically 1–2°) while projection images are taken [1]. ET is a combination of this computed tomography and electron microscopy, and fills the resolution gap between the structural methods at the sub-nanometer level, such as single-particle reconstruction, and those at the sub-micrometer level using optical microscopy. In ET, transmission electron microscope (TEM) is used to image typically 200–500nm thick samples [2] eliminating the need for finer sectioning to visualize the sample volume. Using modern sample preparation techniques, like cryo-electron microscopy methods, ET enables studying the physiological mechanisms of subcellular organelles in their native context [1,2].

To understand the highly complex mechanisms of cell activities, like the signal pathways and mechanisms of virus infections, it is crucial to study various aspects of the cell such as the morphological abnormalities of the whole cell, organelles, or intracellular compartment membranes, and localization or distribution changes of related proteins. These phenomena occur in 3D space. However, while the TEM imaging allows a high resolution observation, the images lose the information of the density distribution along the z-direction (direction of the electron beam, depth), occluding the fine features and distance between two objects along this direction. Therefore, the 3D reconstructions of the target objects using ET have been important for these biological studies. However, ET of biological samples holds two

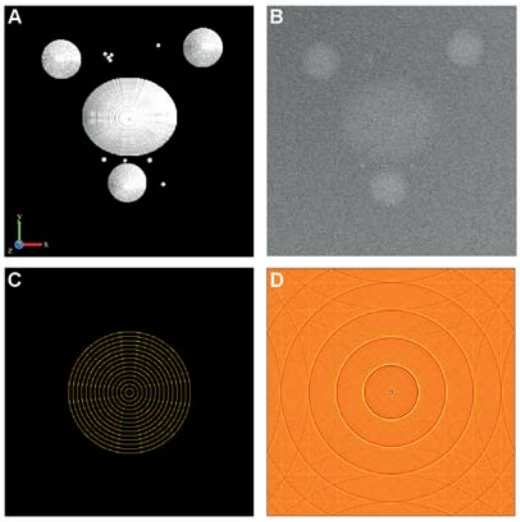

Figure 1. Phantom datasets. Synthetic datasets generated in the study for quantitative analysis with known truth. A) Surface rendering of the cell phantom dataset. B) Zero tilt projection of the cell phantom with 16.1% noise contamination according to the coefficient-of-variation test. C) The artificial pattern synthesized to observe missing wedge effects in the frequency domain. D) The spatial domain image corresponding to the artificial pattern.
doi:10.1371/journal.pone.0108978.g001

major limitations in image acquisition of tilt series for tomography: a limited range of observable tilt angles and an extremely low signal-to-noise ratio (SNR). In the general case, the sample cannot be imaged in full 180° tilt angle range since the structure of the sample holder and limited space between the pole pieces of the objective lens prevent acquiring images with high tilt angles [3]. This missing angular range is known as *missing wedge*. In addition, at 60° tilt angle, the electron beam has to pass approximately twice as much material of the slab-shaped sample as at zero degree [4]. This makes the quality of high tilt angle images worse. Typically, ±60°–70° tilt angle range is used in ET. Together, these technological challenges cause anisotropic resolution seen as elongation and blurring of the objects in the z-direction. In order to reduce the missing information and minimize these artifacts, additional data is acquired from different tilt axes (double tilt axis [5,6], conical tilt axis [7]). The missing wedge is reduced to a missing pyramid with double tilt axis, and a missing cone with conical tilt axis by increasing the information coverage in the Fourier domain. Nevertheless, the usage of these techniques has not been as widespread as single axis tilting because they are technically demanding. They require a more complex sample holder and the alignment of the projections is more complicated in comparison with the single axis tilting geometry. Moreover, the total dose of electrons received by the specimen increases by twice with the double tilt geometry. An excess of electron dose damages target objects in a sample by destroying the smallest details, and can induce deformation such as shrinkage in the beam direction [4]. To avoid possible damages to objects, it is important to keep the cumulative electron dosage as low as possible. However, the low electron dosage decreases SNR, and as such, also detectable resolution. A compromise between the number of projections and the used dosage on each projection needs to be found to maximize the resolution of the imaged object.

The most used image reconstruction methods in ET are weighted backprojection (WBP) [8,9] and simultaneous iterative reconstruction technique (SIRT) [10], due to their simplicity and wide availability in tomographic reconstruction software packages. However, WBP is sensitive to the missing wedge and can result in severe artifacts in limited angle tomography such as ET [11]. SIRT is an iterative method that approximates 3D volume by minimizing the difference between the original projections and projections of the reconstructed volume. It was developed to be usable also in ET with large missing wedge using a sparse set of projections. However, it does not fill the missing wedge and is not able to handle varying sample depth between low and high tilt angles [12]. Recently, a SIRT method using WBP in initialization and backprojection steps was presented [13] to improve reconstruction compared with either of the methods separately.

Regularization and *a priori* knowledge have been used to reduce artifacts, which are common in traditional reconstruction methods used for ET. Angle dependent non-linear anisotropic diffusion filtering [14] has been applied to projection images to compensate the varying depth of the sample. To compensate the missing wedge, total variation and directional smoothing [15] was applied to projection images. Shape-based regularization using prior models of particles included in the sample [16] and segmented mask as a prior in modified SIRT [17] were presented recently. However, in general ET reconstruction problem, no *a priori* knowledge of the objects in the sample is available, unless external objects, such as colloidal gold particles, are added into the sample. Recently, compressed sensing was applied to ET reconstruction to reduce artifacts caused by the missing wedge [18,19]. Compressed sensing reconstruction methods require *a priori* knowledge of the sparse representation of the objects in the sample. This representation was provided by the image gradient, improving especially boundary regions in the reconstructions.

The goal of this study was to gain isotropic resolution for which we applied a new statistical image reconstruction method in ET, capable of correcting the effects of the missing wedge even when *a priori* knowledge of the objects is not available. Statistical methods have been used in e.g. emission tomography (PET, SPECT) to successfully reconstruct 3D images from noisy projection data [20–22]. For this study, we chose the sequential maximum a posteriori expectation maximization (sMAP-EM) method [20], which searches for the most likely cross-sectional images given the measured projections from TEM. We regularized the iterative reconstruction with a median filtered image of the previous iteration in a weighted one-step late algorithm to control the noise in the reconstructed images [23]. The reconstruction was expected to estimate values for the missing wedge during the iterations and to form a 3D image from the measurements. Instead of running the iterative reconstruction once to convergence with a chosen weight for the regularization, we applied the method sequentially. In these sequences, the previous result was initializing the successive one while the weight of the regularization was gradually decreased sequence by sequence. By this way, sMAP-EM improves the image quality step by step during the sequences.

To evaluate sMAP-EM reconstruction method, we utilized synthetic cell datasets and an experimental data consisting of several gold particles as test targets. Gold particles with known shape and size are often used as reference objects in biological samples. An automatic ellipsoid fitting based method, utilizing this knowledge about the gold particles, was developed in this study to measure elongation and contrast in the reconstructions. We compared sMAP-EM reconstructions with the WBP and SIRT

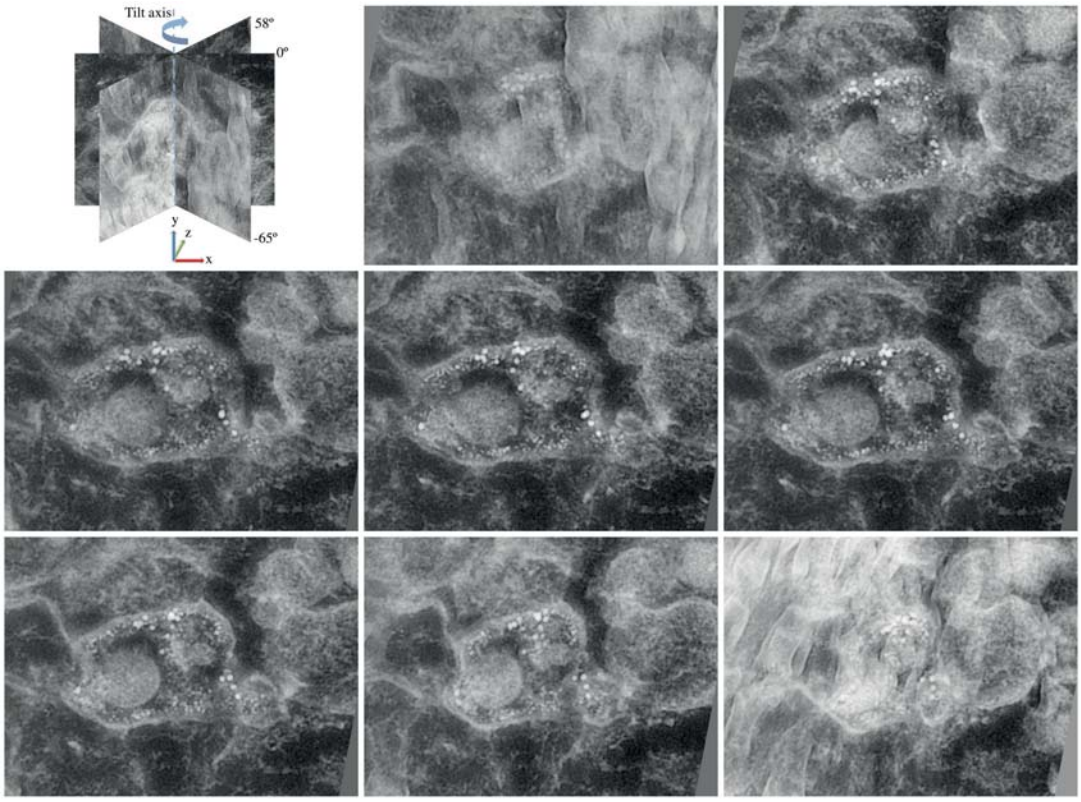

Figure 2. Experimental vesicle data. Altogether 124 projections of the experimental data were taken approximately from -65° to 58° tilt angle range with 1° increments. The experimental data includes a multivesicular body, intraluminal vesicles and gold particles of two diameters. Projection tilt angles from left to right, and from top to bottom: -64.97°, -46.93°, -29.00°, -11.97°, 6.16°, 24.04°, 41.07°, 58.05°. Projections are presented with inverted intensities to improve the visualization.
doi:10.1371/journal.pone.0108978.g002

results. All the qualitative and quantitative evaluations showed that the sMAP-EM image reconstruction method gives the best isotropic results and the best contrast in the images.

Materials and Methods

Datasets

Cell phantoms. The cell phantom (Figure 1A,B) was created in order to test the developed method with a realistic numerical phantom of an intracellular structure. The constructed phantom is of the size $512\times512\times128$ in the (x, y, z) directions, with isotropic voxel size of 1 nm. x, y and z axes are defined as the horizontal axis of the projection images, the tilt axis, and the direction of the electron beam, respectively. It contains 3 large spherical objects mimicking virus particles. Each virus particle has a diameter of 80nm. A large ellipsoidal object representing a cell vesicle was also included. This vesicle was cut in half from the middle z-section emulating the microtomy process. The lengths of the axes of this vesicle are 102, 85 and 51nm. Virus particles and vesicle were created using textures from the reconstruction of experimental data. Additionally, 11 small and dense spherical objects presenting gold particles were added. These gold particles, having diameter 7, 9 and 11nm, had high density to simulate TEM imaging. Non-uniform background density was set to smoothly vary 2.4% between the minimum and maximum density. Virtual projections were calculated with 1° increment using four different tilt angle ranges ($\pm40^\circ$, $\pm50^\circ$, $\pm60^\circ$, $\pm70^\circ$) to vary the size of the missing wedge. With the addition of noise to the projection data, two main components of noise in experimental TEM projections were simulated; Poisson noise due to electron counting and Gaussian noise due to the CCD sensor. The obtained projections were contaminated with two different levels corresponding to approximately 16.1% (noise level 1, NL 1, Figure 1B) and 18.0% (noise level 2, NL 2) noise contamination according to the coefficient-of-variation test.

Synthetic pattern for frequency domain analysis for missing wedge area. The analysis was done to study what is produced in the region of missing wedge area by the reconstruction methods and how it evolves with changing tilt angle. For this analysis, first, a well-defined frequency pattern (Figure 1C) was synthesized to better observe how the missing wedge is filled. Then the artificial image (Figure 1D) corresponding to this pattern was obtained with inverse 2D fast Fourier transformation. The amplitudes of the frequencies were adjusted so that there were

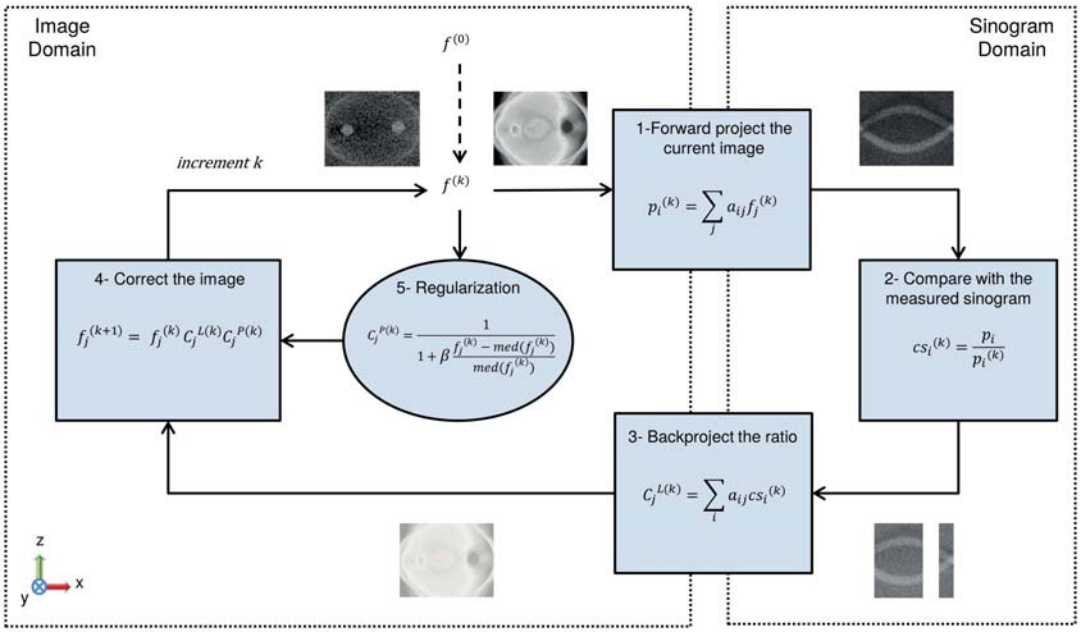

Figure 3. One sequence of the sMAP-EM reconstruction method for a single slice of the sample volume. $f^{(0)}$ is the initial image, $f_j^{(k)}$ is the reconstruction result of the j^{th} pixel at k^{th} iteration, a_{ij} is the system matrix element defining the contribution of the j^{th} pixel to the i^{th} projection, p_i is the i^{th} projection, $med(\cdot)$ is the median filter with a 3×3 kernel size, and β is the predefined sequence dependent coefficient defining the amount of regularization. The blocks (1), (2), and (3) yield the ML-EM correction factor, $C_j^{L(k)}$, and the block (5) yields the a priori correction factor $C_j^{P(k)}$. Two correction factors are combined in the block (4) to update the current estimate.
doi:10.1371/journal.pone.0108978.g003

no pixels with negative values in the spatial domain image. Finally, virtual projections of this image were calculated with 1° increment for ±60° tilt angle range. These projections were reconstructed with all three reconstruction methods. Only for sMAP-EM, projections with the 10° increment step of the wedge size were reconstructed for finer observation (Figure S3).

Experimental vesicle data. An experimental sample of a multivesicular body (MVB) (Figure 2) was prepared by high-pressure freezing and freeze substitution as in [24]. The sample was used to study breakages in the membranes of virus-induced MVB and intraluminal vesicles suggesting genome release to the cytoplasm. Also, two specific targets, echovirus 1 and α2β1-integrin receptor, were labeled with gold particles of 14nm and 6 nm of size, respectively, to study the localization and distribution of these targets in the virus-induced MVB. A series of single axis TEM images were obtained with the JEM-2100F Field Emission Electron Microscope (JEOL Ltd., Tokyo, Japan) at a voltage of 200 kV. It comprises 124 images of the MVB taken at an interval of approximately 1° in the angular range [−65°, +58°], with the magnification of 10k. Before reconstruction, the projection images were aligned by cross-correlation using the 14nm gold particles as markers. The dimensions of the original projection images were 4096×4096 which were cropped to size 958×712 pixels used for reconstruction. The pixel size was 1nm.

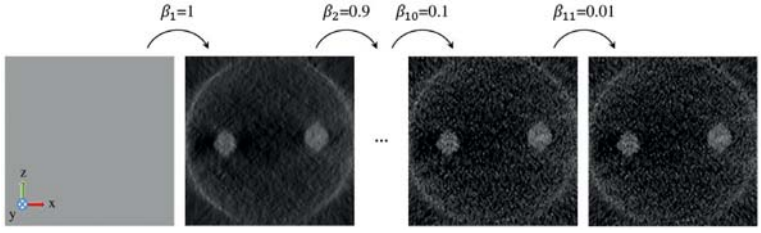

Figure 4. Sequential adaptation of the regularization weight, β. The sequences are initialized with an image of ones (the leftmost image). At the end of sequences with decreased β values, the final reconstruction image is obtained (the rightmost image). In total, 1000 iterations are performed in 11 sequences.
doi:10.1371/journal.pone.0108978.g004

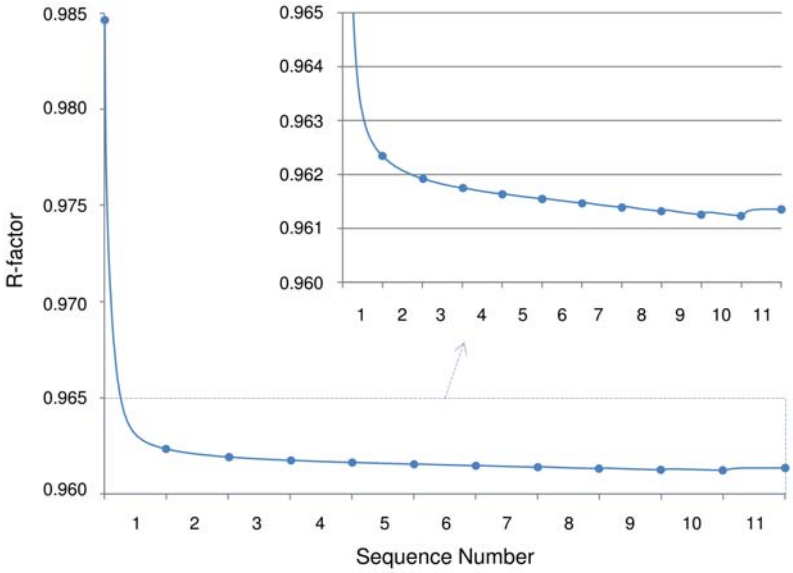

Figure 5. Illustration of the change of the R-factor throughout the iterations. R-factor decreases smoothly during the first 10 sequences. At the final sequence, a small increase is observed due to the noise contamination while enhancing the resolution and the contrast.
doi:10.1371/journal.pone.0108978.g005

The projection data and reconstructions of all datasets are available at our supplementary data site: http://pioms.ucdavis.edu/pone/smap-em.

Sequential MAP-EM Image Reconstruction Method

Maximum likelihood (ML) estimation was used previously for tomographic reconstruction considering the Poisson nature of the measured data [25]. The method searches for the image maximizing the likelihood of the measured data to occur ($P(Data|Img)$) using the iterative algorithm, expectation maximization (EM). In each ML-EM iteration, the estimated image is projected to the sinogram domain and compared with the measured sinogram proportionally. The result of this comparison is back-projected to the image domain to obtain a correction image which is used to update the current image estimate multiplicatively. The method produces statistically unbiased but noisy images [26]. In order to improve the image quality, a priori probability distribution was used [27–29] based on the Bayes' rule:

$$P(Img|Data) = P(Data|Img)P(Img)/P(Data)$$

where $P(Data|Img)$ is the likelihood function, $P(Img)$ and $P(Data)$ are the a priori probability distributions. $P(Img|Data)$ is the a posteriori probability distribution function to be maximized with EM algorithm in maximum a posteriori expectation maximization (MAP-EM) approaches [30]. Since $P(Data)$ is constant, it does not have influence on the solution. For $P(Img)$, Alenius et al. [23] suggested median root prior, based on the assumption that the intensity values are similar in the small neighborhood of each pixel of the reconstructed image. The advantage of median filtering is that it is good at preserving edges while reducing the noise. In our study, a sequential version of this median root prior based MAP-EM approach [20] was used for solving the missing wedge problem. One sequence of the method is illustrated for a single slice in Figure 3. The blocks (1), (2), and (3) represent the ML-EM approach and the block (5) represents a priori information introduced. In the block (4) the result of ML-EM and a priori information are combined together to update the current estimate. The iterations continue with a constant predefined regularization weight β, in each sequence. The value of β is varied throughout the sequences as shown in Figure 4.

The first sequence was initialized with an image of a non-zero value and the value of β was set to 1 which corresponds to full regularization. The successive sequences were initialized with the resulting image of the previous one and the β value was decreased gradually sequence by sequence. It was reduced to 0.1 linearly in 10 steps and the final sequence was performed with $\beta = 0.01$. By decreasing the β value, the blurring effect of the regularization filter was reduced. Therefore the resolution and the intensity contrast were enhanced. However, β was never set to 0 in order to avoid checkerboard artifacts observed when a high number of iterations is used without regularization [31]. The number of iterations in each sequence of sMAP-EM was chosen to be sufficiently large to satisfy convergence for reconstructions at different noise levels and different samples.

To illustrate the change in the reconstructed image during sequences, the R-factor was calculated using a small region of interest (ROI) including a virus particle in one slice of the cell phantom (NL1) data as:

$$R = \frac{\sum_{j \in ROI} |f'_j - f_j|}{\sum_{j \in ROI} |f'_j|}$$

where f_j is the reconstruction result and f'_j is the ground truth of the j^{th} pixel. The change in the R-factor throughout the sequences

is shown in Figure 5. For the first 10 sequences, R-factor decreases smoothly during the iterations. At the final sequence, the decrease of β value from 0.1 to 0.01 introduces some noise to the image which yields a small increase in the R-factor curve. However, by decreasing the weight of the low pass regularization filter, the visual quality of the image is enhanced at the final sequence in terms of the resolution and the contrast.

The reconstruction method was implemented in MATLAB (MathWorks Inc., MA, USA) and the code (available at: https://www.cs.tut.fi/sgn/m2obsi/m2obsiWWW/demos/mapem/MAPEM.html) was run on the computer grid Techila (Techila Technologies Ltd., Tampere, Finland). The sample volume was divided into slices perpendicular to the tilt axis and sMAP-EM was applied to the image of each slice in parallel. The resulting 3D volume was obtained by concatenating the reconstructed 2D images. In CPU time, it took approximately 960 hours for the cell phantom dataset and 4230 hours for the experimental vesicle dataset to obtain the reconstruction results. Approximately 120 AMD 64-bit processor worker computers participated in the experiments. Therefore the reconstruction of the cell phantom data took about 8 hours and the experimental vesicle data about 35 hours.

Conventional reconstruction methods for comparison: WBP & SIRT

Widely used implementations of WBP and SIRT available in Tomo3D software [32] were used to test the methods. The WBP method simply distributes the projection data over the image plane proportionally to the contribution of each image element (pixel). The WBP method can be mathematically expressed as

$$f_j = \sum_i a_{ij} W(p_i), 1 \le j \le m,$$

where f_j is the reconstruction result of the j^{th} pixel, a_{ij} is the system matrix element defining the contribution of the j^{th} pixel to the i^{th} projection, p_i is the i^{th} projection, m is the total number of pixels, and $W(\cdot)$ represents the filtering operation. In this study, a ramp filter and a Hamming filter with cutoff frequency 0.5 cycles/pixel were used in WBP reconstructions. Ramp filter was used to compensate the blurring artifact resulting from simple back-projection and the Hamming filter was used to suppress the high frequency noise amplified by the ramp filter.

SIRT is another well-known reconstruction method which enhances the image iteratively using forward and backward projections. The method is initialized with an arbitrary reconstruction

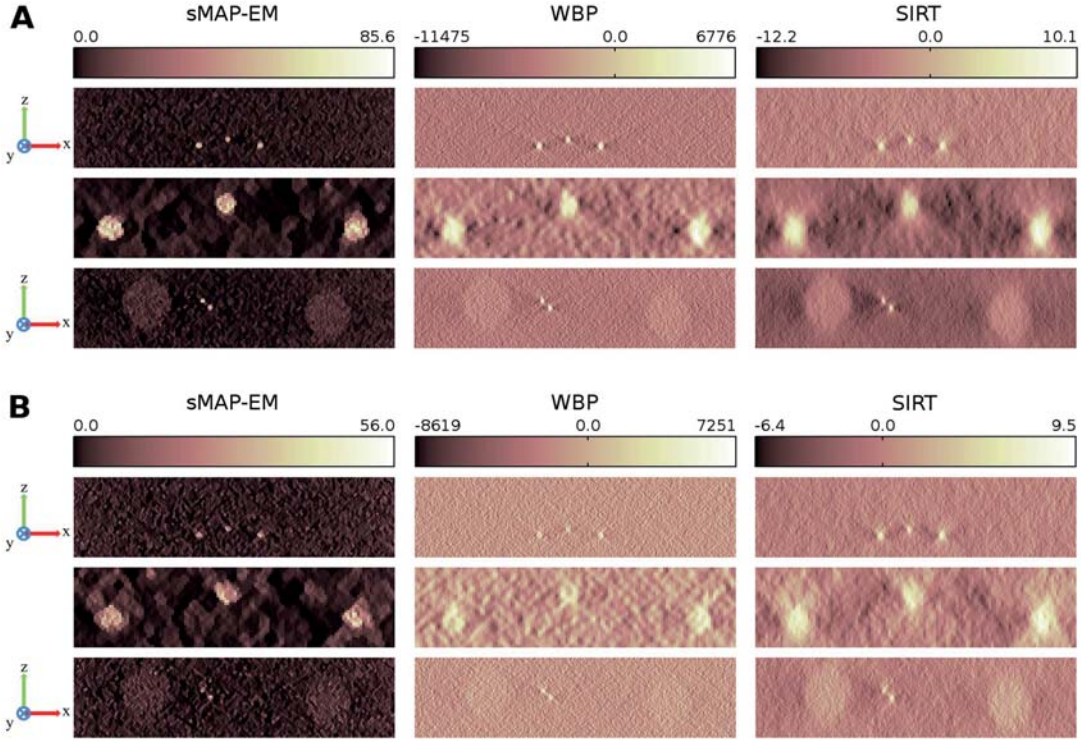

Figure 6. Orthogonal x–z slices from the cell phantom reconstructions. Orthogonal x–z slices from the reconstructions with projections in $\pm 60^{\circ}$ tilt angle range having (A) 16.1% (noise level 1, NL1) and (B) 18.0% (noise level 2, NL2) noise contamination according to the coefficient-of-variation test. Slices show gold particles (top row) and virus particles (bottom row). The middle row images present zoomed region of the gold particles in the top row images. The full dynamic range of raw pixel values is presented with pseudo-color. The artifacts caused by missing wedge are clearly present in the WBP and SIRT reconstructions from NL1 projections, whereas sMAP-EM is able to compensate the missing information better. The reconstructions from NL2 projections have lower contrast and as such, also the artifacts are less visible.
doi:10.1371/journal.pone.0108978.g006

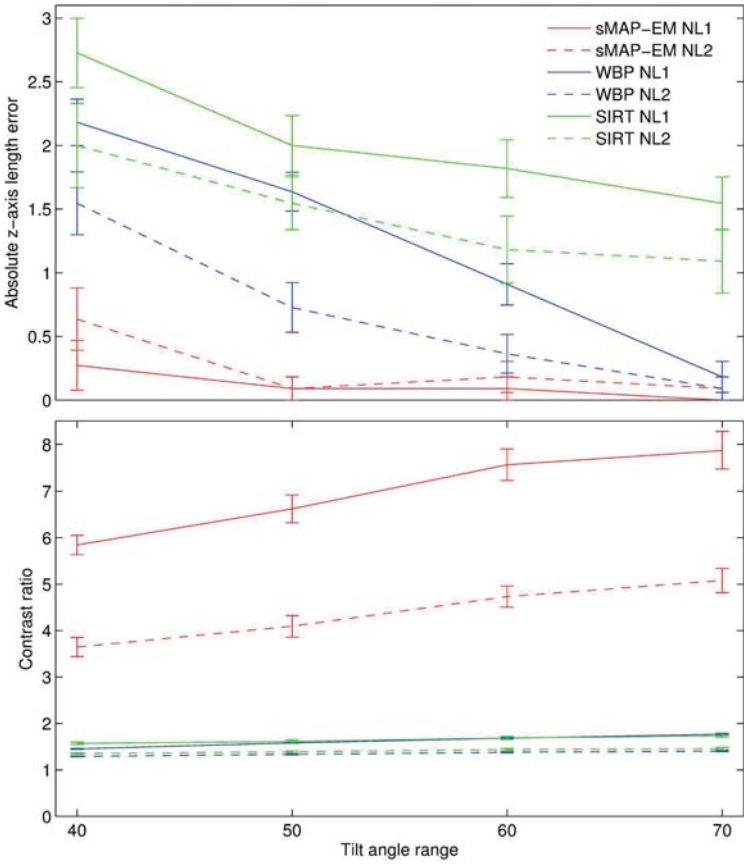

Figure 7. Effects of different missing wedge sizes to absolute z-axis length error and contrast ratio. Measured means and standard errors of the means of the absolute z-axis length errors and the contrast ratios of 11 gold particles in the cell phantom reconstructions. Measurements from the reconstructions of projections with noise level 1 (solid line) and noise level 2 (dashed line) are shown in the same plot. The tilt angle range is affecting the z-direction resolution with all methods. sMAP-EM is clearly the best and has the least effect of increased missing wedge. sMAP-EM gives the best contrast improving with the angular range while the WBP and SIRT reconstructions have low contrast with all tilt angle ranges.
doi:10.1371/journal.pone.0108978.g007

estimate. First, the image is projected to the sinogram domain. Next, the difference between the measured projections and the projections from the current reconstruction is calculated. Finally, the difference is back-projected to the image domain to update the current image estimate. The method can be formulated as [10]:

$$f_j^{(k+1)} = f_j^{(k)} + \sum_i a_{ij} \frac{p_i - \sum_j a_{ij} f_j^{(k)}}{\sum_j a_{ij}^2}, 1 \le j \le m,$$

where $f_j^{(k)}$ is the reconstruction result of the j^{th} pixel at the k^{th} iteration. SIRT with long object compensation was used in this study as proposed by [33]. The method is weighting the projections considering the length of the parallel rays clipped to the bounding box of the reconstruction region to eliminate the artifacts at the boundary of the reconstructed ROI. SIRT was run with 30 iterations in cell phantom data and frequency domain analysis, while 50 iterations were used in experimental vesicle data to improve visual quality. Both iteration numbers are appropriate according to the evaluations made in [33].

Ellipsoid fitting based evaluation methods

Both visual and quantitative evaluations were made from all reconstructions. An objective ellipsoid fitting based method was developed in BioImageXD software [34] to quantitatively measure accuracy and contrast using gold particles in the reconstructed volume. The method generates a set of ellipsoids $x^2/a^2+y^2/b^2+z^2/c^2 = 1$ with varying ellipsoidal parameters $a,b,c \in \mathbb{N}$. Voxels inside the ellipsoids are set as a mask. Normalized cross-correlation is used to find the location of gold particle in the reconstruction from a small volume around the initial location. Parameters of the best fitting ellipsoid for each gold particle are extracted from correlations by selecting the highest correlation coefficient.

In general, low SNR decreases the accuracy of object detection in images. Low SNR also affects the ability of the ellipsoid fitting based method to find a clear gold particle boundary. This applies

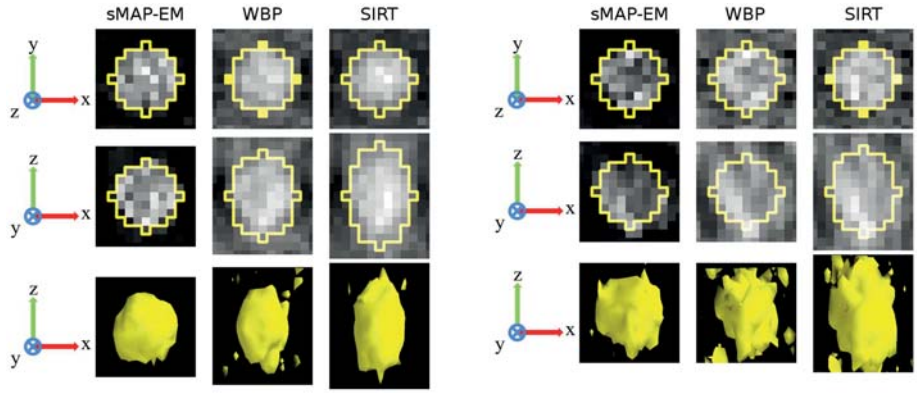

Figure 8. 3D fitted ellipsoids on a representative gold particle in the cell phantom reconstructions. 2D orthogonal x–y (top) and x–z (middle) slices through the center of a 3D fitted ellipsoid drawn over a representative measured gold particle from reconstructions with projections in $\pm 60^\circ$ tilt angle range. Surface rendering of the gold particle (bottom) presents overall shape of the reconstructed gold particle. Isosurface threshold value was selected experimentally for the best visualization. All images are in the same scale. The full dynamic range of each image was used for visualization. Intensity inside the gold particle in the sMAP-EM reconstruction appears to have larger variation than in the WBP and SIRT reconstructions. This results partly from higher smoothing especially in the SIRT reconstruction, but also from the fact that the variation of the background intensity in the WBP and SIRT reconstructions is high and the contrast of the gold particle is low making the inside of the gold particle appear more uniform in the visualization. The contrast of the gold particle is high in the sMAP-EM reconstructions from (A) noise level 1 and (B) noise level 2 projections making fitting accurate. The contrast of the gold particle is much lower in the WBP and SIRT reconstructions especially with noise level 2 projections, reducing the accuracy of the ellipsoid fitting as presented quantifically in Figure S1.
doi:10.1371/journal.pone.0108978.g008

especially for the WBP and SIRT reconstructions, whereas sMAP-EM reconstructions were quantified accurately even with the highest level of noise used. The accuracy of ellipsoid fitting based method was tested in all reconstruction methods using projection images with varying levels of Gaussian noise. The method gives reliable results (see Figure S1) for sMAP-EM with all noise levels. The results are also stable for projections having NL1 or higher SNR, but less reliable for NL2 with WBP and SIRT methods. It can be expected that the ellipsoid fitting method does not give reliable results for the WBP and SIRT reconstructions from projections with lower SNR than in NL2 images. However, the ellipsoid fitting based method can be used to compare different reconstruction methods and data acquisition procedures in an automated, objective, and reliable way under certain amount of noise.

To assess the accuracy in 3D, ground-truth gold particles in the cell phantom data were analyzed. Parameters of fitted ellipsoids were compared with the radius (r) of ground-truth gold particles in the original volume. The fitted ellipsoid axis length absolute error in all directions was calculated as $\mathrm{LAE}_x = |a-r|$, $\mathrm{LAE}_y = |b-r|$ and $\mathrm{LAE}_z = |c-r|$.

In order to measure the effect of the missing wedge on the resolution, elongations in all axes were analyzed from the reconstructions. With isotropic resolution, elongation would be 1.0 in all directions, as gold particles are spherical in the nanometer scale. However, as a result of the missing wedge, the images of the gold particles tend to be elongated especially in the z-direction. Elongations were calculated directly from the fitted ellipsoid parameters in all directions as $e_{yx} = b/a$, $e_{zx} = c/a$ and $e_{zy} = c/b$.

The contrast in the reconstructions was evaluated using contrast ratio (CR) to quantify how well gold particles can be visualized and analyzed. The higher CR values mean higher contrast, and better visibility, in the reconstructed volumes. CR was calculated as

$$\mathrm{CR} = \frac{\sum_{j \in I} f_j / |I|}{\sum_{j \in O} f_j / |O|},$$

where f is the reconstructed volume, $j \in \mathbb{N}^3$ is the voxel index, f_j is the value of voxel j in the volume f, and the sets I and O are the voxels inside and outside the volume of interest (VOI) defined by the fitted ellipsoid, respectively. The voxels outside the VOI were defined to construct a volume around the VOI with the same shape but twice the volume of the VOI.

Results

Synthetic data reconstructions

To observe the effect of noise to the reconstructions, we reconstructed the cell phantom data from two projection noise levels. Figure 6 shows different slices from the reconstructed volumes. sMAP-EM reconstruction shows clearly better contrast in the images. All methods produce results where objects are detectable with lower noise. However, reconstructions of higher noise level are more different. The used SIRT reconstruction with long object compensation clearly includes more smoothing of the data. The WBP and the SIRT reconstructions showed shadows near the objects in the lateral (x–y) plane and clear artifacts in x-z slice due to the missing wedge. The artifacts were more visible in the reconstructions at the lower noise level for the WBP and SIRT methods.

The quantitative evaluations for the accuracy and the CR of 11 gold particles in the cell phantom reconstructions of both noise levels and all four tilt angle ranges ($\pm 40^\circ$, $\pm 50^\circ$, $\pm 60^\circ$, $\pm 70^\circ$) are presented in Figure 7. The results of the ellipsoid fitting method (Figure 8) show that the sMAP-EM reconstruction results are consistently better with extremely good accuracy. The method produced reconstructions with low elongation in the lateral plane

Table 1. Quantitative results for 11 gold particles in the cell phantom reconstruction.

Noise	Method	LAE_x	LAE_z	e_{yx}	e_{zx}	e_{zy}	CR
NL 1	sMAP-EM	0.00±0.00	0.09±0.09	1.00±0.00	1.03±0.03	1.03±0.03	7.57±0.34
	WBP	0.36±0.15	0.91±0.16	1.11±0.05	1.36±0.08	1.23±0.05	1.68±0.02
	SIRT	0.09±0.09	1.82±0.23	1.03±0.03	1.50±0.05	1.46±0.05	1.69±0.04
NL 2	sMAP-EM	0.00±0.00	0.18±0.12	1.00±0.00	1.06±0.04	1.06±0.04	4.73±0.22
	WBP	0.45±0.16	0.36±0.15	1.15±0.06	1.27±0.11	1.09±0.04	1.38±0.01
	SIRT	0.09±0.09	1.18±0.26	1.03±0.03	1.32±0.06	1.29±0.06	1.44±0.02

Quantitative results of cell phantom reconstructions with ±60° tilt angle range. $LAE_{x,z}$ presents mean of fitted ellipsoid axis length absolute error in pixels, $e_{yx,zx,zy}$ is mean ellipsoid elongation and CR is mean contrast ratio. Standard error of the mean is included with the mean values. LAE_y is excluded from the table because none of the methods show any error in fitted ellipsoid y-direction.

doi:10.1371/journal.pone.0108978.t001

(Table 1). The WBP and the SIRT reconstructions show an increase in elongation in the z-direction, as measured by the fitted ellipsoids. The WBP reconstruction also results in elongated gold particle images in the lateral plane. From these results we can see that the sMAP-EM produces the best isotropic resolution in all directions that is close to the ground-truth value.

Contrast and the amount of noise in reconstruction is important for further automatic and semi-automatic analysis and visualization. The effects of different noise levels in projections was studied to see how much different methods are influenced by the noise. We used five different noise levels in projections in ±60° tilt angle range and measured gold particle elongation. With perfect reconstruction method the elongation should be independent of the noise and only dependent of the missing wedge. The results (Figure S1) show that gold particles are analysed reliably from sMAP-EM reconstructions of all noise level projections. The measured elongation increases slightly due to increased noise in the reconstructions. However, the contrast becomes very low especially with the largest noise level in the WBP and SIRT reconstruction preventing reliable automatic measurements of the gold particles seen as sudden drop of the elongation measurement. The CR results (Figure 7) show that the sMAP-EM reconstruction produces much better contrast than the WBP and the SIRT reconstructions. This is visible also in Figures 6 and 8.

To observe how the missing wedge is filled by different reconstruction methods with different wedge sizes, we reconstructed the projections calculated from the synthetic slice shown in Figure 1D. The comparison of the resulting spectra shows that sMAP-EM filled more information in the missing region, while the SIRT and WBP failed to do so (Figure 9). The overall trend of the sMAP-EM reconstructions shows that recovery of the low frequency was more recognizable than that of the high frequency in the missing regions. Furthermore, the accuracy of the filling deteriorated as the wedge angle increased (Figures S2 and S3). The amplitude and connectivity of the bridging decreased with the increasing frequency. In the reconstruction with 60° wedge, the information fillings were recognizable at the edge of the region but were blurry in the middle if there were any, resulting in the disconnection of the bridging arcs. However, the other results like the elongation of the gold particles show that the filled information is useful.

Experimental data reconstructions

3D rendering of the reconstructions (Figure 10) show clear differences between methods especially on the x–z direction where the missing wedge mostly effects. The membrane of the MVB is clearly distinguishable with membrane breakages in all volume renderings (Figure 10A). Membrane of the large intraluminal vesicle is more connected in the sMAP-EM reconstruction. When visualizing the MVB membrane particles from sideview (Figure 10B) the difference in elongation between sMAP-EM and other methods comes clear. sMAP-EM is able to separate particles in the membrane where WBP creates elongated connection. As a result of different background levels, artifacts and contrast, preparation of the visualization is different in sMAP-EM than in WBP and SIRT. The sMAP-EM reconstruction can be directly volume rendered without setting any threshold value whereas often complicated and possibly even biased use of manual thresholding to remove the background have to be done to visualize interesting structures from the WBP and SIRT reconstructions.

In Figure 11, orthogonal slices of the experimental data are presented first in the original scale and then as scaled to positive

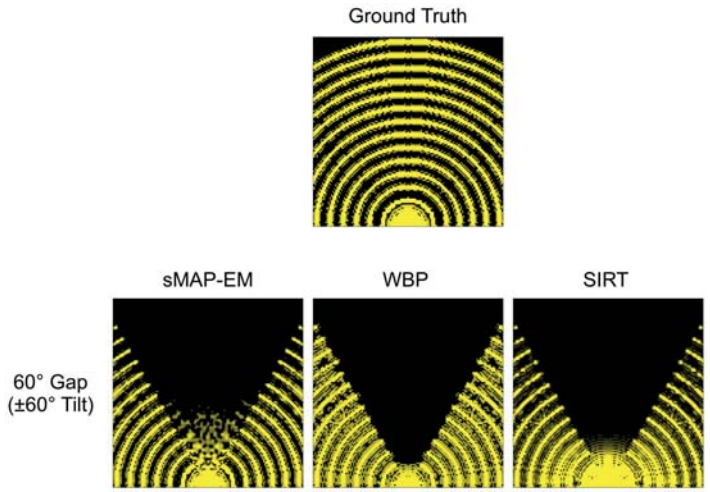

Figure 9. Observation of the missing wedge in the frequency domain. Along with the ground truth, the spectra of the synthetic pattern reconstructed by sMAP-EM, WBP, and SIRT are shown. The width of the missing wedge used is $\pm 60^{\circ}$. For better visual comparison, all amplitudes having lower than a threshold value were set to zero and the spectrum was scaled with the logarithm of base 10; the threshold value and scaling factor were adjusted for each reconstruction method. The filling of the missing wedge by sMAP-EM with meaningful information is supported by quantitative results of gold particle studies presented in Figure 7 and Tables 1 and 2.
doi:10.1371/journal.pone.0108978.g009

values to be comparable. Volumes of the sMAP-EM reconstruction are identical in both full and non-negative dynamic range since this method guarantees the value "zero" to be the baseline indicating no detectable densities. However, WBP and SIRT slices give considerably different visual impressions because the baseline values were not kept to be zero in addition to the negative value artifacts. Effects of these differences on visualization are clear in the zoomed ROIs. The gold particle in the red box is clearly visible in the sMAP-EM reconstruction but show elongation and less contrast in other reconstructions. The green box is located on presumable MVB membrane breakage. Furthermore, an isolated gold particle can be seen above the green box. Its intensity in the bottom visualization supports the superior contrast of sMAP-EM over SIRT and WBP. A bright object on the right-top side in the x-y slice of the sMAP-EM also shows the visibility difference; this was consistent in the z-direction neighbors of x-y slices. In general, the gold particles are much more distinguishable in the sMAP-EM reconstruction compared with the WBP and the SIRT reconstructions. The same can be seen in the ellipsoid fitting (Figure 12, Figure S4) on a gold particle.

The quantitative results of gold particle elongation (Table 2) show that sMAP-EM reduce elongation as compared to WBP and SIRT. This is important when studying connectivity of particles in the z-direction that is the most important direction gained from tomography studies. Gold particles for the ellipsoid fitting based evaluations were identified manually. 20 individual gold particles were detectable in sMAP-EM reconstruction. However, as a result of poor contrast and artifacts in the WBP and the SIRT reconstructions, only 7 isolated gold particles were found. These were used for the quantification in all methods. The results of the ellipsoid fitting based evaluations of isotropic resolution in the reconstructions are presented in Table 2. The sMAP-EM reconstruction was the most symmetric in x, y, and z-directions. The contrast ratio in the sMAP-EM reconstruction was almost three times higher than in other reconstructions. There is no elongation in the images of gold particles in the lateral plane in the SIRT reconstruction. However, the elongation in the z-direction in the SIRT reconstruction with long object compensation is larger than in the sMAP-EM and the WBP reconstructions. The WBP reconstruction shows elongation also in the lateral plane as a result of artifacts in x-direction.

Table 2. Quantitative results for 7 gold particles in the experimental vesicle data.

Method	e_{yx}	e_{zx}	e_{zy}	CR
sMAP-EM	1.01±0.06	1.27±0.07	1.27±0.07	3.01±0.36
WBP	1.14±0.05	1.57±0.09	1.38±0.07	1.18±0.01
SIRT	1.00±0.00	1.67±0.14	1.67±0.14	1.18±0.01

Quantitative results of reconstructions of experimental data. Mean elongation ($e_{yx,zx,zy}$) and mean contrast ratio (CR) of the gold particles are presented with standard error of the mean.
doi:10.1371/journal.pone.0108978.t002

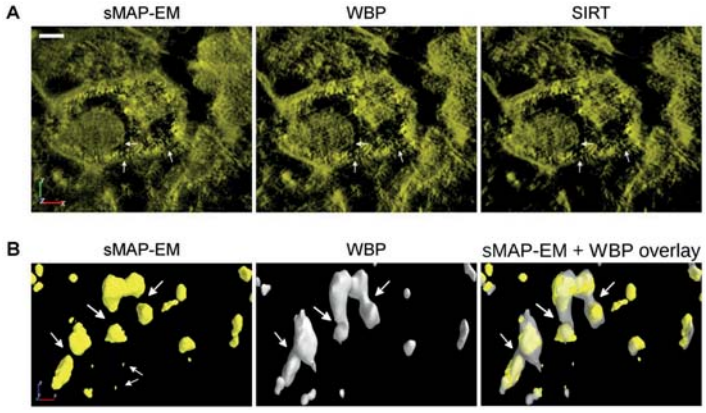

Figure 10. 3D rendering of the experimental vesicle data reconstructions. Volume renderings (A) show that the MVB membrane and its breakages (marked with white arrows) are visible with all reconstruction methods. However, large intraluminal vesicle and its membrane (marked with an arrow) is much more clearly visible in the sMAP-EM reconstruction than in the WBP and SIRT reconstructions. The sMAP-EM reconstruction can be directly volume rendered without any thresholding whereas both WBP and SIRT need a threshold to remove the background to make interesting regions visible. The threshold selection is a qualitative process which can lead to the removal of interesting data while reducing the background. For this figure, the thresholds for WBP and SIRT were selected for the best possible presentation. Scale bar 100nm. MVB membrane structure was further studied with surface rendering (B) from the direction of y-axis. The sMAP-EM reconstruction was compared to WBP which was quantitatively 2 shown to produce less elongation than SIRT. It is clearly visible that sMAP-EM is able to distinguish individual particles (regions marked with arrows) where WBP creates elongated connection. Also small particles (marked with arrows) are visible in the sMAP-EM that are absent in the WBP. The isovalues for surface renderings were selected so that the same percentage of the highest density voxels were included in the surface with both methods.
doi:10.1371/journal.pone.0108978.g010

Discussion

To use the advantages of MAP-EM for the missing wedge and the high noise level in input images, a modified version, ''sMAP-EM'', was applied to the ET reconstruction of the biological samples in this work. Our results with both phantom and experimental datasets demonstrated that the sMAP-EM is consistently superior to the WBP and SIRT methods, in terms of the elongation suppression, 3D resolution, and contrast. The WBP and SIRT severely suffered from the missing wedge while the sMAP-EM handled this information loss better. This way sMAP-EM produced better isotropic resolution. Contrast between interesting and background regions in reconstructed volume determine how accurate automatic or semi-automatic analysis and visualization are. The sMAP-EM gave much better contrast than the WBP and SIRT in all experimental and simulated studies. This made quantitative analysis of gold particles (Figure S1) and visualization of experimental data reconstructions (Figure 10) more reliable without need for any user-defined parameters for sMAP-EM reconstructed volume.

The idea of sequential regularization is to fit a statistical model to the projection data while regularizing estimates sequentially. The weight of the regularization is kept high initially to strongly suppress any contamination and to get more robust estimates, and it is decreased sequentially to improve resolution of more reliable estimates. We assumed Poisson model for the projection data in the maximum likelihood estimation while penalizing the noise contamination with median filter regularization in this study with sMAP-EM. The results showed that the selected model and the regularization filter are quite suitable for reconstructing the ET data. However, different models and regularizations (e.g. L-filter [23]) can be used for the other tomographic imaging environments and target samples still taking advantage of sequential regularization. Use of *a priori* knowledge about the shape and density of the objects in the sample can further improve the results. Nevertheless, this data is not always available as we did not have it in our case.

The minimum required number of sequences and iterations for each sequence depend on variance of sample and noise level. It is known that high number of iterations generates checkerboard artifacts in the images reconstructed with statistical methods if the images are not regularized during the iterations [31]. However, sMAP-EM can use large number of iterations and keep improving the images since the weight of regularization is never set to zero. Therefore, the number of iterations was safely kept larger than sufficient for the datasets used to have a more general and robust sMAP-EM solution which can be applicable to various samples at different noise levels. The number of sequences and iterations for each sequence can be optimized using an adaptive strategy. Since there is no general image quality criteria to be used for this adaptation, the strategy should be determined according to the requirements of the specific application and the trade-off between the image resolution and the noise level. The high number of iterations increases the computation time. Nonetheless, it can be reduced easily by any computer grid since the 3D sample volume can be reconstructed slice by slice in parallel. We used Techila computer grid in this study to get the results within a feasible time. The demand for high resolution biological images is so high that long computation time can often be acceptable. Therefore, the sMAP-EM method could be a valuable method in cellular biology for further quantitative analysis of the ET reconstructions.

Interpolation [35] and image inpainting [36] methods can be used to recover the missing projection data. These methods use the data available around the edges of the information gap to fill the missing region. The accuracy of the filling highly depends on the size of the gap and the noise level of the projections. In ET, typically $\pm 60^{\circ}$ range is used to acquire projections and it is difficult for these methods to recover such a large gap for this

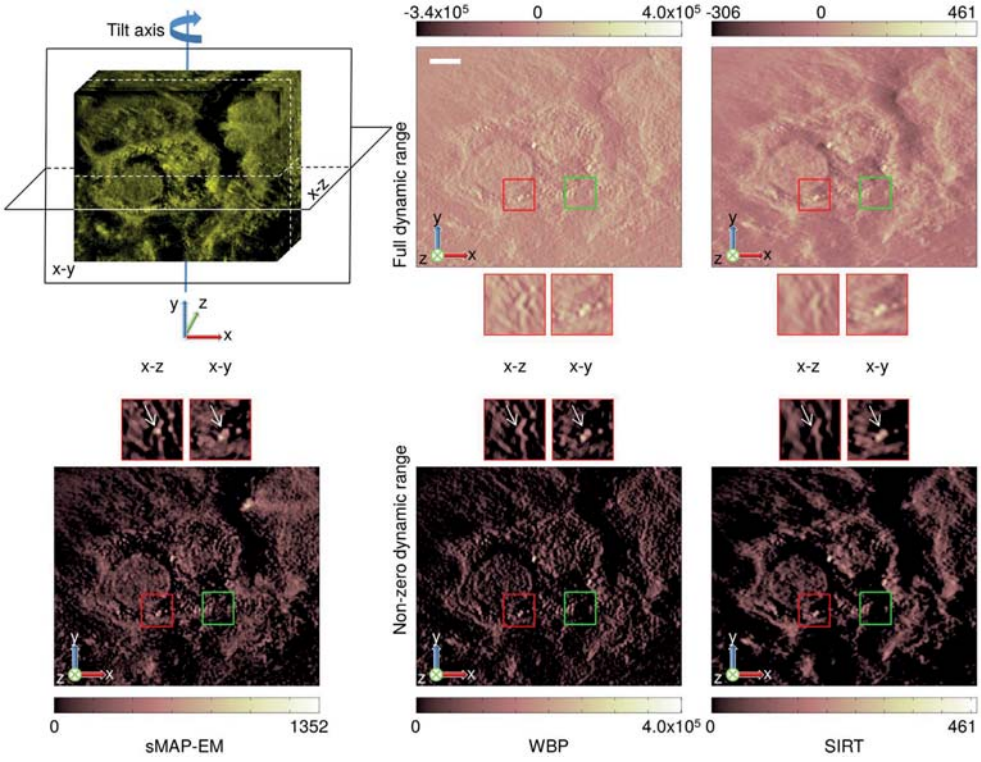

Figure 11. Comparison of orthogonal slices between sMAP-EM, WBP, and SIRT reconstructions from the experimental dataset. (Top) The leftmost figure presents the location of the orthogonal x–y and x–z slices over the reconstructed volume. Full dynamic range of each slice is visualized with a pseudo-color. Two boxes below each image are zoomed-up views of red region of interest (ROI) and its corresponding x-z plane. Green box in all slices indicate location of presumable MVB membrane breakage. (Bottom) Only non-negative pixel values of each slice are rendered with the same pseudo-color, by setting zero to all pixels originally having negative values. Two boxes above each image are zoomed-up views of the same ROI as in the images at the top, and associated x–z plane. sMAP-EM yields identical results for full and non-zero dynamic ranges while WBP and SIRT result in different visual impressions. sMAP-EM is superior to WBP and SIRT to reveal association of gold particles (white arrows). Scale bar 100nm.
doi:10.1371/journal.pone.0108978.g011

range. sMAP-EM fills the gap in a different way by searching for the most likely image, given the whole available projection data. Using the whole available data in the maximum likelihood sense makes sMAP-EM a robust method for filling the missing wedge (Figure 9 and Figure S2). The missing information can also be reduced by using the double axis or the conical tilting geometry. Despite all the complications, if these techniques were used for data acquisition, multi-tilt extension of sMAP-EM would be the reconstruction method to be preferred. It is shown in Figure S3 that the gap filling strength and accuracy of sMAP-EM increase rapidly with the decrease of the missing information. Another observation for this figure is that the high frequencies are not recovered as well as the low frequencies in the missing wedge regions with different sizes. The loss of high frequency content in the missing wedge region decreases the uniformity of the resolution in the spatial domain. However, the other results indicate that even the weak gap filling for the $\pm 60^{\circ}$ tilt angle range is sufficient to produce significant elongation suppression, 3D resolution improvement, and contrast enhancement.

It is difficult to evaluate the accuracy of the experimental data reconstructions since the ground truth is not available. Even though, it is easier to make objective evaluations if some objects with known shape exist in the reconstructed volume. In this study, we had gold particles in the sample used for the experimental data, so we were able to use these particles as reference objects for the quantitative evaluations. For these evaluations, we developed an ellipsoid fitting based method enabling objective, parameter-free, and automatic analysis of the gold particles. In order to have global and statistical information about the reconstruction methods, several gold particles were selected randomly from various parts of the image volume for the evaluation. The method worked well in all sMAP-EM reconstructions. However, the lower contrast in the WBP and the SIRT reconstructions reduced detection accuracy, especially in the cell phantom experiment with the higher noise level (Figure 8, Figure S1).

Deducing the 3D accuracy was possible by comparisons between known radii of the gold particles and three semi-axis lengths of the corresponding fitted ellipsoids in the simulated cell phantom case. Along with our expectations, the results of the

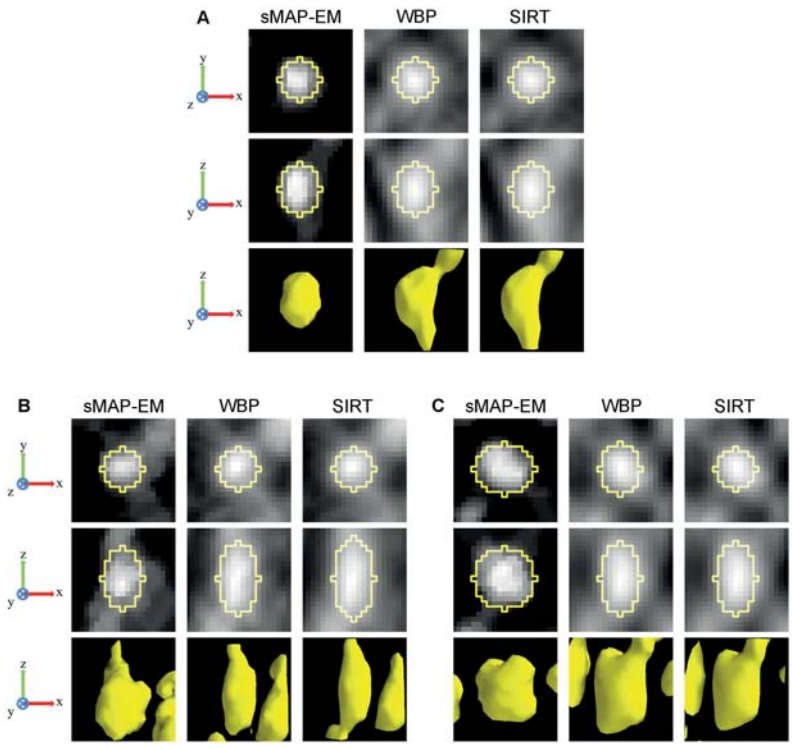

Figure 12. 3D fitted ellipsoids on gold particles in the experimental vesicle data reconstructions. Subfigures A, B, and C present reconstructions for three different gold particles. For each gold particle, orthogonal x–y (top) and x–z (middle) slices through the center are given. Surface renderings (bottom) present overall shape of the reconstructed gold particles. Isosurface threshold value was selected experimentally for the best visualization. All images are in the same scale. The full dynamic range of each subimage was used for the best visualization. The z-direction resolution is better in the sMAP-EM reconstruction than in the WBP and SIRT reconstructions. Also the contrast is superior in the sMAP-EM reconstruction making further analysis simpler. The visual impression is supported by quantitative results presented in Table 2.
doi:10.1371/journal.pone.0108978.g012

quantitative evaluations showed the sMAP-EM reconstruction to be much better than the WBP and SIRT with the test data, adding objective evidences to the visual inspections. The elongation measurements in the cell phantom experiment clearly demonstrated that the sMAP-EM reconstructions were virtually free from this artifact, while both WBP and SIRT reconstructions included the artifacts. The elongation was also consistently reduced in the experimental data reconstruction with the sMAP-EM method.

High contrast and resolution of the sMAP-EM method enables automatic analysis as well as better visual interpretation in ET imaging. For example, the experimental data in Figure 11 shows the localization of target proteins labelled with gold particles. The automation of location detection, counting, distribution calculation, and adjacent distance calculation of the gold particles in this dataset are easier with sMAP-EM.

The present research demonstrated that the proposed sMAP-EM method can successfully compensate for the missing wedge artifacts in ET while improving the contrast and the 3D resolution of the reconstructed structures from both simulated and experimental data. All the quantitative measures supported the qualitative evaluations and showed the sMAP-EM reconstruction to be consistently better than the WBP and SIRT. For accurate ET analysis of the complex cellular structures in biology, we believe that sMAP-EM is the method to be chosen.

Supporting Information

Figure S1 Effects of noise on projections to absolute z-axis length error in the sMAP-EM, WBP and SIRT reconstructions. The plot presents absolute z-axis length error measured from the gold particles in the reconstructions of $\pm 60^{\circ}$ cell phantom projections with different noise levels. Higher noise level decreases the contrast of the reconstructions making the objective ellipsoid fitting less accurate. The noise levels 1 and 2 used in the study are 16.1% and 18.0%, respectively. The other tested noise levels have smaller noise contamination. An ideal reconstruction method independent of the noise in projections would result in straight line with zero slope. It is expected that when the noise level increases, the accuracy of automated analysis method decreases. The absolute z-axis length is slightly increasing with noise on sMAP-EM (red) reconstructions as expected. In the WBP (blue) and SIRT (green) reconstructions, the contrast becomes extremely low with the highest noise contamination that

prevents reliable automatic analysis of the gold particles with the ellipsoid fitting method.
(EPS)

Figure S2 Change in average amplitude ratio of missing per non-missing area relative to wedge size. The graph shows that sMAP-EM fills information in the missing wedge with significantly larger average amplitude than WBP and SIRT. The difference is observed for all wedge sizes including the practical tilting angle ranges of electron tomography (gray-box). The decreasing trend of the ratios in all reconstruction methods is the same as expected; larger the missing area, less filling. However, the long object compensation of Tomo3D SIRT (green) suppresses this decreasing trend as compared to the SIRT without the compensation (cyan).
(TIF)

Figure S3 Spectra of synthetic pattern sMAP-EM reconstructions with 10° increment step of the missing wedge size. To reassure the deterioration trend of the gap filling accuracy relative to the increase of the missing information, sMAP-EM reconstructions with 10, 20, 30, 40, and 50° missing wedge were also conducted. The reconstruction of sMAP-EM with 60° missing wedge is compared to the WBP and SIRT reconstructions in the Figure 9 showing also the ground truth.
(TIF)

Figure S4 The other 3D fitted ellipsoids in the experimental vesicle data reconstructions. Orthogonal x-y (top) and x-z (middle) slices through the center of the gold particles. Surface rendering of the gold particle (bottom) presents overall shape of the reconstructed gold particle. Isosurface threshold value was selected experimentally for the best visualization. All images are in the same scale. The full dynamic range of each subimage was used for the best visualization. The quantitative results are presented in Table 2.
(TIF)

Author Contributions

Conceived and designed the experiments: LP EA UT SP TM PS VM RHC UR. Performed the experiments: LP EA TM PS. Analyzed the data: LP EA TM RHC. Contributed reagents/materials/analysis tools: LP PS RHC. Wrote the paper: LP EA SP TM UR RHC. Developed the reconstruction method and toolbox: UT EA UR.

References

1. McEwen BF, Marko M (2001) The emergence of electron tomography as an important tool for investigating cellular ultrastructure. Journal of Histochemistry & Cytochemistry 49: 553–563.
2. Lučić V, Förster F, Baumeister W (2005) Structural studies by electron tomography: From cells to molecules. Annual Review of Biochemistry 74: 833–865.
3. Midgley P, Weyland M (2003) 3D electron microscopy in the physical sciences: the development of Z-contrast and EFTEM tomography. Ultramicroscopy 96: 413–431.
4. Koster AJ, Grimm R, Typke D, Hegerl R, Stoschek A, et al. (1997) Perspectives of molecular and cellular electron tomography. Journal of Structural Biology 120: 276–308.
5. Penczek P, Marko M, Buttle K, Frank J (1995) Double-tilt electron tomography. Ultramicroscopy 482: 393–410.
6. Mastronarde DN (1997) Dual-axis tomography: an approach with alignment methods that preserve resolution. Journal of Structural Biology 120: 343–352.
7. Lanzavecchia S, Cantele F, Bellon PL, Zampighi L, Kreman M, et al. (2005) Conical tomography of freeze-fracture replicas: a method for the study of integral membrane proteins inserted in phospholipid bilayers. Journal of Structural Biology 149: 87–98.
8. Radermacher M (2006) Weighted back-projection methods. In: Frank J, editor, Electron Tomography: Methods for Three-Dimensional Visualization of Structures in the Cell, New York: Springer. 2nd edition, pp. 245–273.
9. Orlov IM, Morgan DG, Cheng RH (2006) Efficient implementation of a filtered back-projection algorithm using a voxel-by-voxel approach. Journal of Structural Biology 154: 287–296.
10. Agulleiro JI, Fernandez JJ (2012) Evaluation of a multicore-optimized implementation for tomographic reconstruction. PLOS ONE 7: e48261.
11. Delaney A, Bresler Y (1998) Globally convergent edge-preserving regularized reconstruction: an application to limited-angle tomography. IEEE Transactions on Image Processing 7: 204–221.
12. Penczek PA (2010) Fundamentals of three-dimensional reconstruction from projections. Methods in Enzymology 482: 1–33.
13. Wolf D, Lubk A, Lichte H (2014) Weighted simultaneous iterative reconstruction technique for single-axis tomography. Ultramicroscopy 136: 15–25.
14. Maiorca M, Hanssen E, Kazmierczak E, Maco B, Kudryashev M, et al. (2012) Improving the quality of electron tomography image volumes using pre-reconstruction filtering. Journal of Structural Biology 180: 132–142.
15. Aganj I, Bartesaghi A, Borgnia M, Liao HY, Sapiro G, et al. (2007) Regularization for inverting the radon transform with wedge consideration. In: 4th IEEE International Symposium on Biomedical Imaging: From Nano to Macro. pp. 217–220.
16. Gopinath A, Xu G, Ress D, Oktem O, Subramaniam S, et al. (2012) Shape-based regularization of electron tomographic reconstruction. IEEE Transactions on Medical Imaging 31: 2241–2252.
17. Zürner A, Döblinger M, Cauda V, Wei R, Bein T (2012) Discrete tomography of demanding samples based on a modified SIRT algorithm. Ultramicroscopy 115: 41–49.
18. Goris B, Van den Broek W, Batenburg K, Heidari Mezerji H, Bals S (2012) Electron tomography based on a total variation minimization reconstruction technique. Ultramicroscopy 113: 120–130.
19. Leary R, Saghi Z, Midgley PA, Holland DJ (2013) Compressed sensing electron tomography. Ultramicroscopy 131: 70–91.
20. Tuna U, Sohlberg A, Ruotsalainen U (2013) Can we reduce SPECT acquisition time using MAP-EM reconstruction. Journal of Pattern Recognition and Intelligent Systems 1: 54–63.
21. Fessler JA, Hero AO (1995) Penalized maximum-likelihood image reconstruction using space-alternating generalized EM algorithms. IEEE Transactions on Image Processing 4: 1417–1429.
22. Hebert T, Leahy R (1989) A generalized EM algorithm for 3-D Bayesian reconstruction from Poisson data using Gibbs priors. IEEE Transactions on Medical Imaging 8: 194–202.
23. Alenius S, Ruotsalainen U (2002) Generalization of median root prior reconstruction. IEEE Transactions on Medical Imaging 21: 1413–1420.
24. Soonsawad P, Xing L, Milla E, Espinoza JM, Kawano M, et al. (2010) Structural evidence of glycoprotein assembly in cellular membrane compartments prior to Alphavirus budding. Journal of Virology 84: 11145–11151.
25. Shepp LA, Vardi Y (1982) Maximum likelihood reconstruction for emission tomography. IEEE Transactions on Medical Imaging 1: 113–122.
26. Herman GT, Odhner D (1991) Performance evaluation of an iterative image reconstruction algorithm for positron emission tomography. IEEE Transactions on Medical Imaging 10: 336–346.
27. Hanson KM, Wecksung GW (1983) Bayesian approach to limited-angle reconstruction in computed tomography. Journal of the Optical Society of America 73: 1501–1509.
28. Herman GT, Hurwitz H, Lent A, Lung HP (1979) On the bayesian approach to image reconstruction. Information and Control 42: 60–71.
29. Hurwitz Jr H (1975) Entropy reduction in Bayesian analysis of measurements. Physical Review A 12: 698.
30. Levitan E, Herman GT (1987) A maximum a posteriori probability expectation maximization algorithm for image reconstruction in emission tomography. IEEE Transactions on Medical Imaging 6: 185–192.
31. You J, Wang J, Liang Z (2007) Range condition and ML-EM checkerboard artifacts. IEEE Transactions on Nuclear Science 54: 1696–1702.
32. Agulleiro JI, Fernandez JJ (2011) Fast tomographic reconstruction on multicore computers. Bioinformatics 27: 582–583.
33. Xu W, Xu F, Jones M, Keszthelyi B, Sedat J, et al. (2010) High-performance iterative electron tomography reconstruction with long-object compensation using graphics processing units (GPUs). Journal of Structural Biology 171: 142–153.
34. Kankaanpää P, Paavolainen L, Tiitta S, Karjalainen M, Päivärinne J, et al. (2012) BioImageXD: an open, general-purpose and high-throughput image-processing platform. Nature Methods 9: 683–689.
35. van Velden F, Kloet R, Van Berckel BNM, Molthoff CFM, Lammertsma A, et al. (2008) Gap filling strategies for 3-D-FBP reconstructions of high-resolution research tomograph scans. IEEE Transactions on Medical Imaging 27: 934–942.
36. Bertalmio M, Sapiro G, Caselles V, Ballester C (2000) Image inpainting. In: Proceedings of the 27th Annual Conference on Computer Graphics and Interactive Techniques. SIGGRAPH '00, pp. 417–424. doi:10.1145/344779.344972.

Publication II

T. Moriya, E. Acar, R. H. Cheng, and U. Ruotsalainen, “A Bayesian approach for suppression of limited angular sampling artifacts in single particle 3D reconstruction”, Journal of Structural Biology, vol. 191, no. 3, pp. 318–31, June 2015.

Journal of Structural Biology 191 (2015) 318–331

Contents lists available at ScienceDirect

Journal of Structural Biology

journal homepage: www.elsevier.com/locate/yjsbi

A Bayesian approach for suppression of limited angular sampling artifacts in single particle 3D reconstruction

Toshio Moriya [a,b,*], Erman Acar [a,b], R. Holland Cheng [c], Ulla Ruotsalainen [a,b]

[a] Department of Signal Processing, Tampere University of Technology, P.O. Box 553, FI-33101 Tampere, Finland
[b] BioMediTech, Tampere University of Technology, P.O. Box 553, FI-33101 Tampere, Finland
[c] Department of Molecular and Cellular Biology, University of California, Briggs7 (MailCode#0390), Davis, CA 95616, USA

ARTICLE INFO

Article history:
Received 3 April 2015
Received in revised form 10 July 2015
Accepted 16 July 2015
Available online 17 July 2015

Keywords:
Cryo-electron microscopy
Sparse angular sampling
Missing cone
Maximum *a posteriori* probability estimation
Median root prior reconstruction
Poisson image formation model

ABSTRACT

In the single particle reconstruction, the initial 3D structure often suffers from the limited angular sampling artifact. Selecting 2D class averages of particle images generally improves the accuracy and efficiency of the reference-free 3D angle estimation, but causes an insufficient angular sampling to fill the information of the target object in the 3D frequency space. Similarly, the initial 3D structure by the random-conical tilt reconstruction has the well-known "missing cone" artifact. Here, we attempted to solve the limited angular sampling problem by sequentially applying maximum *a posteriori* estimate with expectation maximization algorithm (sMAP-EM). Using both simulated and experimental cryo-electron microscope images, the sMAP-EM was compared to the direct Fourier method on the basis of reconstruction error and resolution. To establish selection criteria of the final regularization weight for the sMAP-EM, the effects of noise level and sampling sparseness on the reconstructions were examined with evenly distributed sampling simulations. The frequency information filled in the missing cone of the conical tilt sampling simulations was assessed by developing new quantitative measurements. All the results of visual and numerical evaluations showed the sMAP-EM performed better than the direct Fourier method, regardless of the sampling method, noise level, and sampling sparseness. Furthermore, the frequency domain analysis demonstrated that the sMAP-EM can fill the meaningful information in the unmeasured angular space without detailed *a priori* knowledge of the objects. The current research demonstrated that the sMAP-EM has a high potential to facilitate the determination of 3D protein structures at near atomic-resolution.

1. Introduction

3D structures of proteins at a near-atomic resolution provide valuable information for the understanding of physiological functions, and for the development of medicines. Single particle reconstruction (SPR) is a suitable method for the structural studies of proteins when their crystals are difficult to obtain with sufficient quality for crystallography (Frank, 2006). In general, the SPR assumes free orientations of the protein particles upon the imaging by cryo-electron microscopy (cryo-EM). This flexibility creates the necessity to estimate 3D orientations of the protein particles on the grids solely from their extremely noisy projected 2D images. For this, the traditional SPR process includes "*ab initio* 3D reconstruction" step where the initial estimate of the particle structure is computed using a reference-free 3D angle estimation and a 3D reconstruction method.

The reference-free 3D angle estimation is commonly done using the averaged particle views (Frank, 2006). These averages are calculated beforehand in the "reference-free 2D averaging" step, where particle images are aligned, classified, and averaged to improve signal-to-noise ratio of each 2D particle view. To improve the accuracy of the 3D angle estimation, it is a common practice to

Abbreviations: CTF, phase-contrast transfer function; DF, direct Fourier; EM algorithm, expectation maximization algorithm; FSC, Fourier shell correlation; FSMAR, Fourier shell mean amplitude ratio; FSMSE, Fourier shell mean squared error; MAP, maximum *a posteriori* probability; MAP-EM, maximum *a posteriori* probability expectation maximization; ML, maximum likelihood; ML-EM, maximum likelihood expectation maximization; MRP, median root prior; MSE, mean squared error; MSD2D, mean squared difference in the 2D spatial domain; MSE3D, mean squared error in the 3D spatial domain; OSL, one-step-late; SNR, signal to noise ratio; sMAP-EM, sequential maximum *a posteriori* probability expectation maximization.

* Corresponding author at: Department of Structural Biochemistry, Max-Planck-Institute of Molecular Physiology, Otto-Hahn-Str. 11, 44227 Dortmund, Germany.

E-mail addresses: toshio.moriya@mpi-dortmund.mpg.de (T. Moriya), erman.acar@tut.fi (E. Acar), rhch@ucdavis.edu (R.H. Cheng), ulla.ruotsalainen@tut.fi (U. Ruotsalainen).

http://dx.doi.org/10.1016/j.jsb.2015.07.007
1047-8477/

select a small number of the 2D class averages with the highest qualities (less than 100 classes). However, this class selection causes an insufficient number of angular sampling to fill the information in the 3D frequency space of the interest. Missing gaps in this sparse sampling correspond to the projection angles of the excluded 2D classes. An alternative approach of 3D angle estimation uses physical tilting of the specimen upon imaging with electron microscope. The known angle of the tilt constraint provides the relative angels between the tilt pairs of 2D projection views. This additional information simplifies the computational determination of the 3D angles. For proteins, the most widely-used method of this approach is the random-conical tilt reconstructions (Radermacher et al., 1986). However, this reconstruction method has the well-known drawback of the "missing cone" since the maximum tilting angle is limited to approximately ±60° with conventional electron microscope. Therefore, the initial estimation of structure is highly possible to be contaminated with a significant amount of artifacts. The artifacts can cause errors through the reference bias in the 3D refinement, known as "Einstein from noise" (Henderson, 2013; van Heel, 2013). It is important to suppress the effects of the sparse sampling gaps or missing cone on the quality of the initial 3D reconstruction.

In the SPR field, the artifact contaminations in 3D reconstruction with limited angular sampling have been well known (Penczek, 2010a) but no well-established solutions have been proposed. Currently, many varieties of back-projection and algebraic 3D reconstruction methods are available through the freely-distributed SPR software packages (Hohn et al., 2007; Scheres, 2012a; Scheres et al., 2008; Shaikh et al., 2008; Tang et al., 2007; Van Heel et al., 2011). These methods are simple and efficient. The packages also support methods that iteratively refine 3D volume by minimizing errors between the measured and estimated projections to minimize noise-induced inconsistency. The same approaches have been well studied for 2D image reconstruction from measured 2D projections with the missing information in the field of tomography (e.g. emission, transmission, and electron tomography). These studies have shown that back-projection methods are sensitive to the missing information and can result in severe artifacts (Delaney and Bresler, 1998) and that algebraic methods also do not fill the information gaps (Penczek, 2010a).

In contrast, there are tomography studies showing that some statistical reconstruction methods are capable of suppressing the artifacts yielded from the missing information, even when detailed *a priori* knowledge of the objects is not available (Paavolainen et al., 2014; Tuna et al., 2013). These studies used the maximum *a posteriori* probability estimates with expectation maximization algorithms (MAP-EM). An inspiring study is the application in electron tomography of biological samples, where the authors applied the sequential MAP-EM (sMAP-EM) method to compensate for missing wedges of 2D image reconstructions (Paavolainen et al., 2014). This sequential method was originally developed for the suppression of the artifacts yielded from the missing angles in positron emission tomography and single-photon emission computed tomography (Tuna et al., 2013). It was consistently superior to a weighted back-projection and a simultaneous iterative reconstruction technique. The sMAP-EM showed robustness against noise, and suppressed artifacts by filling meaningful information in the missing wedge (Paavolainen et al., 2014). The MAP-EM based approaches have been used also in the 3D refinement and 3D classification of SPR (Kucukelbir et al., 2012; Lyumkis et al., 2013; Scheres, 2012a, 2012b). The recent growth of statistical reconstruction methods is prominent in the SPR field (Scheres, 2010; Sigworth et al., 2010), and lead to "the resolution revolution" as described in a recent review (Kühlbrandt, 2014). All the three near-atomic resolution SPR structures referred in this review used the statistical reconstruction approach implemented in RELION (Scheres, 2012a). It is possible now to achieve the 3 Å-level resolution even for small membrane protein with low symmetry, such as TRPV1 ion channel (300 kDa and C4 symmetry) (Liao et al., 2013). However, the objectives of these statistical 3D reconstruction methods have not been in the compensation for limited angular sampling. It is because a reasonably dense sampling can be usually assumed at the 3D classification and 3D refinement stages if the number of the observed particle images is sufficient (conventionally at least 5000 images) and the target protein does not have strong "preferred orientations". However, it is frequently not reasonable to assume the same for the initial 3D reconstruction right after the reference-free 3D angle estimation.

The current research aims to develop a statistical 3D reconstruction method which performs well even with sparse angular sampling or conical tilt sampling used in the *ab initio* 3D reconstruction step of SPR. Since it is not necessary to estimate the 3D projection angles simultaneously in the initial 3D reconstruction, the task for the 3D reconstruction is much simpler than the ones for the previous MAP-EM based algorithms in SPR. This allowed us to focus on the issue of the limited angular sampling cases. Here, we propose to expand the concepts of the sMAP-EM to the 3D domain and develop the implementation for SPR. The evenly distributed and the conical tilt angular samplings of simulated datasets were examined with various noise levels. The three different levels of sparseness were also examined with the evenly distributed angles. To understand the characteristic and behavior of the sMAP-EM reconstruction process, the Fourier shell correlation (FSC) (van Heel and Schatz, 2005) and the mean squared error (MSE) against the ground truth were used as the numerical measurements. Following the convention of the SPR field, the 3D resolutions were evaluated using the FSC between two independent reconstructions, along with the visual inspection. To numerically assess the gap filling ability of sMAP-EM in the frequency domain, the Fourier shell mean amplitude ratio (FSMAR) and Fourier shell MSE (FSMSE) were developed in this study. Finally, the sMAP-EM reconstruction from the experimental cryo-EM particle images was conducted. We expect that the sMAP-EM would be able to suppress the artifacts in the *ab initio* 3D reconstruction of SPR with limited angular sampling by estimating meaningful values for the information missing gaps.

2. Theoretical background

2.1. Bayesian inference

The Bayesian inference can be expressed as:

$$P(\Theta|X) \propto P(X|\Theta)P(\Theta),$$

where $P(\Theta|X)$ is *a posterior* probability density function of a parameter set Θ when a set of particle images X has been observed, $P(X|\Theta)$ is the likelihood function of X when Θ is known already, and $P(\Theta)$ is the *a priori* probability density function of Θ. The most important parameter in Θ is a voxel value set of a 3D volume for the 3D reconstruction in the SPR, since this is the objective. After we observe a set of particle images, the best estimate of 3D structure is the particular one having the maximum *a posterior* probability among all the other possible reconstructions in a given 3D space. This probability is not directly accessible but it is same as the right-hand terms which can be calculated using an estimate of Θ including 3D volume. This estimate can be refined using an iterative procedure. The expectation maximization (EM) algorithm (Dempster et al., 1977) is a popular choice to compute the maximum *a posteriori* probability (MAP) estimation using this approach, and so called MAP-EM.

To enhance the computational efficiency, we can further assume that all possible 3D structures happen with equal chance. In this case, *a priori* probability $P(\Theta)$ is constant and the formula can be reduced to:

$$P(\Theta|X) \propto P(X|\Theta)$$

Therefore, the maximization of *a posterior* probability $P(\Theta|X)$ becomes same as maximizing likelihood $P(X|\Theta)$, and the maximum likelihood estimation (ML estimation) calculated by EM algorithm is ML-EM. Historically, the theoretical works of the statistical reconstruction methods started with ML-EM due to its simplicity and the limitation of computation power. These studies have shown that ML-EM produces statistically unbiased but noisy images (Herman and Odhner, 1991). For the attempt to improve the image quality, MAP-EM has become more popular choice (Hanson and Wecksung, 1983; Herman et al., 1979; Levitan and Herman, 1987) as the computer technology improved. *A priori* knowledge can be introduced to the MAP-EM by the one-step-late (OSL) technique (Green, 1990).

2.2. Statistical model of image formation

Assuming Poisson distribution for the statistical model of image formation, the following model is used for the cryo-EM application incorporating the phase-contrast transfer function (CTF):

$$s_d = CTF_d\, v_d \approx CTF_d \sum\nolimits_b v_b a_{db} \quad v_b \sim Poisson(\lambda_b)$$

where v_b is the electron counts reflecting the specimen density at the bth 3D position (Fig. 1). It is a random discrete variable following a Poisson distribution with parameter $\lambda_b > 0$, which is the mean electron counts of v_b considered as the true density value. The a_{db} is a weight of a system matrix defining the contribution of the v_b to form the dth pixel intensity v_d in a stack of all CTF-free projection images. The term $\sum_b v_b a_{db}$ expresses the integral operation of 3D forward-projection along a line orthogonal to the dth pixel. The CTF_d denotes a filtering operator expressing the CTF influence at the dth pixel. Finally, the s_d is the dth pixel intensity in a stack of all observed projection images. For this application, we assumed that all projection images are CTF-corrected by applying a pseudo-inverse operation CTF_d^{-1} at the dth pixel:

$$CTF_d^{-1} s_d \approx v_d \approx \sum\nolimits_b v_b a_{db} \tag{1}$$

It is important to note that the CTF function is not invertible because of the zero crossing. Here, we assume CTF_d^{-1} represents a pseudo-inverse operation, such as phase-flipping operation. Therefore, the left term becomes an approximation of right term, indicated by $\approx$. Using this Poisson distribution based image formation model, the probability density function of observed voxel values in the 3D volume $\boldsymbol{V}$ conditioned on the mean values $\boldsymbol{\lambda}$ can be expressed as:

$$f(\boldsymbol{V}|\lambda) \approx f(\boldsymbol{VA}|\lambda \boldsymbol{A}) = \prod_{db} \exp(-\lambda_b a_{db}) \frac{(\lambda_b a_{db})^{v_b a_{db}}}{(v_b a_{db})!} \tag{2}$$

Here, the random variable $\boldsymbol{V}$ is not directly measurable but indirectly accessible through the relation of $\boldsymbol{VA}$ with the observed projection images $\boldsymbol{CTF}^{-1}\boldsymbol{S} \approx \boldsymbol{V}$, defined by the Eq. (1). Accordingly, the expected value of $v_b a_{db}$ conditioned on its sum $CTF_d^{-1} s_d$ and an estimated mean value $\lambda_b^{\langle k \rangle} a_{db}$ at a kth iteration can be calculated with:

$$\begin{aligned} E[v_b a_{db} | CTF_d^{-1} s_d, \lambda_b^{\langle k \rangle} a_{db}] &= CTF_d^{-1} s_d \frac{\lambda_b^{\langle k \rangle} a_{db}}{\sum_{b'} \lambda_{b'}^{\langle k \rangle} a_{db'}} \\ &= \left(\frac{CTF_d^{-1} s_d}{\lambda_d^{\langle k \rangle}} a_{db} \right) \lambda_b^{\langle k \rangle} \triangleq \overline{v_b a_{db}}^{\langle k \rangle}, \end{aligned} \tag{3}$$

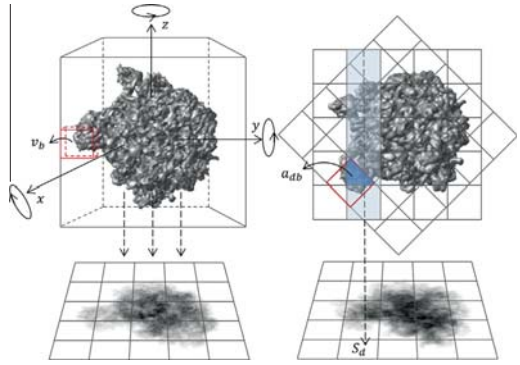

Fig. 1. Coordinate system and image formation model of the cryo-electron microscopy (cryo-EM). Left: the coordinate system and the original orientation of the target protein. The 3D angle was defined by the *zyz* convention of Euler angle with counter clockwise rotation. Right: the cryo-EM image formation model. The dashed arrow represents an electron beam radiating from the top and transmitting though the sample. The s_d is a pixel value of an observed projection image in 2D, v_b is a voxel value in the 3D density map, and a_{db} defines the contribution of v_b to form s_d disregarding the phase-contrast transfer function (CTF).

where the $\sum_{b'} \lambda_{b'}^{\langle k \rangle} a_{db'} = \lambda_d^{\langle k \rangle}$ expresses a 3D forward-projection of an estimated density map for the dth pixel at a kth iteration. Using this Eq. (3) to replace $v_b a_{db}$ with $\frac{\lambda_b^{\langle k \rangle} a_{db}}{\lambda_d^{\langle k \rangle}}$, the ML-EM algorithm for this statistical model can be derived by solving the derivative of a logarithm form of the Formula (2) at zero (Green, 1990).

2.3. Updating function of the MAP-EM with median filter

Smoothing prior is a common choice for the regularization or penalization of the noise with OSL. This Bayesian prior is based on heuristics and assumes most of objects in the real world are locally smooth, and the signal intensities reflecting objects are frequently similar in the small neighborhood. The median root prior (MRP) reconstruction method uses median filtering to implement smoothing prior with OSL technique (Alenius and Ruotsalainen, 2002). The useful property of median filter is that it preserves edges of objects while reducing the noise in measured data. Using the above settings and the assumption of $\sum_d a_{db} = 1$, the update function of the MRP reconstruction method is defined as follows:

$$\lambda_b^{\langle k+1 \rangle} = C_b^{P\langle k \rangle} C_b^{L\langle k \rangle} \lambda_b^{\langle k \rangle},$$

where

$$C_b^{P\langle k \rangle} = \frac{1}{1 + \beta \left(\frac{\lambda_b^{\langle k \rangle} - Med(\lambda_b^{\langle k \rangle}; N_b)}{Med(\lambda_b^{\langle k \rangle}; N_b)} \right)}$$

is the penalty coefficient, and

$$C_b^{L\langle k \rangle} = \sum\nolimits_d \frac{CTF_d^{-1} s_d}{\lambda_d^{\langle k \rangle}} a_{db} \tag{4}$$

is the likelihood coefficient. $Med(\lambda_b^{\langle k \rangle}; N_b)$ is the median value in a $N_b \times N_b \times N_b$ neighborhood of the bth voxel. As we can see from the similarity between Eqs. (3) and (4), the likelihood coefficient is the same for the ML and MAP estimates in the OSL. When $\beta = 0$, the penalty coefficient $C_b^{Pk} = 1$ has no effect on the updating and the algorithm calculates ML estimate. The number of iterations and regularization weight β is given by user as input parameters. The details of the derivation can be found in the previous works

of the MRP method (Alenius and Ruotsalainen, 2002; Alenius, 1999).

2.4. Sequential application of the MRP reconstruction: sMAP-EM

The previous study has shown that the three parameters of the MRP reconstruction method strongly affect the final resolution, the final contrast, and the visual impression of resulting reconstructions: (1) the number of iterations, (2) the window size of the median filter, and (3) the regularization weight (β) (Alenius and Ruotsalainen, 2002). The number of iterations must be sufficiently large to achieve a high quality of the final result, like the other statistical methods. The window size of the median filter must be adjusted to preserve the structural features of the research interests. The regularization weight must be selected properly depending on the application purpose; in general, the smaller β results in higher resolution and contrast, with the cost of more noisy impression. To achieve higher image quality by expanding the MRP method, the sequential method "sMAP-EM" was developed (Tuna et al., 2013). The method consists of the two levels of nested iteration processes. The inner loop is the original MRP reconstruction using a constant β value through the whole iterations. The outer loop uses the resulting image of the previous cycle and gradually reduces the regularization weight for the inner loops. In this paper, we refer each cycle of the inner loop as simply "iteration" and the one of the outer loop as "regularization weight stage" or simply "stage". The number of stages as well as the number of iterations and the β value for each stage are the user-defined input parameters. These three parameters together define the final regularization weight and the total number of iterations for the sMAP-EM, which strongly affect the quality of the resulting reconstruction. A small β value other than 0.0 is recommend for the final stage, since the absence of the regularization can yield a severe checkerboard artifacts with a large number of iterations when the measured projection data is noisy (You et al., 2007). The initial estimate of reconstruction is another user-defined input parameter, for which an image of uniform positive intensities is commonly used. By using the sequential reconstructions, the sMAP-EM successfully enhances the final quality of the reconstructed image in terms of the resolution and the contrast by gradually weakening the regularization and initializing stages with the result of previous stage.

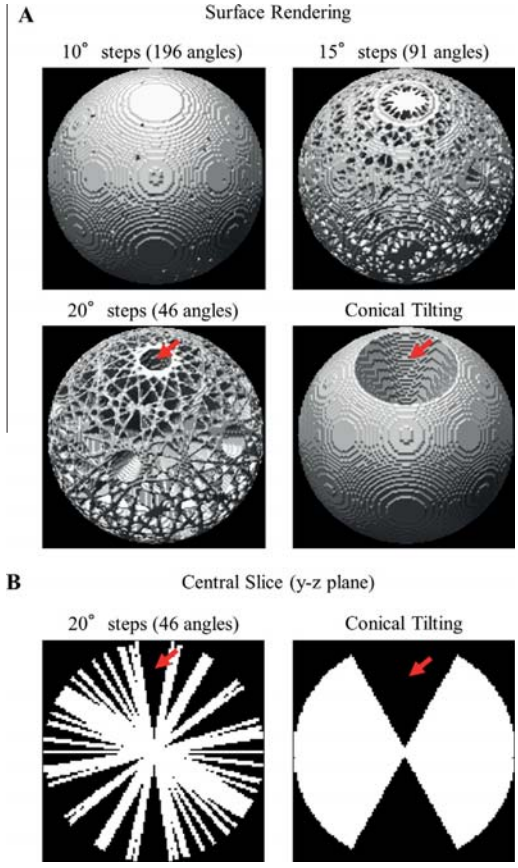

Fig. 2. Sampling gaps and missing cone of 3D angular samplings. (A) 3D visualization of evenly-distributed and conical tilting angular sampling in the frequency domain. (B) Representative central slices at the y–z plane showing the missing gaps and cones. The red arrows indicate the corresponding area of a large gap and missing cone between (A) and (B).

3. Material and methods

3.1. Datasets

3.1.1. Simulated dataset of evenly distributed angular sampling

A 3D phantom model was generated from an atomic coordinate data of the 50S ribosomal subunit obtained from the Protein Data Bank (PDB code: 1JJ2) using UCFS chimera (Pettersen et al., 2004). The simulated model was a $112 \times 112 \times 112$ voxel array with isotropic voxel size of 3.26 Å/voxel. The background offset of the particle density map was adjusted to ensure that there were no pixels with negative values in its 3D projection images after adding noise. Simulated equally-distributed projections from this density map were obtained with 20°, 15°, and 10° angular samplings (46, 91, and 196 angles) using XMIPP 3.1 (Scheres et al., 2008). The information gaps of the angular sampling in the frequency domain are shown in Fig. 2. There are no obvious missing gaps with 10° angular sampling, the 15° starts showing clear gap space, and the 20° has additionally large gaps (red arrow). The phase-contrast transfer function (CTF) was not imposed since we assumed that the input particle images were CTF-corrected. Two types of noise in cryo-EM projections were simulated: (1) Poisson noise associated with electron counting and (2) zero-mean Gaussian white noise associated with the detector system. The noise levels were set to the SNR (variance ratio) of 10.0, 5.0, 1.0, and 0.5 (Supporting Fig. 1). Only single projection image was used at each Euler angle to directly examine the effect of the noise level.

3.1.2. Simulated dataset of conical tilt sampling

The above simulated density map of the 50S ribosomal subunit was also used to generate 180 projections of a conical tilt sampling with 60° tilt with 2° angle steps (Fig. 2). The same set of noise levels as above was used. The CTF was not simulated, and each Euler angle contained only single projection image.

3.1.3. Experimental dataset

The previously published cryo-EM dataset of the 50S ribosomal subunit (Voss et al., 2010) was used as experiment dataset and is available online. The images were CTF-corrected with the pseudo-inverse CTF operation and their dimensions are 100×100 pixels with isotropic pixel size of 3.26 Å/voxel. The two subsets of 16,512 images were randomly selected from the original set of 82,575 images. The 2D translations and 3D

projection angles of the selected particle images were independently estimated for each subset by a reference-based method using RELION 1.2 (Scheres, 2012a). The reconstruction result in the cryo-EM dataset was used as the starting model. The low-pass filter with the 70 Å cutoff was applied to the starting model before the process. Using the estimated 3D angles, the images were classified into 196 equally-distributed projections and the average image of each class was calculated. Before the averaging, the background offset of the particle images was adjusted to ensure that there were no negative value pixels. The selection of high quality 2D classes in the *ab initio* 3D reconstruction step was simulated. The number of particle images in each class was used as the selection criterion, because a larger number of particle images is usually associated with a higher quality (a better 2D resolution and a lower noise level). The class averages of 46, 91, and 196 projection angles (corresponding to 20°, 15°, and 10° angular samplings) were chosen to express three different levels of the angular sampling sparseness.

3.2. Reconstruction method

The development of 3D sMAP-EM is based on the publically available implementation of its 2D version used in the previous study (Paavolainen et al., 2014). The major difference in the implementation is the required number of parameters to express the projection angle of each measured dataset. The 2D image reconstruction assumes the tomographic measurement with the single-axis tilting geometry, and uses only one angle since the rotation is constrained around a tilt axis. On the other hand, the 3D volume reconstruction requires two parameters in Euler angle definition (excluding the in-plane rotation from the three parameters) to express the free rotation of the target object. Accordingly, all implementations of the 2D operations were converted to the 3D operations including the median filter, the forward projection, and backward projection. The matrix of $3 \times 3 \times 3$ voxels was used for the regularization median filter. This is the smallest possible 3D matrix to ensure that the structural features are reconstructed as detailed as possible for determining the 3D protein structures with a near-atomic resolution. In each 3D forward-projection of the estimated volume, the density values of the voxels outside of the sphere-shaped reconstruction space were set to the average density value of user-defined background space. This process expresses the density of surrounding vitreous ice in the estimated 2D projections. Judging from the measurement histories of preliminary reconstructions, we selected 30 iterations for the single stage setting (non-sequential reconstruction equivalent to the original MRP method). This setting was used in the selection of a proper regularization weight of the sMAP-EM for a given experimental condition. For the evaluation of the sMAP-EM reconstruction, 91 iterations per stage was used with multiple stage setting (sequential reconstruction). We set the number of iterations to be large enough to achieve sufficient quality in all the reconstructions. The MATLAB programming environment with the parallel processing tool box (MathWorks Inc., MA, USA) was used to enhance the computation speed by parallelizing the process of each projection angle. As an example of the computation time, the process of 30 iterations took approximately 10 min on average for a $112 \times 112 \times 112$ voxel reconstruction from 46 projection images, using the 12 cores of Intel X5660 processor with 48 GB memory or the 12 cores of AMD Opteron 2435 processor with 32 GB memory. The source code of the 3D version is publically available online[1].

[1] http://www.cs.tut.fi/sgn/m2obsi/m2obsiWWW/demos/TUT_sMAPEM3D_archive_20141127/3DsMAPEM.html.

3.3. Evaluation methods

The quality of each reconstruction result was evaluated by ground truth based and ground truth free methods. For the ground truth based evaluations, the mean squared error in the 3D spatial domain and the FSC (van Heel and Schatz, 2005) relative to the ground truth (the ground truth FSC) were measured. The FSC between two independent reconstructions (the gold standard FSC) was used as the ground truth free measurement of the 3D resolution. Accordingly, for each experimental condition, two 3D density maps were independently reconstructed from different noise realizations. A soft-edged mask with Gaussian-falloff was applied to all the reconstructions before the calculation of both FSC types, so that the voxel values around the edge were smoothly changed from foreground value to the average background value. The mean squared difference between estimated and observed projections in the 2D spatial domain (MSD2D) was used as an additional ground truth free method.

For the assessment of the information filling in unmeasured angular space, we devised the Fourier shell mean amplitude ratio (FSMAR) and Fourier shell MSE (FSMSE). The FSMAR measures the mean amplitude of the information filled in the unmeasured space relative to the one in the measured space at each frequency channel:

$$FSMAR(r) = \left(\frac{\sum_{r_i \in r \bigcup au} |F(r_i)|^2}{\sum_{r_j \in r \bigcup am} |F(r_j)|^2} \right) / \left(\frac{\sum_{r_i \in r \bigcup au} |F_{true}(r_i)|^2}{\sum_{r_j \in r \bigcup am} |F_{true}(r_j)|^2} \right),$$

where F is the complex form of Fourier transform of the reconstructed volume, F_{true} is for the ground truth volume, r_i is an individual voxel component in the unmeasured angular space (au) of a shell with radius r in the frequency space, and r_j is a voxel value in the measured space (am) of the shell. Similarly, the FSMSE is the MSE of the gap-filling in the unmeasured angular space at each frequency band:

$$FSMSE(r) = \frac{1}{N_{au}} \sum_{r_i \in r \bigcup au} (F_{true}(r_i) - F(r_i))^2,$$

where N_{au} is the number of voxels in the unmeasured angular space of a shell with radius r in the frequency space. Since the FSMAR and FSMSE require the ground truth, they were used only in the simulation study.

To assess the performance level of sMAP-EM, the direct Fourier (DF) 3D reconstruction method implemented in XMIPP 3.1 (Scheres et al., 2008) was used as a comparison. We kept the recommended default settings for the algorithm parameters. The background offsets of the input projection images were adjusted to zero for the reconstructions by this method.

4. Results

4.1. Experiment A1: selection of the regularization weights for sMAP-EM

The regularization weight of the termination stage strongly affects the final quality of the sMAP-EM reconstruction process. Therefore, it is desirable to be able to find the proper β value of the termination stage for a given research purpose without having the ground truth, because the true structure is usually unknown in real application of the SPR. For this, the simulated datasets of evenly distributed angular sampling were reconstructed with the single stage setting for the β values of 1.0, 0.75, 0.5, 0.25, 0.1 and 0.0. The reconstructions were evaluated with the ground truth based methods (MSE3D and the FSC with ground truth), and their

Table 1
Optimal β values in the experiment A1 and A2.

	10.0 SNR	5.00 SNR	1.00 SNR	0.50 SNR	0.10 SNR	0.05 SNR	0.01 SNR
10° steps	0.00	0.00	0.10	0.25	0.75	1.00	1.00
15° steps	0.00	0.00	0.25	0.25	1.00	1.00	1.00
20° steps	0.00	0.10	0.25	0.50	1.00	1.00	1.00

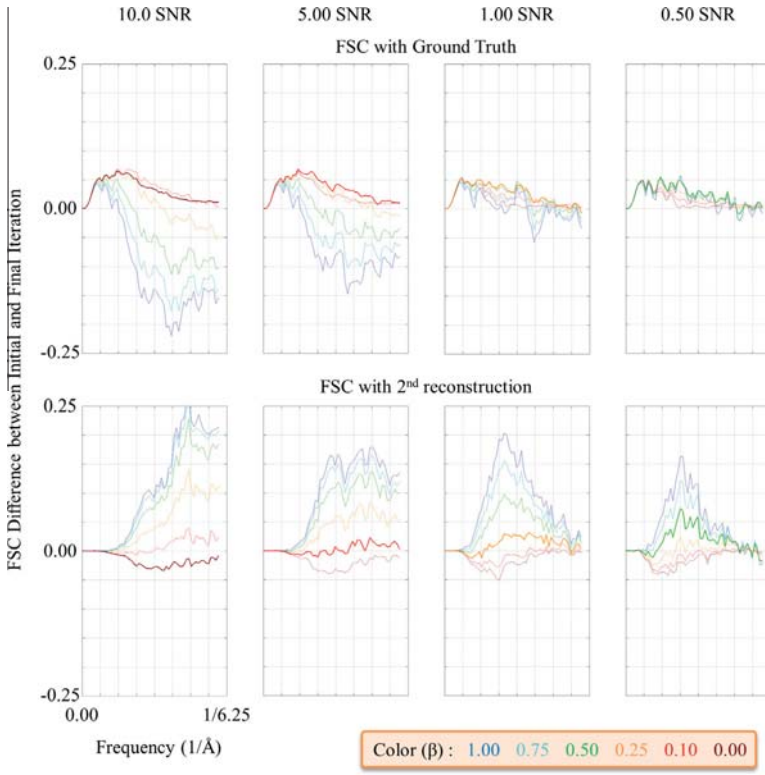

Fig. 3. Effect of regularization weight (β) on the history of Fourier shell correlation (FSC). Top: the differences of the ground truth FSCs between the final and initial iteration of the sequential maximum *a posteriori* probability expectation maximization (sMAP-EM) reconstructions. For each signal-to-noise ratio (SNR), the differences are plotted for all the six independent reconstructions with different β values. The β yielded the largest FSC improvement were almost identical to the optimal β for the mean squared error in the 3D domain (MSE3D; thick line). Bottom: the difference in the FSCs with 2nd reconstructions for the sMAP-EM method. The trend of the FSC with another noisy realization of the sMAP-EM reconstruction with the same noise level was very different from the FSC with the noise-free ground truth. Through all the iterations, the reconstructions with the optimal β values for the MSE3D (thick line) and for the FSC with ground truth tended to show the smallest change in the FSC with 2nd reconstruction among the six different β value reconstructions.

relations to the ground truth free methods (MSD2D and the FSC with 2nd reconstruction) were investigated.

As expected, the two different methods of ground truth based evaluation showed a consistent result. The β value yielding the minimum MSE3D (optimal β value; Table 1) strongly tended to produce the best result of the FSC with ground truth (Fig. 3 top and Supporting Fig. 2). The optimal β became larger for the lower SNR and the larger angular steps. When the β was too small for a given experimental condition, the error started to increase in the middle of the iterations (Supporting Fig. 3). This indicates that a stronger regularization with a larger β value is necessary for a greater noise reduction and a stronger robustness against the sampling sparseness.

The relation between the optimal β value and the MSD2D was not conclusive (Supporting Fig. 4). The optimal β values did not produce the minimum MSD2Ds at all the noise level, instead $\beta = 0$ always did. However, the MSD2D monotonically decreased throughout the iterations regardless of the β value neither the noise levels. The sMAP-EM reconstruction convergences to noisy observations produces a noisy 3D density map, but the introduction of a proper regularization weight makes the final structure closer to the ground truth as can be seen in Supporting Fig. 3.

On the contrary, the history of the FSC with 2nd reconstruction was quite informative about the optimal β value (Fig. 3 bottom). The reconstruction with the optimal β value tended to show the smallest change between the initial and final iteration at almost all frequency bands among the six different β values. These tendencies were consistent at all the noise levels with all degrees of sparseness. This observation showed that the FSC between two independent reconstructions can be used to estimate the optimal

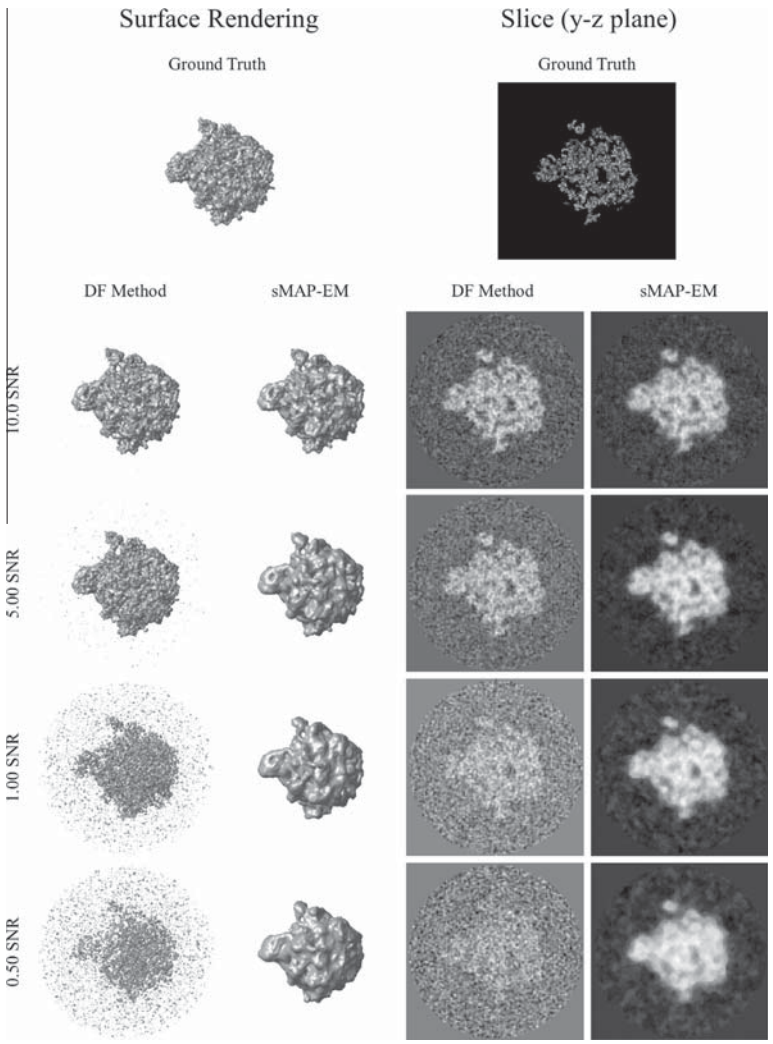

Fig. 4. 3D reconstructions of 20° angular sampling relative to the noise level. Left: surface renderings of the resulting 3D reconstructions with the DF method (left column) and sMAP-EM (right column) relative to the SNR of simulated projections. The ground truth is shown at the top. The 3σ value of the density distribution is used as the threshold. Right: corresponding y–z slices. Each slice is scaled individually with the full intensity range for the visualization. The sMAP-EM is less affected by the SNR variation and makes the visual assessment possible even at the low SNR without applying additional post processing.

β value for the sMAP-EM reconstruction of the experimental cryo-EM images, even if the ground truth is not available.

4.2. Experiment A2: evaluation of selected sMAP-EM reconstructions

To understand the basic characteristics of the 3D sMAP-EM relative to noise level and angular sampling sparseness, the optimal sMAP-EM reconstructions selected in the experiment A1 were compared with the DF reconstructions. From the visual impression (Fig. 4), it is clear that the sMAP-EM has a superior ability to handle the high noise level and the sparse sampling. Since the sparse sampling was our interest, the reconstructions with 20° sampling steps are presented for the noise effect. Even the small features in the sMAP-EM reconstruction are clearly observable at the worst 0.50 SNR. With the decrease of the input SNR, the structures became smoother because of a stronger regularization. However, the obvious structural deformation or serious loss of the details were not observed. In contrast, noise in the DF reconstructions became notable and obscured the target object below the 1.00 SNR. The increase of the sampling sparseness at 1.00 SNR affected the reconstructions in a similar way to the increase of the noise level (Fig. 5). These results indicate that the sMAP-EM is less sensitive to variations of both the noise level and angular sampling sparseness than the DF method.

The numerical evaluations were consistent with the visual assessment, supporting the advantage of the sMAP-EM over the DF method (Fig. 6). According to the MSE3D (left), the sMAP-EM resulted in smaller errors than the DF method at all the SNRs and the angular sampling steps. The errors of the two methods are close to each other at the best SNR (10.0). As the noise level increases, the error of the DF reconstructions rapidly increases while the increase is slow with the sMAP-EM method. At the worst

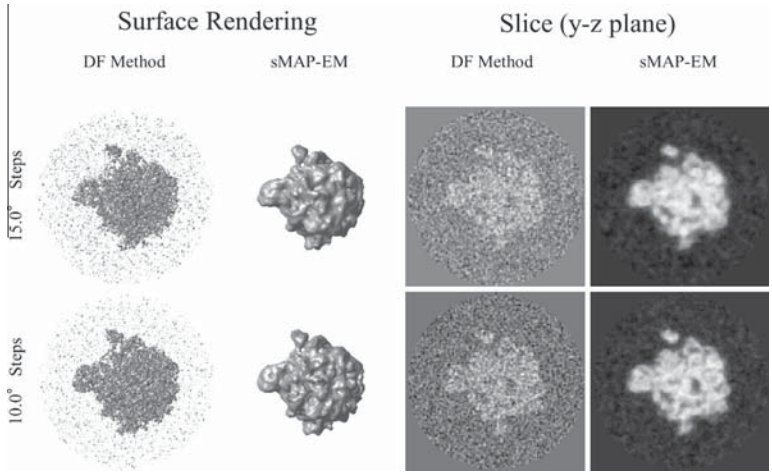

Fig. 5. 3D reconstructions of 15° and 10° angular sampling with 1.00 SNR. Left: surface renderings of the resulting 3D reconstructions with DF method (left column) and sMAP-EM (right column), at the 3σ density threshold. Right: corresponding y–z slices. The full intensity range of each slice is visualized. The sparseness of angular sampling affected the both reconstruction methods similarly as the input SNR variation did; the increase of angular sampling decreased the noise level in the reconstructions and increased visibility of the details.

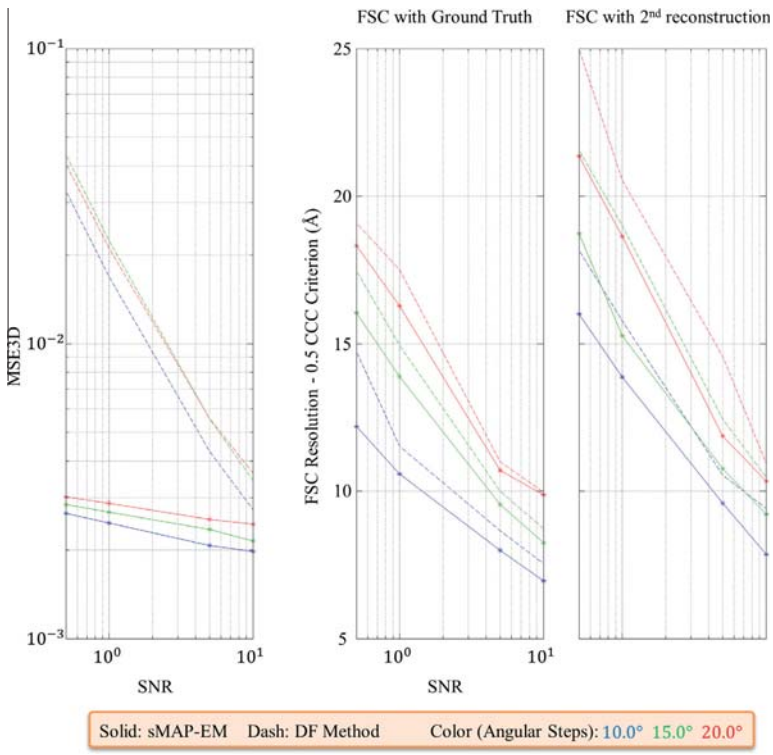

Fig. 6. Numerical evaluation of 3D reconstructions with equally distributed angular sampling. Left: MSE3D of reconstructions relative to the ground truth. The sMAP-EM shows less errors than the DF method at all the SNRs and the angular samplings. With both methods, the errors reduce when the SNR increases or the angular sampling becomes denser. The gradual slope of the sMAP-EM error curves support the noise robustness of this method. Right: FSC resolutions by the correlation coefficient 0.5 criterion relative to the ground truth and another realization of reconstruction. The sMAP-EM resulted in a better resolution than the DF method at all the SNR values and the angular steps. The resolution improves when the SNR increases or the angular sampling becomes denser.

Table 2
β values of termination stages in the experiment B.

10.0 SNR	5.00 SNR	1.00 SNR	0.50 SNR
0.01	0.01	0.10	0.20

SNR (0.5), the sMAP-EM error is ten times smaller than the DF method error. The increase of sampling sparseness also caused the increase of MSE3D in both the sMAP-EM and the DF method, but the effect was smaller compared with the SNR variation (Fig. 6). The FSC evaluation showed that the sMAP-EM reconstruction also resulted in better resolutions than the DF method at all the SNRs and the angular steps (right). To see the effects of these two variables together, the FSC resolutions by the correlation coefficient 0.5 criterion were calculated from the FSC functions (Supporting Fig. 5). In general, the resolution worsened when the SNR increased or the angular sampling became sparser. All the resolutions by the FSCs with 2nd reconstructions were worse than the corresponding resolutions by the FSCs with ground truth, indicating the FSC between two independent reconstructions did not overestimate the resolution for neither of the reconstruction methods.

4.3. Experiment B: assessment of artifact suppression by gap-filling ability

The purpose of this experiment was to evaluate the artifact suppression by the gap-filling ability of the 3D sMAP-EM. Simulated datasets of conical tilt sampling were used because of its clearly defined missing cone. To ensure the gap filling, this experiment used the multiple stage setting with the same β value set as described in the previous studies ($\beta = 1.0, 0.9, \ldots, 0.1, 0.01$) (Paavolainen et al., 2014; Tuna et al., 2013). Since the ground truth is available in the simulation study, the MSE3D was used to terminate the stage sequence of the sMAP-EM. The process was terminated at the stage when the MSE3D stopped to decrease and reached to the minimum error. The β value of the termination stage at each noise level is reported in Table 2.

In terms of the noise robustness, the MSE3D, and the FSC resolution, the advantages of the sMAP-EM over the DF method were clear with the conical tilt sampling (Supporting Figs. 6 and 7). The superior noise reduction in the sMAP-EM reconstructions allowed the visual inspection of the features with low intensity values. The artifacts in the sMAP-EM reconstructions showed no obvious dependency on the input SNR, except the increase of smoothness because of the selected β values. In contrast, the resulting noise level in the DF reconstructions became too high to visually inspect the low intensity details below the 1.00 SNR. The effect of the missing cone in the DF reconstructions was recognizable through the vertically elongated noise grains in the background space.

To visually investigate the suppression of the limited angular artifacts by sMAP-EM, the *x*-axis views were reprojected from the ground truth and the reconstructed volumes of 10.0 SNR (Fig. 7A). By comparing the details of a region of interest, both reconstruction methods produced similar image quality in the horizontal direction (from comparing the bright pixels between red lines). However, the reprojection of sMAP-EM shows sharper top–bottom boundaries of the object (yellow lines) and higher similarity to the ground truth, comparing with the DF method. The elongation artifact makes the impression of the DF reconstruction longer in the diagonal direction (from top-right to bottom-left) than in the other directions.

The 3D Fourier transforms of the resulting reconstructions visually show that the sMAP-EM has the ability to fill meaningful information in missing cone (Fig. 7B). For both the sMAP-EM and the DF method, the differences of amplitudes in the measured angular space were small between the ground truth and the reconstructions at 10.0 SNR. However, the low frequency range of the missing cone was clearly filled with information only in the sMAP-EM reconstruction. The filled information is similar to the corresponding information of the ground truth, but the amplitude decreases as the frequency increases. The DF reconstruction has a clear boundary of the missing cone, showing no evidence of gap filling ability.

The proposed numerical measurements supported the visual assessment of the filled information in the missing cone of the sMAP-EM reconstructions (Fig. 8). The FSMAR (top) shows that all the sMAP-EM curves clearly have high amplitude ratios at the low frequency range up to 33 Å resolution (3rd tick). On the other hand, the curves of the DF method show that the amplitude ratios are low and almost constant in the whole frequency range, indicating that the amplitude in the missing cone is on the background noise level. The FSMSE (middle) showed smaller errors of the sMAP-EM compared with the DF method in the low frequency range of the missing cone. The bias (error mean) and error variance explained the nature of the difference (Supporting Fig. 8). The MSE of the sMAP-EM reconstruction was more described by the error variance than the bias. On the other hand, the major portion of the MSE in DF reconstructions was originated from the large bias and the error variance was small. The reduction in the bias of the sMAP-EM relative to the DF method reflects the degree of the amplitude restoration in the missing cone, since the absence of gap-filling should make the bias equal to the missing cone mean amplitude of the ground truth. Although the error variance was large for the sMAP-EM, its MSE was still lower than the DF method. This indicates that the information filling had a positive effect on the quality of the reconstruction. To investigate whether the filled information actually have the correct amplitudes and phases compared to ground truth, the FSC curves relative to the ground truth were calculated by masking out the measured angular space in the frequency domain (bottom). For the sMAP-EM reconstructions, the most of the correlation values at the lower frequency range are higher than 0.143, indicating the estimated signals are not random (Rosenthal and Henderson, 2003). Whereas, the FSC curves of the DF reconstructions show that most of the correlation values are below 0.143. However, we observe large negative correlations around the frequency of 33 Å resolution (3rd tick) with both DF method and sMAP-EM. This indicates that the contrast of estimated density values at these particular frequencies was incorrectly inverted in the spatial domain (Penczek, 2010b). This might be caused by the particular relationship between the frequency composition of the structure itself and the position of the missing wedge.

4.4. Experiment C: reconstruction from the experimental cryo-EM images

The 3D sMAP-EM was evaluated with the experimental cryo-EM dataset of the 50S ribosomal subunit. Reflecting the observation in the experiment A1, we first selected a proper regularization weight for each angular sampling condition. For a given condition, the eleven reconstructions were conducted with the single stage setting using $\beta = 1.0, 0.9, \ldots, 0.1, 0.01$. The regularization weight which yielded the minimum change in the FSC with 2nd reconstruction was selected (Table 3). By setting termination of the process to the stage associated with this selected regularization weight, the sMAP-EM reconstructions with multiple stage setting were conducted to evaluate the sampling sparseness effect.

The result demonstrated that the sMAP-EM method has superior robustness against the angular sampling sparseness and the

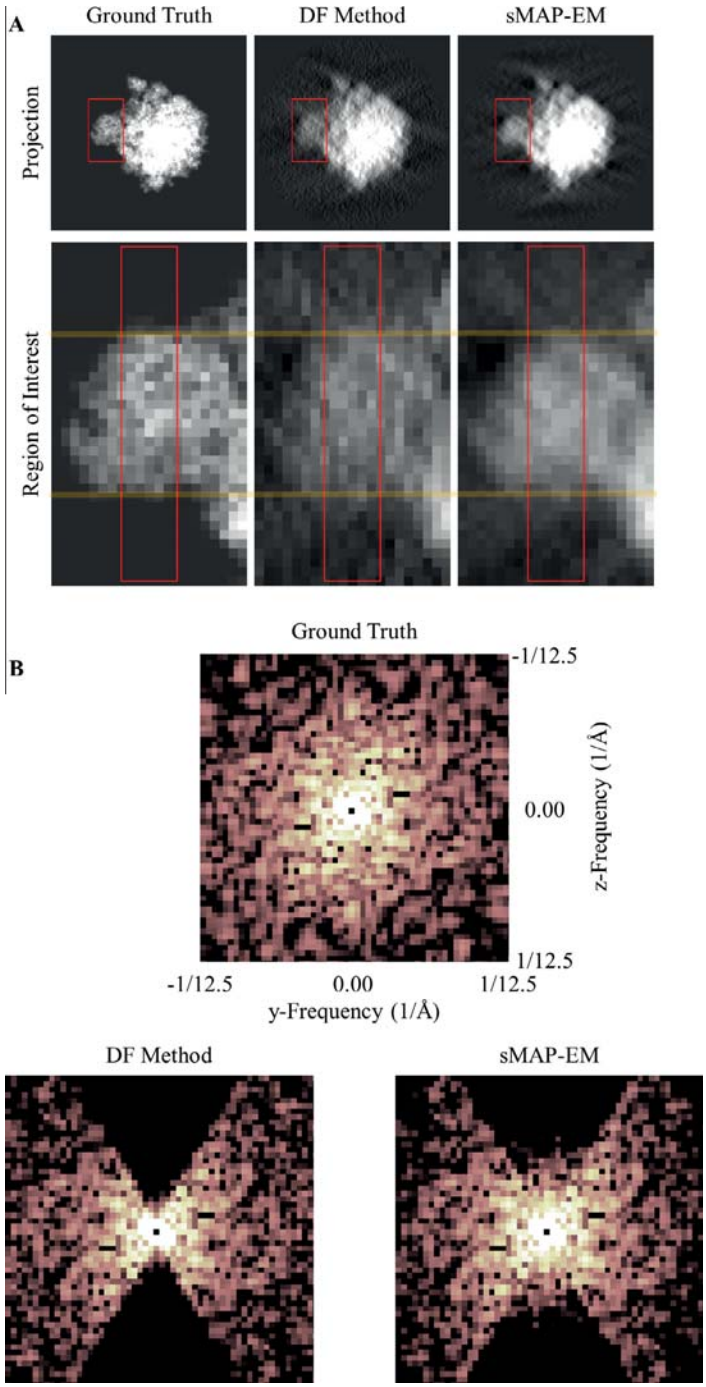

Fig. 7. Visual assessment of the limited angular sampling artifact in the spatial domain and of the missing cone in the frequency space. (A) Visualization of the limited angular sampling artifacts in the spatial domain. The *x*-axis views are reprojected from the ground truth and the reconstructed volumes of 10.0 SNR (top). Their details (bottom) of a region of interest (red box in top) are also shown. The original pixel intensities are kept. The sMAP-EM projection shows a higher similarity to the ground truth, comparing with the DF method. (B) Visualization of the missing cone in the frequency space. A representative central slice of the ground truth (top) in the 3D Frequency domain (*x* axis view). Corresponding central slice of the DF (bottom left) and sMAP-EM reconstructions (bottom right). Only the reconstructions at 10.0 SNR are shown. The same range of the log-scaled amplitudes is used for the visualization of all central slices. Only the central area up to the half of the Nyquist frequency (12.5 Å resolution) is shown to demonstrate the information filling in the missing cone area. In contrast to the DF method, the sMAP-EM clearly filled information in the low frequency range of the missing cone.

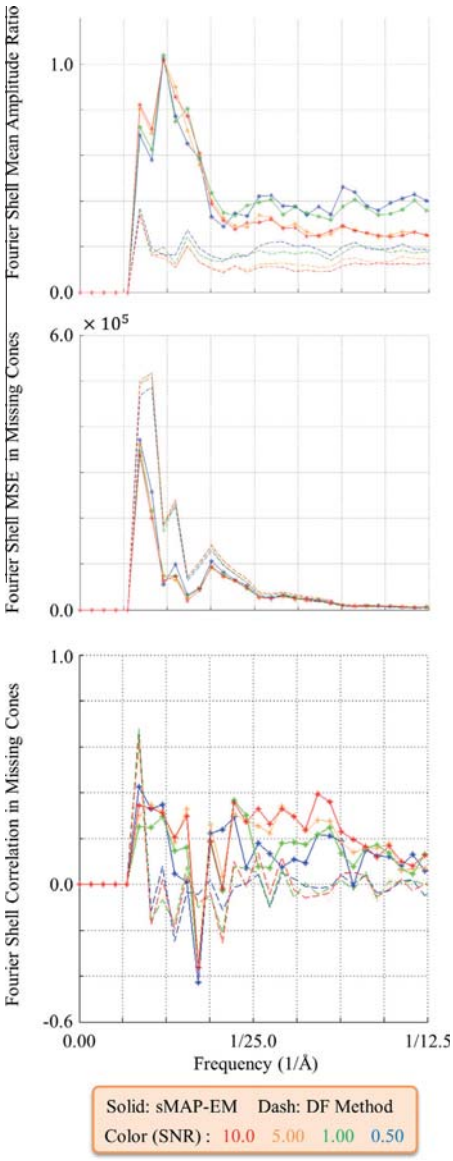

Fig. 8. Numerical evaluation of information filling in missing cone. Top: Fourier shell mean amplitude ratio (FSMAR) of the DF and sMAP-EM reconstructions, defined as the ratio between the mean amplitude in the missing cone and in the observed angle space at each frequency band. The ratio of a reconstruction was normalized by the ground truth. The frequency up to the half of the Nyquist frequency is shown. The high ratios at the low frequencies in the sMAP-EM show that the information other than background noise is filled in the missing cone. Middle: Fourier shell mean squared error (FSMSE) in the missing cones of the two methods. The smaller errors of sMAP-EM compared with of DF method at the low frequency range of the missing cone support the information filling in the sMAP-EM reconstruction. Bottom: Fourier shell correlation (FSC) relative to the ground truth. The correlation values are calculated only in the missing cone region by masking out the measured angular space in the frequency domain. The most of the correlation values are higher than 0.143 for the sMAP-EM reconstructions, indicating the estimated signals are not random. Whereas, the FSC curves of the DFM reconstructions show that correlation values at almost all frequencies are below 0.143.

Table 3
β values of termination stages in the experiment C.

196 classes	91 classes	46 classes
0.1	0.1	0.2

noise compared with the DF method. In Fig. 9, the MAP-EM reconstructions have less noisy impression and they show clearer small details no matter how many Euler angle classes were used. The noise level and the smoothness of the sMAP-EM reconstructions was almost constant, while the noise level in the DF reconstruction varied depending on the number of the classes. The numerical evaluation was consistent with the visual impression (Fig. 10A). Regardless of the sampling sparseness (right), the sMAP-EM yielded better resolutions measured with the FSC with 2nd reconstruction. However, the stricter selection of the Euler angle classes improved the resolution of both the sMAP-EM and the DF reconstructions despite of the increase in the sampling sparseness. This is because the 50S ribosomal subunit particles in the cryo-EM dataset strongly preferred the orientations around (0°, 20°) (Fig. 10B). In consequence, the class averages of the particle images near the preferred orientation were almost noiseless and their details were clear, while the image qualities of the other averages were extremely low. By discarding the low quality class averages, the class selection improved the total quality of the input dataset. The improvement was expressed by the FSC with 2nd reconstruction. The Euler angle class selection has a tradeoff between the total quality of input dataset and angular sampling density. In our results, the increase of total quality affected the FSC improvement stronger than the decrease of sampling density.

5. Discussion

In the current study, we applied a MAP estimate based statistical reconstruction method to the limited angular sampling problem in the *ab initio* 3D reconstruction step of SPR. Here, the model with less artifacts is assumed to be better for the subsequent 3D refinement. It is important to note that the relationship between the quality of the initial model and the associated achievable optimum depends also on the optimization algorithm used for the 3D refinement iterations. In this study, we concentrated only on producing a high-quality initial model from sparse projections, and all evaluations of the reconstruction method were designed for testing the achievable quality. All the results of visual and numerical evaluations showed the superior performance of the sMAP-EM over the DF method in the case of limited angular sampling as well as of an extremely high input noise. The greater noise reduction in the reconstructions allows the visual assessment even with extremely high nose level of input projection images. This advantage eliminates the necessity of any additional pre- or post-processing for the noise. Comparing with the DF reconstruction, the error of the sMAP-EM reconstruction relative to the ground truth is smaller and the FSC resolution is better for all the input SNRs and the angular steps used in this paper. The advantage of sMAP-EM was independent of the angular sampling method. Notably, all our visual and numerical evaluations in the frequency domain supported that the sMAP-EM can fill meaningful information in the unmeasured angular space.

For the purpose of the current study, we assume that the approximation error from the used pseudo-inverse CTF operation is negligible. For the *ab initio* 3D reconstruction, the 2D class average images are commonly used instead of individual particle images. Each average consists of the particle images taken over dif-

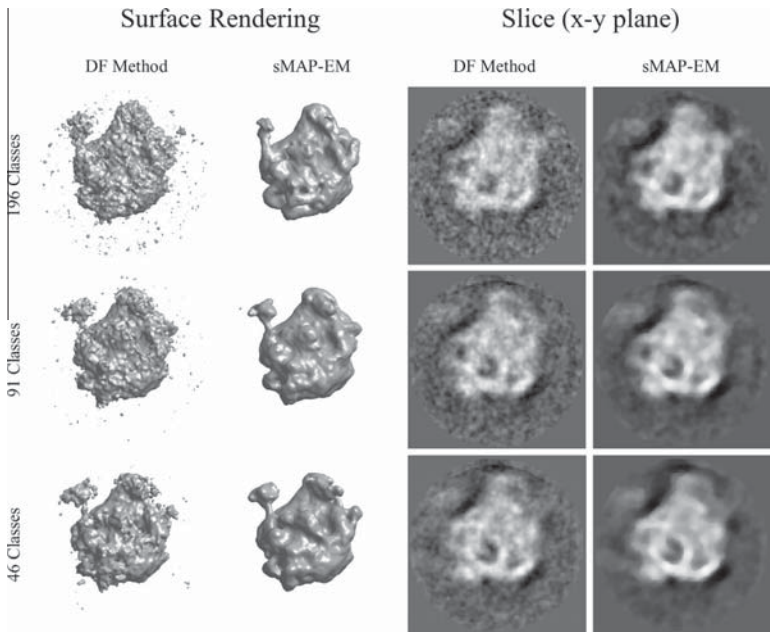

Fig. 9. 3D reconstructions of cryo-EM dataset relative to the angular sampling sparseness. Left: surface renderings of the resulting 3D reconstructions with DF method and sMAP-EM. The density threshold was independently adjusted for each reconstruction. Right: corresponding *x*–*y* slices, individually scaled with the full intensity range. The noise levels of the DF reconstructions are higher than the sMAP-EM reconstructions for all the class selections. Regardless of the angular sampling sparseness (expressed by the number of the selected Euler angle classes), the noise level and the smoothness of the sMAP-EM reconstructions was almost constant.

ferent defocus values. With this manner, the 2D class averaging is known to recover information at all frequencies (Frank, 2006). However, for the possible application of sMAP-EM to the 3D Refinement, it would be desirable to incorporate the CTF in the image formation model to enable the full CTF correction of the reconstructed density map, like the other existing 3D Refinement algorithms in the SPR field.

One useful feature of sMAP-EM is that the algorithm automatically finds the best balance between reducing the noise and preserving the structural feature. This will remove the necessity of manually finding a proper frequency filtering before, during, and after the reconstruction process. Instead, the regularization weight (β) needs to be roughly adjusted to achieve the best balance. The insufficient noise reduction with a small β value will result in noisy reconstruction and make the interpretation of the structures difficult. On the other hand, the excessive noise reduction will smooth the structure too much, and this can cause the deformation, loss of the fine features, and an impression of blobby painting (Alenius, 1999). With large regularization weight, the consistency between two realizations of the sMAP-EM reconstructions can be artificially high and the FSC between two independent reconstructions will overestimate the resolution (Penczek, 2010b).

In practice, considering only a few small β values should be sufficient in a certain application where the sMAP-EM would be used, since the variations of the SNR and the angular sampling density are usually small. In the current study, our aim was to investigate a wide range of the regularization weights and to find the practical range for the SPR application. For this, we adapted the experimental design of a previous SPR study where the authors proposed the comprehensive assessment of multiple measurements and their histories to reveal the characteristic and behavior of the SPR iterative processes (Moriya et al., 2013). As a result, we could estimate that the practical range of β is 0.1–0.2 for the experimental cryo-EM dataset. Also the expectations for the reference-based 3D refinement step would affect the choice of the β value. For prevention of the reference bias, the reference structure is typically smoothed by a low pass filter with a very low cutoff frequency (Scheres, 2012a). For this practice, a large regularization weight β near 1.0 might be a preferable choice. However, as discussed above, this setting has to take into account the possibility of resolution overestimation by the FSC between two independent reconstructions. In addition, our simulation studies showed that the wide range of the β values near the optimal yields similar MSE3D values and FSC curves. Therefore, keeping the regularization weight not too far away from the optimal is sufficient to keep a proper balance between the noise reduction and the structural feature preservation.

The uniqueness of the sMAP-EM is the gap filling ability (Paavolainen et al., 2014; Tuna et al., 2013). The method is robust against the limited angular sampling by actively filling meaningful frequency information in the unmeasured angular space. The gap filling ability is originated from the MRP. In our implementation, the iteration cycle of the likelihood coefficient uses the simple back-projection to reconstruct the coefficients in the 3D domain from the correction projection 2D images in the spatial domain. The 3D likelihood coefficient will always have the information gaps in its 3D Fourier transformation. However, the 3D penalty coefficient calculated in the spatial domain fills frequency information in the gap. The gap-filling is possible because the median filter in our regularization has an edge preservation property which fills frequency information in missing gap. Therefore, the regularization term also acts as an interpolation operation in the frequency domain. The source information of the interpolation comes from the relation of pixel values in the local neighborhood. At the first iteration, the initial gap filling by the regularization with median filtering occurs only around the edge of unmeasured angular space

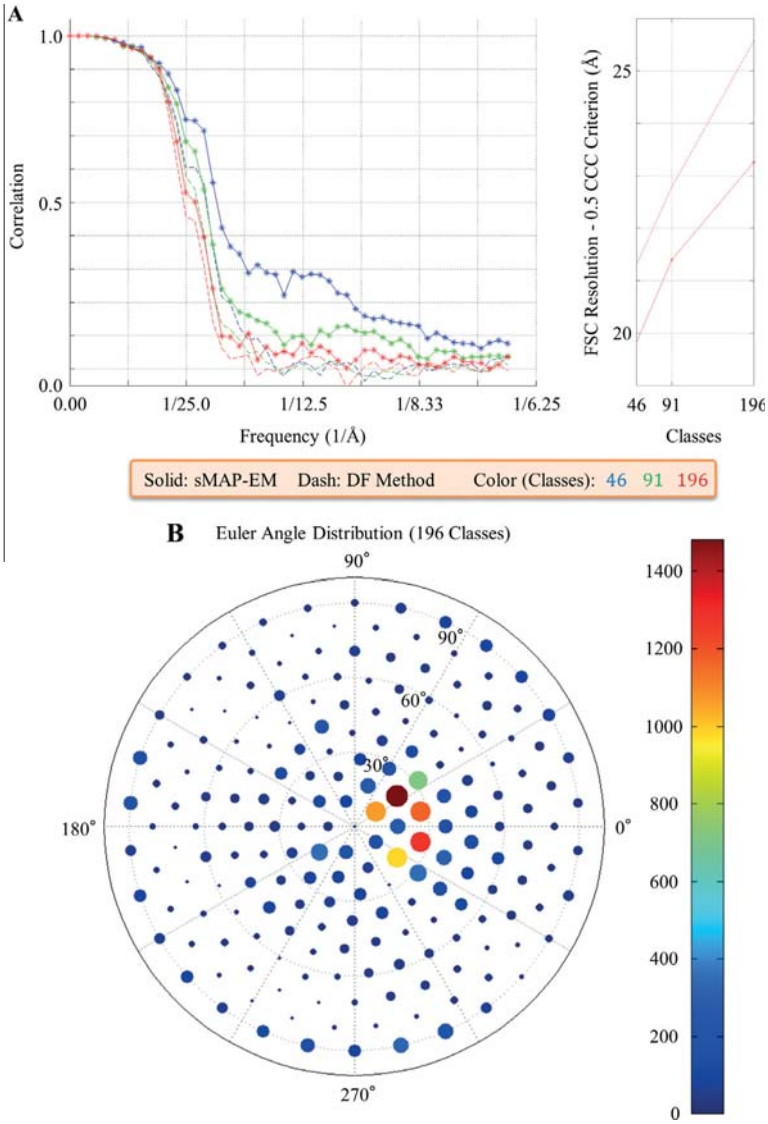

Fig. 10. FSC evaluations of the reconstructions and Euler angle distribution of cryo-EM dataset. Top: functions of the FSC with 2nd reconstruction and the corresponding resolutions by the correlation coefficient 0.5 criterion. The sMAP-EM reconstructions have better resolutions than the DF reconstructions with all the class selections. For both of the reconstruction methods, the resolution improves as less class averages are used. Bottom: surface projection of Euler angles of 16,512 particles assigned into 196 equally distributed angles. The angular and radial coordinates correspond to the first and second angles in the Euler angle with the *zyz* convention. The size and color of each circle indicate the number of particles images assigned to the corresponding Euler angle coordinate. This experimental dataset of the 50S ribosomal subunit shows that the particles have a strong preferred orientation.

as a result of the edge preservation using the local neighbor pixel values as the information source. The extent of filling is limited by the matrix size of the median filter. This filled information is preserved and updated by successive iterations. During the iterations, the gap filling occurs more toward the center of the gap arc by using the previously estimated information in the missing gap. At the same time, the improvement of estimation accuracy gradually propagates along the gap arc with the same manner. However, the estimation error is likely to accumulate during the propagation, and is expected to be higher at the point further away from the observed angular space. The drawback of this gap filling is that the filling of meaningful frequency information requires a large number of iterations. This is especially the case for the high frequency information because this information can only be reconstructed with a small regularization weight. Therefore, our future agenda is to find a way for reducing the computation time by reducing the sufficient number of iterations for the gap filling.

The above discussion of gap-filing mechanism suggests that also other MAP estimate based reconstruction methods may have potential to fill the missing gaps if the regularization term

influences the frequency information in the unmeasured angular region and the update function does not wipe out the filling from the previous iterations. For example, the Kucukelbir et al. (2012) have used an adaptive basis to represent the estimated density map using a two-level, stationary wavelet transform-based frame and a sparse prior (enforcing the usage of the smallest number of bases or most of coefficients of each bases are close to zero) in the 3D spatial domain. This kind of representation should also be able to provide the frequency information in the missing gaps.

6. Conclusion

The current study demonstrated that the proposed sMAP-EM method has the additional advantage of the gap filling in addition to the general noise robustness of the statistical reconstruction methods. These advantages allow quick visualization of protein structure without any additional post-processing, even for the reconstruction from a noisy dataset with limited angular sampling due to a small number of observed particle images. The gap filling ability is especially useful for suppressing the limited angular sampling artifacts in the initial estimation of 3D density map, and reducing errors of 3D refinement due to the reference bias. The sMAP-EM also has an ability to handle the preferred orientation problem of proteins, and can be applied after the 3D refinement step when the resulting Euler angle distribution indicates that the angular sampling is significantly uneven and sparse. Furthermore, like the other existing MAP-EM based algorithms in the SPR field, the sMAP-EM can be expanded to handle the simultaneous 3D angle estimation and 3D classification of conformations by adding associated parameters into the statistical model: Euler angle, in-plane translation, and conformation identification numbers for each particle image. We believe that these advantages of sMAP-EM can contribute a further resolution revolution of SPR, facilitating the reconstruction with near atomic-resolution even for 100–500 kDa proteins with low symmetries.

Acknowledgements

The funding of this work was provided by Tekes FiDiPro 1913/31/2012 and Tampere University of Technology Internal Grant.

Appendix A. Supplementary data

Supplementary data associated with this article can be found, in the online version, at http://dx.doi.org/10.1016/j.jsb.2015.07.007.

References

Alenius, S., 1999. On Noise Reduction in Iterative Image Reconstruction Algorithms for Emission Tomography: Median Root Prior. Tempere University of Technology, Tempere.
Alenius, S., Ruotsalainen, U., 2002. Generalization of median root prior reconstruction. IEEE Trans. Med. Imaging 21, 1413–1420.
Delaney, A.H., Bresler, Y., 1998. Globally convergent edge-preserving regularized reconstruction: an application to limited-angle tomography. IEEE Trans. Image Process. 7, 204–221.
Dempster, A.P., Laird, N.M., Rubin, D.B., 1977. Maximum likelihood from incomplete data via the EM algorithm. J. R. Stat. Soc. Ser. B 39, 1–38.
Frank, J., 2006. Three-Dimensional Electron Microscopy of Macromolecular Assemblies: Visualization of Biological Molecules in Their Native State, second ed. Oxford University Press, New York.
Green, P.J., 1990. Bayesian reconstructions from emission tomography data using a modified EM algorithm. IEEE Trans. Med. Imaging 9, 84–93.
Hanson, K.M., Wecksung, G.W., 1983. Bayesian approach to limited-angle reconstruction in computed tomography. J. Opt. Soc. Am. 73, 1501–1509.
Henderson, R., 2013. Avoiding the pitfalls of single particle cryo-electron microscopy: Einstein from noise. Proc. Natl. Acad. Sci. U.S.A. 110, 18037–18041.
Herman, G.T., Hurwitz, H., Lent, A., Lung, H.-P., 1979. On the Bayesian approach to image reconstruction. Inf. Control 42, 60–71.
Herman, G.T., Odhner, D., 1991. Performance evaluation of an iterative image reconstruction algorithm for positron emission tomography. IEEE Trans. Med. Imaging 10, 336–346.
Hohn, M., Tang, G., Goodyear, G., Baldwin, P.R., Huang, Z., Penczek, P.A., Yang, C., Glaeser, R.M., Adams, P.D., Ludtke, S.J., 2007. SPARX, a new environment for Cryo-EM image processing. J. Struct. Biol. 157, 47–55.
Kucukelbir, A., Sigworth, F.J., Tagare, H.D., 2012. A Bayesian adaptive basis algorithm for single particle reconstruction. J. Struct. Biol. 179, 56–67.
Kühlbrandt, W., 2014. Biochemistry. The resolution revolution. Science 343, 1443–1444.
Levitan, E., Herman, G.T., 1987. A maximum a posteriori probability expectation maximization algorithm for image reconstruction in emission tomography. IEEE Trans. Med. Imaging 6, 185–192.
Liao, M., Cao, E., Julius, D., Cheng, Y., 2013. Structure of the TRPV1 ion channel determined by electron cryo-microscopy. Nature 504, 107–112.
Lyumkis, D., Brilot, A.F., Theobald, D.L., Grigorieff, N., 2013. Likelihood-based classification of cryo-EM images using FREALIGN. J. Struct. Biol. 183, 377–388.
Moriya, T., Mio, K., Sato, C., 2013. Novel convergence-oriented approach for evaluation and optimization of workflow in single-particle two-dimensional averaging of electron microscope images. J. Electron. Microsc. (Tokyo) 62, 491–513.
Paavolainen, L., Acar, E., Tuna, U., Peltonen, S., Moriya, T., Soonsawad, P., Marjomäki, V., Cheng, R.H., Ruotsalainen, U., 2014. Compensation of missing wedge effects with sequential statistical reconstruction in electron tomography. PLoS ONE 9, e108978.
Penczek, P.A., 2010a. Fundamentals of three-dimensional reconstruction from projections. Methods Enzymol. 482, 1–33.
Penczek, P.A., 2010b. Resolution measures in molecular electron microscopy. Methods Enzymol. 482, 73–100.
Pettersen, E.F., Goddard, T.D., Huang, C.C., Couch, G.S., Greenblatt, D.M., Meng, E.C., Ferrin, T.E., 2004. UCSF Chimera – a visualization system for exploratory research and analysis. J. Comput. Chem. 25, 1605–1612.
Radermacher, M., Wagenknecht, T., Verschoor, A., Frank, J., 1986. A new 3-D reconstruction scheme applied to the 50S ribosomal subunit of *E. coli*. J. Microsc. 141, RP1–RP2.
Rosenthal, P.B., Henderson, R., 2003. Optimal determination of particle orientation, absolute hand, and contrast loss in single-particle electron cryomicroscopy. J. Mol. Biol. 333, 721–745.
Scheres, S.H.W., 2010. Classification of structural heterogeneity by maximum-likelihood methods. Methods Enzymol. 482, 295–320.
Scheres, S.H.W., 2012a. RELION: implementation of a Bayesian approach to cryo-EM structure determination. J. Struct. Biol. 180, 519–530.
Scheres, S.H.W., 2012b. A Bayesian view on cryo-EM structure determination. J. Mol. Biol. 415, 406–418.
Scheres, S.H.W., Núñez-Ramírez, R., Sorzano, C.O.S., Carazo, J.M., Marabini, R., 2008. Image processing for electron microscopy single-particle analysis using XMIPP. Nat. Protoc. 3, 977–990.
Shaikh, T.R., Gao, H., Baxter, W.T., Asturias, F.J., Boisset, N., Leith, A., Frank, J., 2008. SPIDER image processing for single-particle reconstruction of biological macromolecules from electron micrographs. Nat. Protoc. 3, 1941–1974.
Sigworth, F.J., Doerschuk, P.C., Carazo, J.M., Scheres, S.H.W., 2010. An introduction to maximum-likelihood methods in cryo-EM. Methods Enzymol. 482, 263–294.
Tang, G., Peng, L., Baldwin, P.R., Mann, D.S., Jiang, W., Rees, I., Ludtke, S.J., 2007. EMAN2: an extensible image processing suite for electron microscopy. J. Struct. Biol. 157, 38–46.
Tuna, U., Sohlberg, A., Ruotsalainen, U., 2013. Can we reduce SPECT acquisition time using MAP-EM reconstruction? J. Pattern Recognit. Intell. Syst. 1, 54–63.
Van Heel, M., 2013. Finding trimeric HIV-1 envelope glycoproteins in random noise. Proc. Natl. Acad. Sci. U.S.A. 110, E4175–E4177.
Van Heel, M., Portugal, R., Rohou, A., Linnemayr, C., Bebeacua, C., Schmidt, R., Grant, T., Schatz, M., 2011. Four-dimensional cryo electron microscopy at quasi atomic resolution: 'IMAGIC4D'. In: Arnold, E., Himmel, D.M., Rossmann, M.G. (Eds.), Crystallography of Biological Macromolecules. Wiley, New York, pp. 624–628.
Van Heel, M., Schatz, M., 2005. Fourier shell correlation threshold criteria. J. Struct. Biol. 151, 250–262.
Voss, N.R., Lyumkis, D., Cheng, A., Lau, P.-W., Mulder, A., Lander, G.C., Brignole, E.J., Fellmann, D., Irving, C., Jacovetty, E.L., Leung, A., Pulokas, J., Quispe, J.D., Winkler, H., Yoshioka, C., Carragher, B., Potter, C.S., 2010. A toolbox for ab initio 3-D reconstructions in single-particle electron microscopy. J. Struct. Biol. 169, 389–398.
You, J., Wang, J., Liang, Z., 2007. Range condition and ML-EM checkerboard artifacts. IEEE Trans. Nucl. Sci. 54, 1696–1702.

Publication III

E. Acar, S. Peltonen, and U. Ruotsalainen, “Adaptive multiresolution method for MAP reconstruction in electron tomography”, Ultramicroscopy, vol. 170, pp. 24–34, August 2016.

Ultramicroscopy 170 (2016) 24–34

Contents lists available at ScienceDirect

Ultramicroscopy

journal homepage: www.elsevier.com/locate/ultramic

Adaptive multiresolution method for MAP reconstruction in electron tomography

Erman Acar [a,b,*], Sari Peltonen [a,b], Ulla Ruotsalainen [a,b]

[a] Department of Signal Processing, Tampere University of Technology, P.O. Box 553, FI-33101 Tampere, Finland
[b] BioMediTech, Tampere University of Technology, Biokatu 10, 33520 Tampere, Finland

ARTICLE INFO

Article history:
Received 15 March 2016
Received in revised form
31 July 2016
Accepted 5 August 2016
Available online 6 August 2016

Keywords:
Adaptive reconstruction
Electron tomography (ET)
Maximum a posteriori (MAP) reconstruction
Missing wedge
Multiresolution reconstruction
Regularization parameter

ABSTRACT

3D image reconstruction with electron tomography holds problems due to the severely limited range of projection angles and low signal to noise ratio of the acquired projection images. The maximum a posteriori (MAP) reconstruction methods have been successful in compensating for the missing information and suppressing noise with their intrinsic regularization techniques. There are two major problems in MAP reconstruction methods: (1) selection of the regularization parameter that controls the balance between the data fidelity and the prior information, and (2) long computation time. One aim of this study is to provide an adaptive solution to the regularization parameter selection problem without having additional knowledge about the imaging environment and the sample. The other aim is to realize the reconstruction using sequences of resolution levels to shorten the computation time. The reconstructions were analyzed in terms of accuracy and computational efficiency using a simulated biological phantom and publically available experimental datasets of electron tomography. The numerical and visual evaluations of the experiments show that the adaptive multiresolution method can provide more accurate results than the weighted back projection (WBP), simultaneous iterative reconstruction technique (SIRT), and sequential MAP expectation maximization (sMAPEM) method. The method is superior to sMAPEM also in terms of computation time and usability since it can reconstruct 3D images significantly faster without requiring any parameter to be set by the user.

1. Introduction

Electron tomography (ET) is a widely used powerful technique in the field of biology revealing the interior structure of the biological samples in 3D at nanometer scale. This is achieved by collecting 2D projections of the specimen from different viewing angles. In its common application, the sample is rotated around a single axis with fixed intervals while its projections are acquired by transmission electron microscope. Then, these projections are used to reconstruct the biological sample in 3D. The accuracy and the resolution of the reconstruction are limited by two major factors: (1) due to the mechanical and physical limitations, the projections typically collected only from $\pm 60^\circ$ to 70° tilt angle range are used in the reconstruction (missing wedge problem). (2) The signal to noise ratio (SNR) of the projection data is low since the total amount of applied electrons is limited in order to prevent radiation damage to the biological sample imaged.

The maximum a posteriori (MAP) reconstruction methods are well suited for reconstruction from such incomplete and noisy projection data. They are able to use a priori information to compensate for the imperfection and incompleteness of the measurements. Any structural or statistical information about the sample or the imaging conditions can be utilized to improve the reconstruction process. These methods try to satisfy the fidelity of the reconstruction to the measurements and utilize the prior information at the same time. The balance between the data fidelity and the prior information is controlled by the regularization parameter. The value of this parameter highly affects the visual quality of the reconstructed image. Its optimum value depends on several factors, such as the noise level, sample variation, resolution, and validity of the prior information.

The computation of the regularization parameter in MAP estimation is usually based on the SNR analysis of the data, structural information about the objects reconstructed, or predefined set of parameters aiming to provide a solution as general as possible. One of these methods, the L-curve method, analyzes the images reconstructed for different values of regularization parameter [1]. For each reconstruction, the relationship between the squared

* Corresponding author at: Department of Signal Processing, Tampere University of Technology, P.O. Box 553, FI-33101 Tampere, Finland.
E-mail address: erman.acar@tut.fi (E. Acar).

http://dx.doi.org/10.1016/j.ultramic.2016.08.002
0304-3991/

norm of the solution and the squared norm of the residual error is analyzed to find the optimum regularization parameter. A similar approach, S-curve method, was implemented for wavelet-based reconstruction [2] and total variation regularization [3] making the assumption that the reconstructed data is sparse in wavelet domain and gradient domain, respectively. Both L-curve and S-curve methods require multiple reconstructions of the data with different regularization parameters, which heavily increases the computational cost of the overall image reconstruction. In another method, Wen and Chan used discrepancy principle for total variation regularization in the image restoration context [4]. Their method requires prior information about the SNR of the data, which is not always straightforward to obtain in tomographic imaging. In this study, one of our aims was to develop an adaptive regularization method, which does not require additional analysis, structural a priori information about the data nor the imaging system, or the user manipulation according to the application purpose.

The other aim of this paper was to reduce the computation time, which is realized by employing multiresolution reconstruction in a sequential scheme. Multiresolution reconstruction grids [5] and multiresolution detector space [6] was used previously to improve the convergence rate of maximum likelihood expectation maximization (ML-EM) method in positron emission tomography (PET). It was also utilized in scanning transmission electron microscopy (STEM) [7] and discrete tomography that reconstructs images composed of small number of intensity levels representing only a few different materials [8]. In this paper, we use the multiresolution method in electron microscopy for the reconstruction of biological specimens with maximum a posteriori probability expectation maximization (MAPEM) method. Multiresolution approach introduced in MAPEM reconstruction enables the weight of the regularization to vary from strong to weak throughout the reconstruction. One reason is that the image size is increased during the reconstruction while the regularization filter size is fixed. The other reason is the number of binned projection data and so its averaging effect decreases throughout different resolution stages. By decreasing noise with these two mechanisms, the reconstruction converges smoothly to a coarse estimate of the reconstructed image at the first resolution stages. Then the number of binned pixels is decreased step by step to improve the resolution of the estimates. Since each step is initialized with a spatially coarse estimate of the image, they give better results in fewer iterations compared to initialization with an image of random or constant value. The computations take shorter time also because the calculations are faster in the smaller reconstruction grids used in the lower resolution stages. We developed the adaptive regularization method first as a parameter-free reconstruction process and then introduced the multiresolution approach to obtain the final adaptive multiresolution reconstruction method.

2. Method

An accurate model for the formation of TEM images would be based on quantum and relativistic aspects of the illumination of the specimen, electron–specimen interaction, microscopy optics, and the detection of the electrons. However, this would be a computationally unfeasible model. Therefore, we apply some simplifications and statistical modeling to obtain a feasible image formation model.

A transmission electron microscope can be operated in different imaging modes depending on the illumination of the specimen, the contrast mechanism based on the interaction of the electrons with the specimen, and the detector type. In the dark field imaging mode, the detection of scattered electrons plays the major role in image formation, whereas it is the detection of transmitted electrons in bright-field imaging mode. We consider the bright field mode, used conventionally for ET in life sciences, in this study. In this imaging mode, a parallel beam of electrons illuminates the specimen, and the image is formed in the back focal plane of the objective lens by the electrons that pass through the aperture. For the image contrast mechanism, we only consider the amplitude contrast generated due to the electrons that are blocked from reaching the detector and we ignore the phase shift created by the electron-specimen interaction. This model is sufficient for medium-resolution contrast (beyond 2–3 nm) imaging however phase contrast should also be considered at higher resolutions where the features to be detected are smaller than the coherence length of the electron [9]. We also assume that successive electrons do not interact with each other so that they can be treated independently. This assumption holds for TEM imaging of biological specimens since the specimen is thinner than the mean distance between two successive electrons [10]. Under these assumptions the formation of the image can be expressed as:

$$p^{raw}(\theta) = C - \left\{ PSF * p(v, \theta) \right\}, \tag{1}$$

where $p^{raw}(\theta)$ is the data acquired for the tilt angle θ, C is the data that would be acquired if there was no specimen, PSF represents the point spread function of the imaging system, $*$ is the convolution operation, and $p(v, \theta)$ is the ray transform of v in the θ direction. The result of this transform can be expressed as a vector of elements p_d where

$$p_d = \sum_b v_b a_{db}. \tag{2}$$

Here, v_b is proportional to the probability that an incident electron traveling along θ is scattered inside the bth voxel of the discretized specimen volume. The contribution of the bth voxel to the dth projection data, p_d, is represented by a_{db}. C and PSF in (1) can be determined by separate calibration experiments and they can be excluded from the equation by subtraction and deconvolution. After this basic preprocessing of the raw data, the problem reduces to estimate the parameters of distribution describing v_b's in (2). In parallel beam projection geometry, the reconstruction space can be divided into slices orthogonal to the tilt axis and the slices can be reconstructed independently. Then the slices can be concatenated to reconstruct the final 3D volume. Therefore, the method will be described here for single slice of the volume to be reconstructed. The image formation geometry is presented in Fig. 1. The parameter estimation can be realized for each slice independently by MAPEM method which maximizes a posteriori probability distribution using the Baye's rule as:

$$P(Img|Data) = P(Data|Img)P(Img)/P(Data) \tag{3}$$

$P(Data|Img)$ is the likelihood of the measured data to be observed given the image to be reconstructed. $P(Img)$ and $P(Data)$ are the a priori probability distributions. $P(Data)$ can be assumed to be constant and excluded from the expression. In ET, very low dose of electrons is applied to a very thin sample in order to prevent radiation damage to the biological sample. Considering the characteristics of the signal and the noise, Poisson distribution can be assumed to represent the measurements. This assumption can be extended to model the number of electrons blocked by each pixel

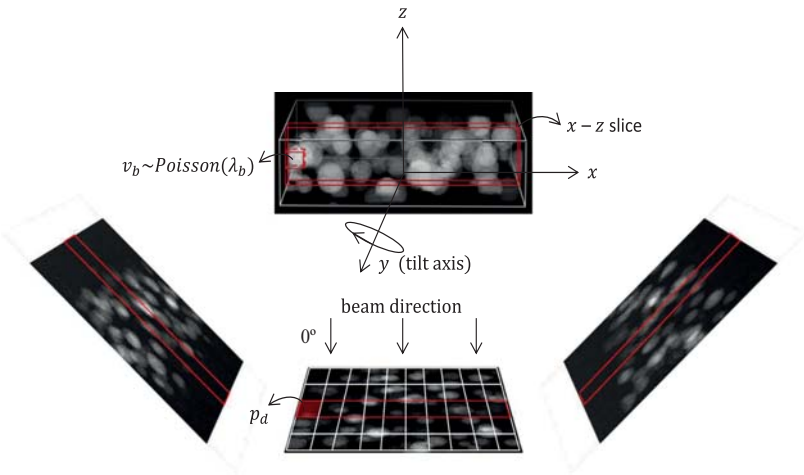

Fig. 1. The projection geometry. The volume is divided into *x*–*z* slices which are reconstructed independently. v_b is proportional to the probability that an incident electron is scattered inside the *b*th pixel of the *x*–*z* slice image. It is modeled by a Poisson distribution with mean λ_b. p_d is the *d*th projection data.

of the image. The statistical chain from generation of the electrons, via the scattering events inside the specimen, to the measurement detector, is assumed to be a cascaded Poisson process. This assumption is useful to satisfy the positivity constraint throughout the iterations. It was also utilized in the development of the adaptive regularization method described below (in Section 2.2). Using Poisson distribution and (2), the likelihood of observing the projection data, $\boldsymbol{p}$, conditioned on the mean values λ ($P(Data|Img)$) can be expressed as:

$$L(\boldsymbol{p}|\lambda) = \prod_{db} exp(-\lambda_b a_{db} \frac{(\lambda_b a_{db})^{v_b a_{db}}}{(v_b a_{db})!}) \tag{4}$$

where λ_b is the parameter of the Poisson distribution describing v_b. By taking the logarithm and derivative of this expression with respect to λ_b and equating it to zero, the maximum likelihood can be obtained as:

$$\hat{\lambda}_b = \frac{\sum_d v_b a_{db}}{\sum_d a_{db}} \tag{5}$$

Since $v_b a_{db}$ is unavailable, it will be replaced by its conditional expected value at each iteration of the expectation maximization algorithm. The expected value can be calculated as:

$$E\left[v_b a_{db} | p_d, \lambda_b^k a_{db} \right] = p_d \frac{\lambda_b^k a_{db}}{\sum_{b'} \lambda_{b'}^k a_{db'}}. \tag{6}$$

where b' is the pixel index of the image to be reconstructed. Using the expected value of $v_b a_{db}$ in (4), the maximum likelihood estimate of λ can be expressed iteratively as follows.

$$\lambda_b^{k+1} = \frac{\lambda_b^k}{\sum_d a_{db}} \sum_d \frac{p_d a_{db}}{\sum_{b'} \lambda_{b'}^k a_{db'}} = \lambda_b^k C_b^{Lk}. \tag{7}$$

In addition to the likelihood term, $C_b^{L\langle k\rangle}$, MAPEM reconstruction involves a regularization term, $C_b^{P\langle k\rangle}$, that represents $P(Img)$. The overall update equation of the MAPEM is

$$\lambda_b^{k+1} = \lambda_b^k C_b^{Lk} C_b^{Pk}. \tag{8}$$

For $P(Img)$, local similarity in the small neighborhood of each pixel of the reconstructed image is a common choice. With Median Root Prior (MRP) [11], the regularization term is expressed as:

$$C_b^{P\langle k\rangle} = \left(1 + \beta \left(\frac{\lambda_b^{\langle k\rangle} - med(\lambda_b^{\langle k\rangle})}{med(\lambda_b^{\langle k\rangle})} \right) \right)^{-1} \tag{9}$$

where *med*() operator represents the median filtering and β is the regularization parameter which controls the strength of this penalization filter.

2.1. Sequential MAPEM reconstruction method

Sequential maximum *a posteriori* expectation maximization (sMAPEM), was introduced to ET recently to compensate for the missing wedge effects [12,13]. The method assumes Poisson distribution to model the image to be reconstructed and median filter (median root prior, [11]) to regularize the iterations. Instead of using one constant regularization parameter value, the method used a sequence of these in the decreasing order. At each regularization stage, predefined number of iterations was performed with constant regularization parameter value. The initial stages with high values of regularization parameters provided a rough but robust estimate of the image for the following stages by highly suppressing the noise. The regularization parameter value was decreased to enhance the resolution and contrast of the final reconstructed image. This sequential method was consistently superior to the conventional reconstruction methods, weighted back-projection (WBP) and a simultaneous iterative reconstruction technique (SIRT), in terms of accuracy and noise suppression due to its capability of filling the missing wedge [12]. However, sMAPEM has some parameters, which affect the final resolution, the final contrast, and the visual impression of the reconstruction result. The number of regularization stages, the number of iterations

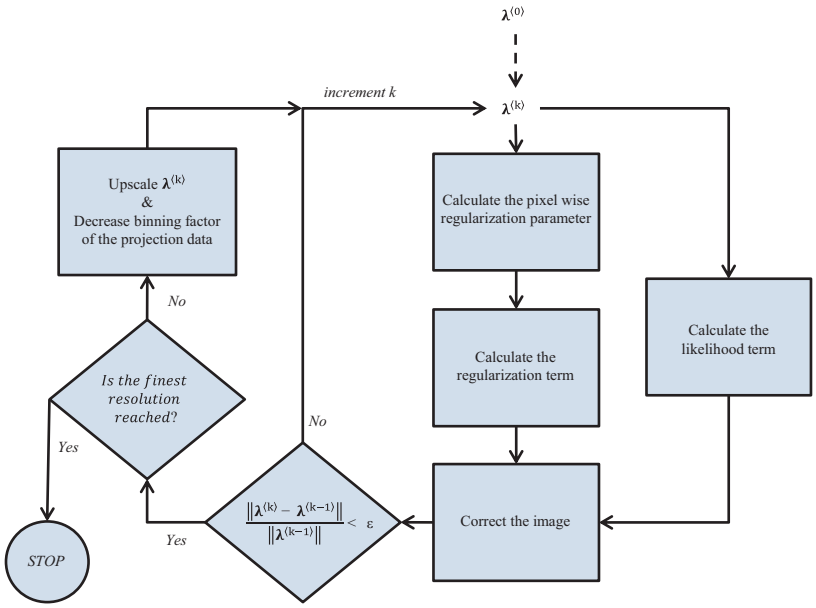

Fig. 2. The flow diagram of the amMAPEM reconstruction method. $\boldsymbol{\lambda}^{\langle k\rangle}$ is the image at kth iteration. The method is initialized with a uniform image of positive values. The number of binned pixels is quartered and the number of binned radial projection samples is halved at the end of each resolution stage. The resulting image of each stage initialized the next one after rescaling the image size and the intensity range. The final image is reconstructed at the last stage using the original projection data.

per each stage, and the regularization parameters need to be set properly by the user according to the data and the application. Moreover, the method requires a long computation time.

2.2. Adaptive regularization

MAPEM methods maximize the likelihood of observing the measured projections subject to the prior knowledge. During this maximization, noise in the projection data makes the pixels with high variance of intensity values vary around their expected values more than the ones with low variance. It would be wise to adjust the regularization parameter pixel-wise considering the amount of local variance. This way, the prior information can be used more strongly for the pixels with high variance of intensity values than the ones with low variance of intensity values.

The intensity values of the pixels at each iteration correspond to the mean values of the Poisson distributions. For Poisson distribution, the variance of the distribution is equal to its mean value. Therefore, the intensity values at each iteration, $\lambda_b^{\langle k\rangle}$, can be used as a measure of variance and so for the regularization strength. For the positivity constraint of the pixels, the regularization parameter, β, needs to be in the range [0,1]. Therefore, the intensity values were normalized considering this range at each iteration and used as the pixel-wise regularization parameter in this study. Hence, the adaptive regularization term can be expressed as:

$$C_b^{P\langle k\rangle} = \left(1+\beta_b^{\langle k\rangle}\left(\frac{\lambda_b^{\langle k\rangle} - med(\lambda_b^{\langle k\rangle})}{med(\lambda_b^{\langle k\rangle})}\right)\right)^{-1} \tag{10}$$

where

$$\beta_b^{\langle k\rangle} = \frac{\lambda_b^{\langle k\rangle}}{\max_b \lambda_b^{\langle k\rangle}} \tag{11}$$

The likelihood term, $C_b^{L\langle k\rangle}$, and the overall update equation are the same as in (6) and (7), respectively. Note that, we assign a different regularization parameter to each pixel at each iteration instead of using a constant regularization parameter for the whole image.

2.3. Adaptive multiresolution MAPEM reconstruction method

The strength of the penalization depends on the regularization parameter value and the filter size relative to the reconstructed image size. sMAPEM method used a sequence of regularization parameter values in the decreasing order to weaken the penalization filter sequentially [12]. In this way, noise was highly suppressed in the reconstruction in the first regularization stages to have coarse but robust estimate of the structure. In the following stages, the regularization parameter value was decreased to enhance the resolution and contrast of the estimate. In addition to changing the regularization parameter value adaptively to control the noise penalization, adaptive multiresolution MAPEM (amMAPEM) reconstruction method changes the reconstruction image size while keeping the filter size constant. In our experiments, we fixed the window size of the filter to its smallest value (3×3) in order to minimize the loss of resolution due to filtering (The reader may refer to [11] for the effect of different filter sizes on MRP regularization). The same size of filter affects the small size image more strongly than the large one. With amMAPEM method, the strength of the penalization filter is weakened by increasing the image size stage by stage sequentially. The advantage of this approach is its computational efficiency.

The flow diagram of the amMAPEM method is given in Fig. 2 for single x–z slice of the reconstructed volume. The method is initialized with a uniform image of size 4×4 so that

3×3 median filter can fit in properly. At each resolution stage, adaptive regularization is applied using the binned projection data and rescaled reconstruction grid. The result of each regularization stage is scaled up by a factor of 2 using bilinear interpolation. The scaled image initializes the following regularization stage. The binning factor of the projection data is also decreased throughout the stages. With this method, the averaging effect of binning operation decreases the noise contamination together with the median filter employed inside the iterations of adaptive regularization. Decreasing the number of binned pixels step by step improves the resolution of the reconstruction. The final image is obtained at the last stage using the result of previous stages and the original projection data P.

The method is implemented in MATLAB (MathWorks Inc., MA, USA) and the code is available together with the data related to this study at http://www.cs.tut.fi/sgn/m2obsi/m2obsiWWW/demos/amMAPEM/amMAPEM.html.

2.4. Stopping rule

The iterations for each resolution stage of amMAPEM were stopped when the difference between two consecutive images throughout the iterations was insignificant. The difference was measured by normalized mean squared error (NMSE) and the level of significance was determined to be 10^{-7} experimentally. The NMSE values are calculated as:

$$NMSE^{\langle k \rangle} = \frac{\sum_b (\lambda_b^{\langle k \rangle} - \lambda_b^{\langle k-1 \rangle})^2}{\sum_b (\lambda_b^{\langle k-1 \rangle})^2} \tag{12}$$

3. Materials

3.1. Datasets

3.1.1. Numerical phantom dataset

A $256 \times 256 \times 64$ nm^3 simulated numerical phantom was generated in MATLAB for the evaluation of the methods. It is composed of about 25 spherical objects located additively in the volume. 25 hollow spheres were also added to the phantom to simulate vesicles. The intensity levels and diameters of the objects were determined randomly following a uniform distribution in the range [0 1] and [19,42] nm, respectively. The projection images were calculated with 1° angular step in the range $\pm 60°$. The images were generated at a pixel size of 1 nm $\times$ 1 nm. Two types of noise were added to the projection data (1) Poisson noise to simulate the randomness in the counting process of transmitted electrons and (2) Gaussian noise to simulate the variations at the detector level. Three noise levels were simulated to have SNRs (ratio of the signal and the noise variances) of 50, 10, and 1. The zero tilt images of the dataset are presented in Fig. 3.

3.1.2. CCDB-P2005 dataset

The experimental dataset consists of a freeze-substituted VeroE6 cultured cell infected with the SARS-CoV (The Cell Centered Database, project P2005, microscopy product 6021, [14,15]). It includes 131 TEM images acquired with a 1° angular step at the range $[-65°, +65°]$ using single tilt projection geometry. The images were collected at 80 kV with a Philips CM-10 transmission electron microscope (Philips, The Netherlands). Spherical gold particles with diameter 10 nm were applied to the surface of the specimen to serve as fiducial markers to align the tilt series. The original images with size 2048×2048 were cropped to 1024×1024 pixels for computational simplicity. The pixel size was 1.2 nm. The zero tilt image of the dataset is presented in Fig. 3d.

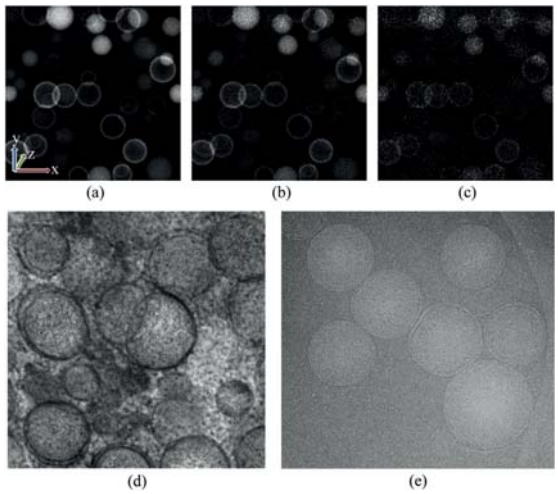

Fig. 3. Zero tilt projection images of the datasets used in the experiments. (a), (b) and (c) show the phantom dataset images at SNR 50, 10 and 1, respectively. (d) and (e) are images from the experimental datasets CCDB-P2005 and EMPIAR-10048, respectively.

3.1.3. EMPIAR-10048 dataset

The experimental dataset is comprised of a single axis tilt series of chlamydia trachomatis type III secretion systems in contact with a HeLa cell [16,17]. It contains 36 cryoEM images collected in 3° increments at the range $[-60°, +45°]$. The dataset also includes spherical gold particles with diameter 10 nm. The alignment and CTF correction of the projection images were realized in IMOD [18]. The raw projection image size was 3708×3838 pixels. 2×2 binning and cropping were applied to the images after the alignment and CTF correction process. The resulting image size was 1369×1448 and the pixel size was 1.08 nm. The zero tilt image of the dataset is presented in Fig. 3e.

3.2. Evaluation criteria

3.2.1. Mean squared error

In order to have a general assessment of the overall image quality, the mean squared error (MSE) between the reconstruction result and the ground truth was calculated as:

$$MSE = \frac{1}{N} \sum_i \left(I_{gt}(i) - I(i) \right)^2, \tag{13}$$

N is the number of voxels, I_{gt} is the ground truth and I is the reconstructed volume.

3.2.2. Fourier shell correlation

Fourier shell correlation (FSC) is the normalized cross-correlation coefficient between two 3D volumes calculated over shells in Fourier space [19]. It can be calculated using the ground truth and the reconstructed volume as:

$$FSC(r) = \frac{\sum_{r_i \in r} F_{gt}(r_i).\, F(r_i)^*}{\sqrt{\sum_{r_i \in r} |F_{gt}(r_i)|^2 \cdot \sum_{r_i \in r} |F(r_i)|^2}} \tag{14}$$

where F_{gt} and F are the Fourier transforms of the ground truth and the reconstructed volume, respectively. r_i is the ith voxel at

radius r. FSC expresses the correlation between two volumes with respect to spatial frequency. The cutoff frequency providing correlation higher than a certain threshold value is used as a measure of resolution in the field of electron microscopy.

4. Results

In order to evaluate the contribution of adaptive multi-resolution method to the reconstruction process, the evaluation results were compared with sMAPEM, and the conventional methods, WBP and SIRT [20]. sMAPEM reconstructions were performed using the recommended parameters. In WBP reconstructions, a ramp filter and a Hamming filter with cutoff frequency 0.5 cycles/pixel were used. 50 iterations were used for the SIRT reconstructions. Positivity constraint was applied for WBP and SIRT reconstructions. All the methods were implemented in MATLAB.

4.1. Numerical phantom reconstructions

The MSE values calculated between the reconstruction results and the ground truth are presented in Table 1 for different noise levels. The MSE value of amMAPEM was lower than the WBP, SIRT and sMAPEM values on average. The values for different noise levels show that amMAPEM is more robust against noise than sMAPEM. The increasing noise results in bigger increase in MSE for sMAPEM than for amMAPEM.

We also calculated Fourier shell correlation (FSC) between the reconstructed images and the ground truth to evaluate the images for their capability of resolving the details. The FSC curves are shown in Fig. 4. The correlation values get close to 1 as the reconstruction result gets close to the ground truth. It is seen in the figure that the correlation values with respect to spatial frequencies are clearly higher for sMAPEM and amMAPEM than for WBP, SIRT. The correlation with the ground truth decreases with the increasing noise. The decrease is bigger for sMAPEM compared to amMAPEM. This shows amMAPEM can handle noise variations better than sMAPEM.

Table 1
MSE analysis of the resulting numerical phantom images for different reconstruction methods and noise levels. The MSE values are scaled by 10^{-3}.

Reconstruction method	MSE (SNR 50)	MSE (SNR 10)	MSE (SNR 1)	Average MSE
WBP	2.70	3.00	6.16	3.95
SIRT	4.60	4.56	5.79	4.98
sMAPEM	0.82	1.69	6.17	2.89
amMAPEM	0.87	1.21	2.92	1.67

The visual assessment of the reconstruction results is in line with the numerical evaluations. The resulting images of the reconstructions for the highest (SNR 1) and lowest (SNR 50) noise levels are given in Fig. 5. The missing wedge artifacts are clearly visible in WBP and SIRT reconstruction results. The spherical objects are elongated in z direction and the elongated objects create artificial objects in the x–y slices. It is also seen that hollow spheres are deformed and look open in the in the WBP and SIRT reconstruction results because of the missing wedge. However, these missing wedge effects are compensated better in sMAPEM and amMAPEM reconstructions.

Fig. 5 also shows that the noise suppression capability of the amMAPEM method with the adaptively selected parameters is better than that of the sMAPEM method. The effect of noise is visible inside the smooth regions of the spherical objects. The results also show that the amMAPEM method can preserve the edges while suppressing the noise. It is clear in the images that the smooth regions are smoother with amMAPEM than with sMAPEM while the boundaries are still sharp. Fig. 6 shows the line profiles of a circular object in z direction. WBP and SIRT profiles are wider than the ground truth profile while the sMAPEM and amMAPEM profiles show edges as sharp as the ground truth. Both sMAPEM and amMAPEM can keep the object boundaries quite close to the ground truth. The major difference between the profiles of these two methods is seen in the plateau with the high intensity values. amMAPEM profile is flatter than sMAPEM profile in this region for all noise levels due to the adaptive regularization.

4.2. CCDB-P2005 dataset reconstructions

The slice images taken from the reconstruction results for different methods are analyzed in Fig. 7. The zoomed-up views of the gold particle show the elongation effect in z direction due to the missing wedge. The spherical shape of the gold particle is highly distorted in WBP and SIRT reconstruction results. However, it is still close to its original spherical shape in the sMAPEM and amMAPEM reconstructions. In Fig. 8, the gold particle images are analyzed in more detail using line profiles taken through the center of the particle shown in Fig. 7. The profiles taken in the x and z directions show that the edges of the sMAPEM and amMAPEM profiles are sharper than the WBP and SIRT profiles. The plateau with the high intensity values is supposed to be flat because of the homogeneity of the gold particle. This region is flatter

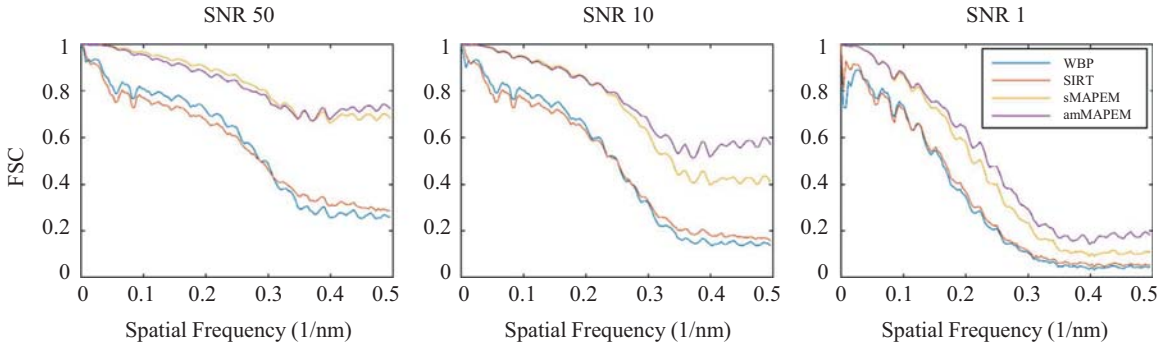

Fig. 4. FSC analysis of the reconstruction results for different noise levels. The correlation values are clearly higher for sMAPEM and amMAPEM than for WBP, SIRT. The correlation values decrease with the increasing noise. The decrease is bigger for sMAPEM compared to amMAPEM. This shows amMAPEM can handle noise variations better than sMAPEM.

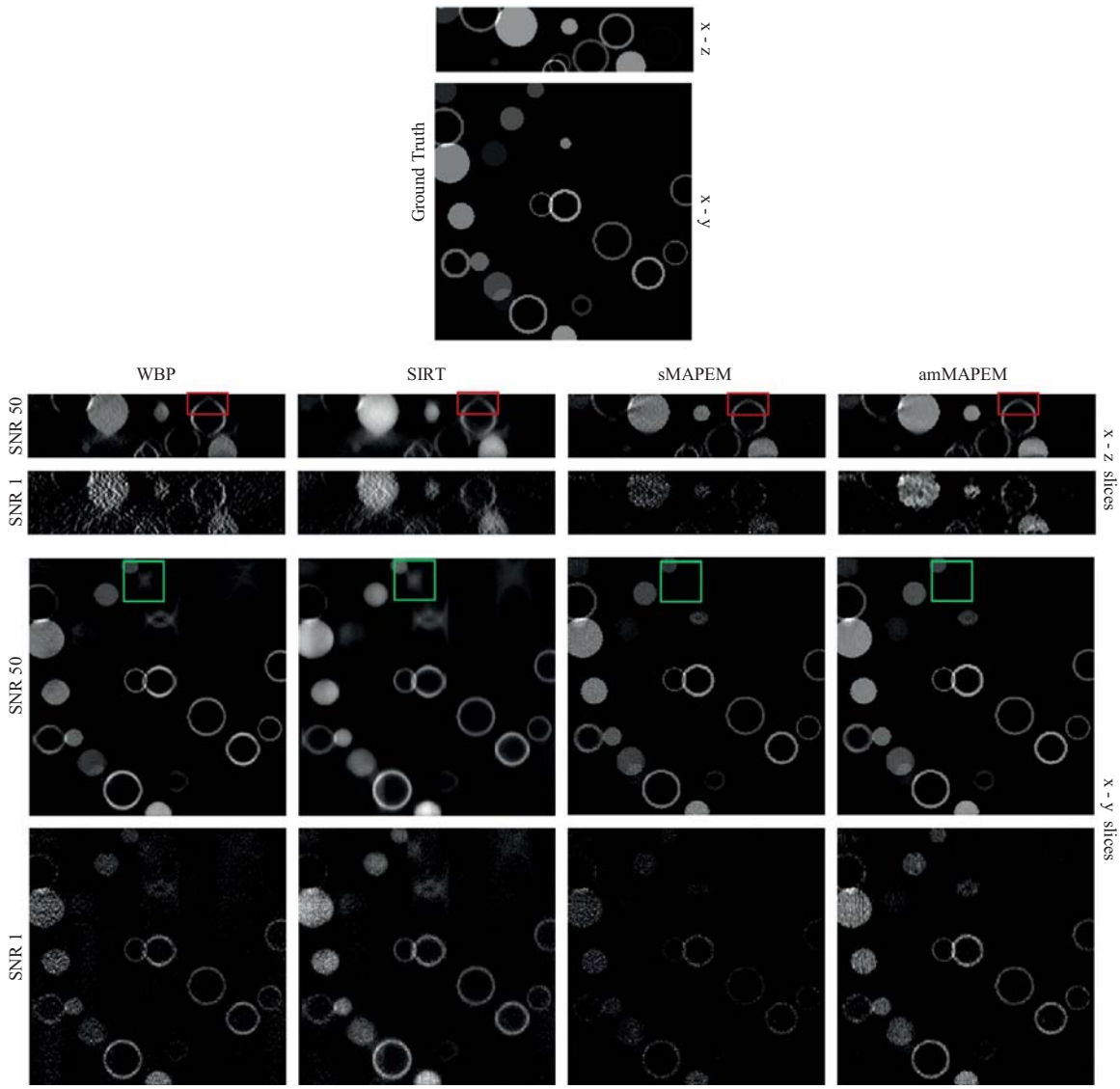

Fig. 5. Resulting *x–y* and *x–z* slice images of the numerical phantom reconstructions for SNR 50 and SNR 1. The ground truth image is given at the top. The hollow spheres look deformed in the in the WBP and SIRT reconstruction results (red rectangles). However, their circular shape and connectedness are preserved better in sMAPEM and amMAPEM images. The objects elongated in *z* direction create artificial objects in *x–y* planes (green rectangles). These artifacts do not appear on the sMAPEM and amMAPEM images. The sMAPEM images have noisier impression than amMAPEM images. (For interpretation of the references to color in this figure legend, the reader is referred to the web version of this article.)

for amMAPEM compared with sMAPEM.

The gold particles in the reconstructed volumes were also analyzed quantitatively. For that purpose, randomly selected 5 gold particles were isolated and compared in terms of FSC with the ground truth generated using the known size of the gold particles. The *x–z* and *x–y* projection images for three of these gold particles are presented in Fig. 9. The average of 5 FSC curves is presented in the figure. The images and the FSC curve show that sMAPEM and amMAPEM methods provide more accurate results with less elongation artifacts compared to WBP and SIRT.

4.3. EMPIAR-10048 dataset reconstructions

The slice images taken from the reconstruction results are presented in Fig. 10. The WBP images are noisier than the other images. The boundary of the circular object is preserved better in amMAPEM image compared to the other results. The quantitative analysis of the reconstructed volumes was performed using the gold particles as it was done for the CCDB-P2005 dataset. The *x–z* and *x–y* projection images for three of the isolated gold particles are presented in Fig. 11. The average of FSC curves calculated using

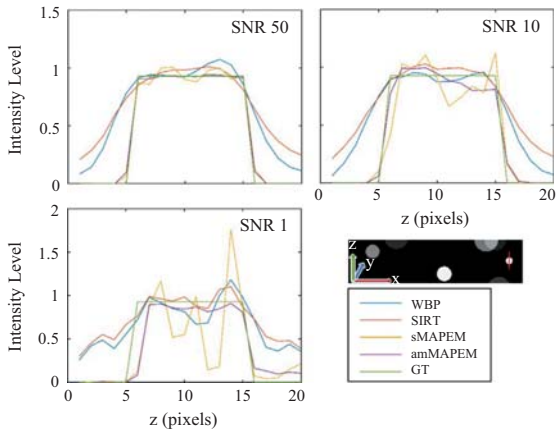

Fig. 6. Line profiles for different reconstruction results with respect to the ground truth (GT). The location of the profiles is shown with red line on the downright ground truth image. The edges of the sMAPEM and amMAPEM profiles are as sharp as the ground truth however edges of the WBP and SIRT profiles are wider. The plateau with the high intensity values is flatter for amMAPEM compared with sMAPEM showing amMAPEM's superiority on handling noise level variations.

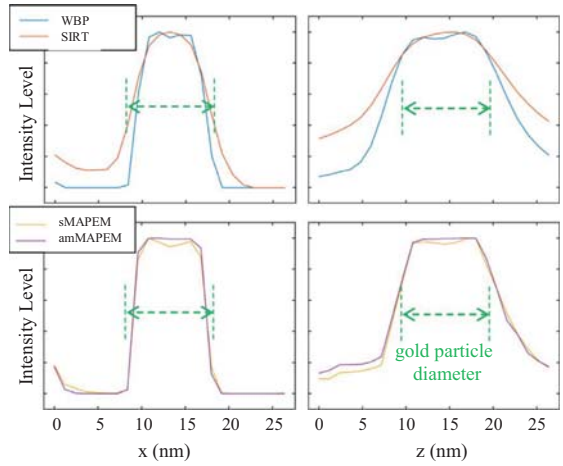

Fig. 8. Line profiles taken through the center of the gold particle shown in Fig. 7 for different reconstruction results. The profiles taken in the *x* and *z* directions are shown on the left and right, respectively. The edges of the sMAPEM and amMAPEM profiles are sharper than the WBP and SIRT profiles. The plateau with the high intensity values is flatter for amMAPEM compared with sMAPEM due to adaptive regularization.

5 randomly selected gold particles is presented in the figure. The images and the FSC curve show that sMAPEM and amMAPEM results are closer to the ground truth compared with the WBP and SIRT results. It is also seen that sMAPEM images are noisier than amMAPEM images.

4.4. Computational analysis

The datasets were divided into *x*–*z* slices and the slices were reconstructed independently. WBP and SIRT slices were reconstructed one by one using a desktop PC. For amMAPEM and

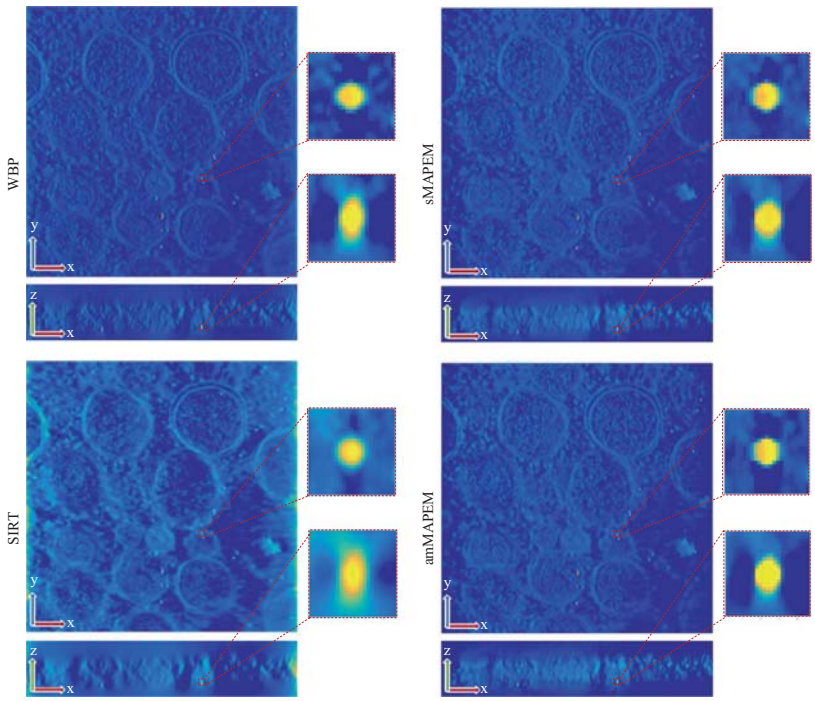

Fig. 7. The slice images taken from the *x*–*y* and *x*–*z* planes of the experimental datasets CCDB-P2005 reconstruction results. The zoomed-up views of a gold particle are given on the right of each slice image. The gold particle images are elongated in *z* direction due to the missing wedge. This missing wedge artifact is less visible in sMAPEM and amMAPEM reconstructions compared with WBP and SIRT reconstruction results.

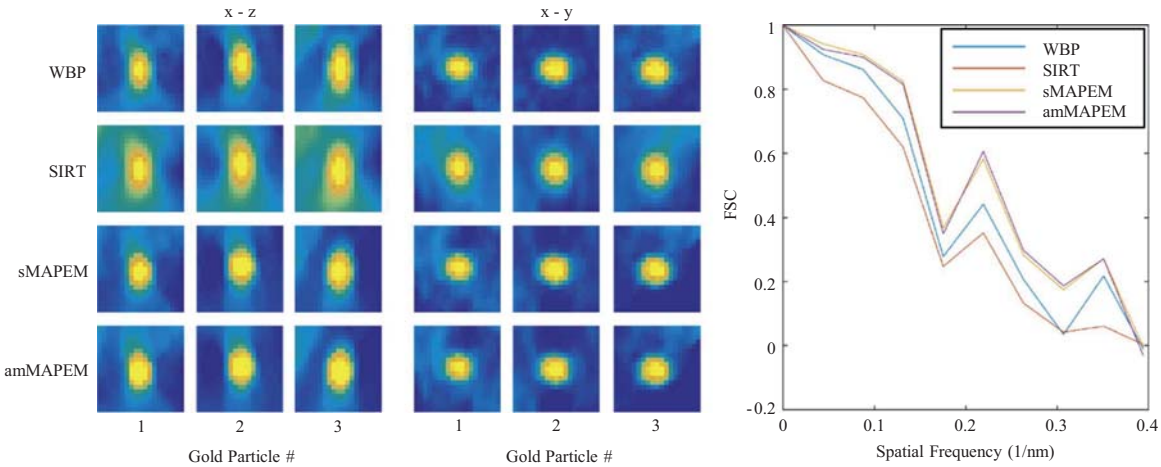

Fig. 9. The gold particle based analysis of the experimental data CCDB-P2005 reconstruction results. The x–z and x–y projection images of three isolated gold particles are presented on the left. The average FSC curves calculated between the reconstruction results and the gold particle ground truth is presented on the right. sMAPEM and amMAPEM methods provide more accurate reconstruction results with less elongation artifacts compared to WBP and SIRT.

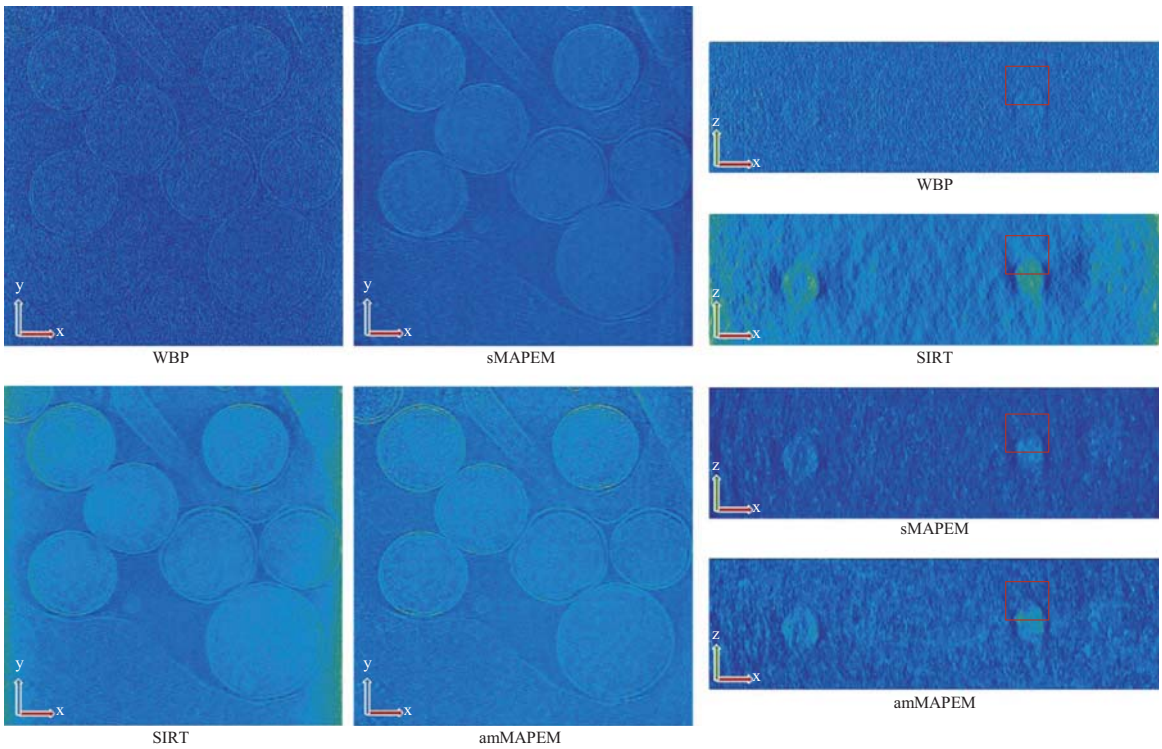

Fig. 10. The slice images taken from the *x–y* and *x–z* planes of the experimental data EMPIAR-10048 reconstruction results. 2×2 binning were applied to the images for better visual impression. The WBP images look noisier than the other images. The boundary of the circular object shown by red rectangle is more clear in amMAPEM image compared to the other results.

sMAPEM, a grid of computers with various configurations was utilized to reconstruct the slices in parallel. In order to compare the computational efficiencies of the reconstruction methods, we measured single slice computation times for each method. The computations were performed using MATLAB on an Intel(R) Core (TM) i5@3.20 GHz desktop computer with Windows 64 bit operating system. The computation times are presented in Table 2. The computation time for amMAPEM increases with the increasing noise. The computation times of the other methods are same for all noise levels since they use fixed parameter settings. amMAPEM

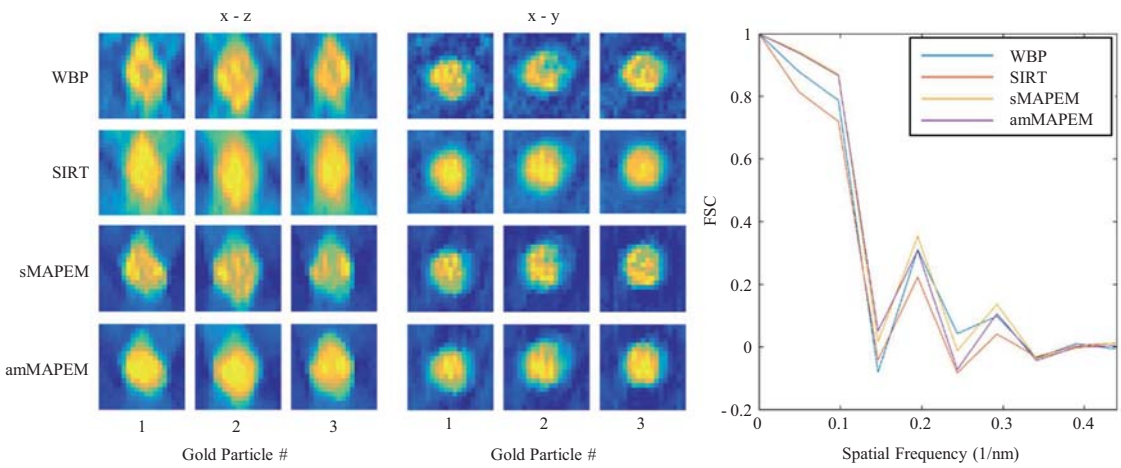

Fig. 11. The gold particle based analysis of the experimental data EMPIAR-10048 reconstruction results. The *x–z* and *x–y* projection images of three isolated gold particles are presented on the left. The average FSC curves calculated between the reconstruction results and the gold particle ground truth is presented on the right. sMAPEM and amMAPEM methods provide more accurate reconstruction results with less elongation artifacts compared to WBP and SIRT. sMAPEM images look noisier than amMAPEM images.

Table 2
The computation times for different reconstruction methods.

Method	Computation time (s)		
	Phantom data	Experimental data CCDB-P2005	Experimental data EMPIAR-10048
WBP	0.15	4.8	2.68
SIRT	11	321	177
sMAPEM	1360	17,804	12,228
amMAPEM	245 (SNR 50) 289 (SNR 10) 612 (SNR 1)	3361	2972

was significantly faster than the sMAPEM method. Although the WBP and SIRT computation times were shorter than those of sMAPEM and amMAPEM, the visual quality and accuracy of these reconstructions were much worse than sMAPEM and amMAPEM.

5. Discussion

The present research demonstrates that the proposed amMAPEM method can reconstruct 3D ET images more accurately than the conventional reconstruction methods, WBP and SIRT, significantly suppressing the missing wedge artifacts. It also provides images with better quality than with sMAPEM in shorter time without requiring special effort for parameter setting. The proposed adaptive regularization method extracts all necessary information simultaneously from the reconstructed image throughout the iterations. Instead of using a single regularization parameter for the whole image, it updates the regularization parameter pixel-wise according to the local noise contamination. This way, we calculate the regularization strength adaptively.

The major advantage of sMAP-EM and amMAPEM methods is their gap filling ability. The methods provide a compensation for the missing angular gap in the frequency domain by using the prior information of local smoothness. The gap filling ability arises from the MRP regularization. The median filter used throughout the iterations acts as an interpolator in the frequency domain. The information source for the interpolation is the relation of the pixel values in the local neighborhood. The filter preserves the edges in the spatial domain while using this information. The reader may refer to the previous studies for the detailed analysis of gap filling capability of sMAPEM in comparison with the conventional reconstruction methods [12,13]. One of the major drawbacks of sMAPEM is that it requires a large number of iterations for gap filling. We overcome this computation time problem with amMAPEM method by employing multiresolution reconstruction.

The amMAPEM method uses the intensity values, which represent the mean of the Poisson model used for each pixel, as a measure of noise contamination since the variance of a Poisson distribution equals its mean. With Poisson model, it was possible to characterize the distribution by a single positive parameter. This provided positivity constraint to be satisfied implicitly for the reconstruction in addition to simplicity of the solution.

The usability of the iterative reconstruction methods in electron tomography highly depend on their computation time. The opportunities provided by the modern computing technology (e.g. GPU [21], SIMD extensions of the modern processors [22]) can be utilized to improve the performance of the methods. We used the computer grid Techila (Techila Technologies Ltd., Tampere, Finland) for the reconstruction of the experimental data in this study. However, methodological improvements still play an important role in accelerating the image reconstruction besides these improvements in the software implementation level.

Ordered subsets (OS) is one method to decrease the computation time in tomographic image reconstruction [23]. The method divides the projection data into predefined number of subsets and updates the reconstructed image for each subset during the iterations. Since there is a large block of information gap and SNR is low in ET, updating the image using even sparser subsets of projection data can exaggerate noise throughout the iterations. Therefore, we utilized the multiresolution approach instead of OS to reduce the computation time. It was shown with the phantom and experimental datasets that the computation time is much shorter for amMAPEM than for sMAPEM. The multiresolution reconstruction also contributed to the visual quality of the reconstruction results in addition to computation time acceleration. Its averaging effect and usage together with the median filter suppressed noise throughout the iterations. Each regularization

stage (except the first one) is initialized with a coarser estimate of the image. Starting with this coarser estimate of the image to be reconstructed instead of a random or uniform one improved the reconstruction result.

The MAP reconstruction method presented in this paper provides a successful solution to compensate for the missing wedge artifacts and noise in electron tomography. Since the method does not require any parameter setting and it has improved computational efficiency, it can be widely used in the field of electron microscopy.

Acknowledgments

This work was supported by Tekes FiDiPro (1913/31/2012). The experimental dataset was provided by The Cell Centered Database which is supported by NIH Grants from NCRR RR04050, RR RR08605 and the Human Brain Project DA016602 from the National Institute on Drug Abuse, the National Institute of Biomedical Imaging and Bioengineering and the National Institute of Mental Health.

References

[1] P. Hansen, Rank-deficient and discrete ill-posed problems: numerical aspects of linear inversion, Soc. Ind. Appl. Math. (1998).
[2] K. Hämäläinen, A. Kallonen, V. Kolehmainen, M. Lassas, K. Niinimäki, S. Siltanen, Sparse tomography, SIAM J. Sci. Comput. 35 (3) (2013) B644–B665.
[3] K. Niinimäki, M. Lassas, K. Hämäläinen, A. Kallonen, V. Kolehmainen, E. Niemi, S. Siltanen, Multi-resolution parameter choice method for total variation regularized tomography, ArXiv e-prints, 2014.
[4] Y.-W. Wen, R.H. Chan, Parameter selection for total-variation-based image restoration using discrepancy principle, IEEE Trans. Image Process. 21 (4) (2012) 1770–1781.
[5] M.V. Ranganath, A.P. Dhawan, N. Mullani, A multigrid expectation maximization reconstruction algorithm for positron emission tomography, IEEE Trans. Med. Imaging 7 (4) (1988) 273–278.
[6] A. Raheja, A.P. Dhawan, Multiresolution expectation maximization reconstruction algorithm for positron emission tomography using wavelet processing, in: Proceedings of the 20th Annual International Conference of the IEEE Engineering in Medicine and Biology Society, 1998, vol. 2, pp. 759–762.
[7] S.V. Venkatakrishnan, L.F. Drummy, M.A. Jackson, M. De Graef, J. Simmons, C. A. Bouman, A model based iterative reconstruction algorithm for high angle annular dark field-scanning transmission electron microscope (HAADF-STEM) tomography, IEEE Trans. Image Process. 22 (11) (2013) 4532–4544.
[8] A. Dabravolski, K.J. Batenburg, J. Sijbers, A multiresolution approach to discrete tomography using DART, PLoS One 9 (9) (2014) e106090.
[9] O. Öktem, Handbook of Mathematical Methods in Imaging, in: O. Scherzer (Ed.), Springer, New York, NY, 2015, pp. 937–1031.
[10] B. Fultz, J.M. Howe, Transmission Electron Microscopy and Diffractometry of Materials, Springer, Berlin, Heidelberg, 2008.
[11] A. Alenius, U. Ruotsalainen, Generalization of median root prior reconstruction, IEEE Trans. Med. Imaging 21 (11) (2002) 1413–1420.
[12] L. Paavolainen, E. Acar, U. Tuna, S. Peltonen, T. Moriya, P. Soonsawad, V. Marjomäki, R.H. Cheng, U. Ruotsalainen, "Compensation of missing wedge effects with sequential statistical reconstruction in electron tomography, PLoS One 9 (10) (2014) e108978.
[13] T. Moriya, E. Acar, R.H. Cheng, U. Ruotsalainen, A Bayesian approach for suppression of limited angular sampling artifacts in single particle 3D reconstruction, J. Struct. Biol. 191 (3) (2015) 318–331.
[14] M.E. Martone, A. Gupta, M. Wong, X. Qian, G. Sosinsky, B. Ludäscher, M. H. Ellisman, A cell-centered database for electron tomographic data, J. Struct. Biol. 138 (1–2) (2002) 145–155.
[15] K. Knoops, M. Kikkert, S.H.E. van den Worm, J.C. Zevenhoven-Dobbe, Y. van der Meer, A.J. Koster, A.M. Mommaas, E.J. Snijder, SARS-coronavirus replication is supported by a reticulovesicular network of modified endoplasmic reticulum, PLoS Biol. 6 (9) (2008) e226.
[16] A. Iudin, P.K. Korir, J. Salavert-Torres, G.J. Kleywegt, A. Patwardhan, EMPIAR: a public archive for raw electron microscopy image data, Nat. Methods 13 (5) (2016) 387–388.
[17] A. Nans, M. Kudryashev, H.R. Saibil, R.D. Hayward, Structure of a bacterial type III secretion system in contact with a host membrane in situ, Nat. Commun. 6 (2015) 10114.
[18] J.R. Kremer, D.N. Mastronarde, J.R. McIntosh, Computer visualization of three-dimensional image data using IMOD, J. Struct. Biol. 116 (1) (1996) 71–76.
[19] M. van Heel, M. Schatz, Fourier shell correlation threshold criteria, J. Struct. Biol. 151 (3) (2005) 250–262.
[20] P.A. Penczek, Fundamentals of three-dimensional reconstruction from projections, Methods Enzymol. 482 (C) (2010) 1–33.
[21] W. Xu, F. Xu, M. Jones, B. Keszthelyi, J. Sedat, D. Agard, K. Mueller, High-performance iterative electron tomography reconstruction with long-object compensation using graphics processing units (GPUs), J. Struct. Biol. 171 (2) (2010) 142–153.
[22] J.I. Agulleiro, E.M. Garzón, I. García, J.J. Fernández, Vectorization with SIMD extensions speeds up reconstruction in electron tomography, J. Struct. Biol. 170 (3) (2010) 570–575.
[23] H.M. Hudson, R.S. Larkin, Accelerated image reconstruction using ordered subsets of projection data, IEEE Trans. Med. Imaging 13 (4) (1994) 601–609.

Publication IV

E. Acar, M. A. Baikoghli, M. Stark, S. Peltonen, U. Ruotsalainen, R. H. Cheng, “Multiresolution MAPEM Method for 3D Reconstruction of Symmetrical Particles in Electron Microscopy”, In: Eskola H., Väisänen O., Viik J., Hyttinen J. (eds) EMBEC & NBC 2017. IFMBE Proceedings, vol 65. Springer, Singapore.

Multiresolution MAPEM Method for 3D Reconstruction of Symmetrical Particles with Electron Microscopy

E. Acar[1], M. A. Baikoghli[2], M. Stark[2], S. Peltonen[1], U. Ruotsalainen[1] and R. H. Cheng[2]

[1]Tampere University of Technology/ Department of Signal Processing, Tampere, Finland
[2]University of California/Department of Molecular and Cellular Biology, Davis, USA

Abstract— **The resolution and accuracy of the 3D images obtained with single particle reconstruction (SPR) highly depend on the number and signal to noise ratio of the particle images. The maximum a posteriori probability expectation maximization (MAPEM) reconstruction methods have been successful in suppressing noise and compensating for the limited angular sampling. This paper presents a multiresolution MAPEM (mMAPEM) method to improve the resolution and accuracy of the 3D images of the symmetrical particles reconstructed using SPR. The method utilizes the median root prior and the symmetry information about the reconstructed structure in the image domain. The method was compared with the conventional Fourier Reconstruction (FR) method using phantom and experimental datasets for different noise levels and projection angle sampling conditions. The numerical and visual assessment of the reconstruction results demonstrate that the mMAPEM method provides more accurate results than FR.**

Keywords— **multiresolution MAPEM reconstruction, electron microscopy, single particle reconstruction, HEV.**

I. Introduction

3D images of viruses play an important role in developing effective vaccines and antivirals. Improving the accuracy and resolution of these images enhances our understanding of the mechanisms of virus assembly and entry to the target cell. Single Particle Reconstruction (SPR) is a common method for obtaining high resolution images of these particles in 3D. In SPR, 2D projection images of the particles randomly oriented inside the specimen are collected with transmission electron microscope (TEM). These highly noisy images of the same particle with different orientations are detected and classified according to their orientations. Then, the average of the particle images constructing each class is calculated to obtain the image representing the class with improved signal to noise ratio (SNR). These class average images are used by the reconstruction methods to obtain the 3D image of the particle from the 2D images with the estimated orientations. The 3D reconstruction and the orientation estimation of the particles can be repeated iteratively to refine the 3D image. The resolution and accuracy of the final image highly depend on the number and signal to noise ratio of the particle images. The aim of this study is to develop a reconstruction method which can compensate for low number and signal to noise ratio of these particle images.

There are several publically available SPR software packages, providing simple and efficient methods for 3D reconstruction [1]. In general, these methods are variants of the back-projection and algebraic 3D reconstruction methods. In the field of tomography, it is reported that back-projection methods are sensitive to the missing information and they can result in severe artifacts due to this information gap [2]. It is also known that algebraic methods do not fill the information gaps [3]. However, it was shown in the recent studies that the statistical reconstruction methods can suppress the artifacts yielded from the missing information and noise without requiring detailed a priori knowledge of the nonsymmetrical objects imaged [4]–[6]. In this study, a multiresolution MAPEM (mMAPEM) method is presented for 3D reconstruction of symmetrical particles in the field of SPR.

II. Method

The projection data acquired with electron microscope can be expressed as:

$$p_d = CTF_d v_d \approx CTF_d \sum_b v_b a_{db}\,; \quad b: 1, \dots, n^3; d: 1, \dots, m^2 ek \tag{1}$$

where v_b represents the probability that an incident electron is scattered inside the b^{th} voxel of the discretized specimen volume. p_d is the d^{th} projection data, a_{db} represents the contribution of the b^{th} voxel to p_d. The CTF_d denotes the influence of the phase-contrast transfer function on the d^{th} projection data. It can be excluded from the equation assuming all the projection images are CTF-corrected. The reconstruction grid is composed of n x n x n voxels and the projection images are m x m pixels. e is the number of asymmetric Euler angles which equals to the number of classes since each class is composed of particle images projected from a single Euler angle. The particle demonstrates a natural $k-fold$ symmetry. Therefore, we have m^2ek observations for n^3 unknowns. The distribution of the asymmetric Euler angles and their symmetric replications are presented in Fig. 1.

H. Eskola et al. (eds.), *EMBEC & NBC 2017*,
IFMBE Proceedings 65,
DOI: 10.1007/978-981-10-5122-7_36

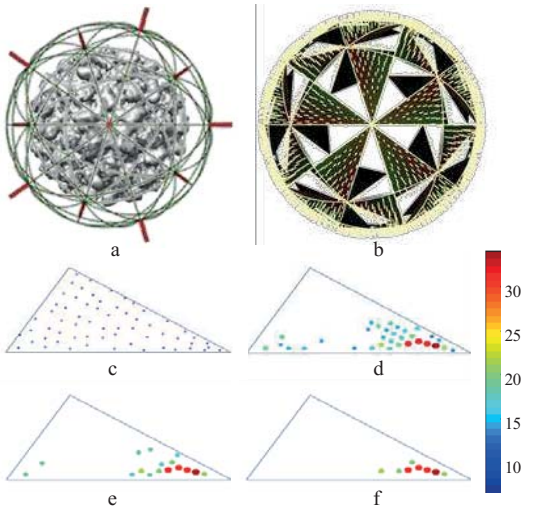

Fig. 1 The distribution of the Euler angles and the icosahedral symmetry. (a) Each red pipe shows an Euler angle of projection for the same particle image. The particle image available for one of these Euler angles can be replicated and back projected from the other angles according to icosahedral symmetry. There is also 5-fold symmetry around the axes passing through the red pipes. (b) The triangles include the asymmetric Euler angles shown by the yellow pipes. The particle images are classified using the Euler angles inside one of the triangles. Then the images are replicated and back projected for the angles inside the other triangles. The distribution of Euler angles inside the asymmetric triangle for the phantom dataset (c) and the experimental dataset for 32 (d), 16 (e), and 8 (f) classes are shown. The color bar shows the number of particle images that each class includes.

The statistical reconstruction methods describe v_b with a distribution model and find the distribution parameters, $\boldsymbol{\lambda}$, which maximize the likelihood of observing p_d based on a priori information if available. Based on the median root prior [7], the iterative update equation of the MAPEM was expressed as [5]:

$$\lambda_b^{\langle k+1\rangle} = \frac{\lambda_b^{\langle k\rangle}}{\sum_d a_{db}} \sum_d \frac{p_d a_{db}}{\sum_{b'} \lambda_{b'}^{\langle k\rangle} a_{db'}} \left(1 + \beta \left(\frac{\lambda_b^{\langle k\rangle} - med(\lambda_b^{\langle k\rangle})}{med(\lambda_b^{\langle k\rangle})}\right)\right)^{-1} \quad (2)$$

where λ_b is the parameter of the Poisson distribution modelling v_b, b' is the voxel index of the volume to be reconstructed, $med()$ operator is the median filtering and β is the regularization parameter to control the weight of this penalization filter. Median filter is used due to its capability of preserving edges.

Multiresolution MAPEM (mMAPEM) reconstructs the volume using a sequence of reconstruction grids with dimensions in the ascending order. Binning is applied to the projection data in parallel with the size of the reconstruction grid.

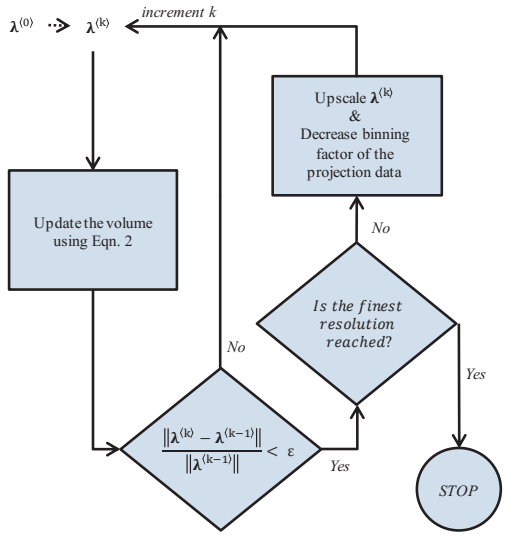

Fig. 2 The flow diagram of the mMAPEM reconstruction method. $\boldsymbol{\lambda}^{\langle k\rangle}$ represents the reconstructed volume at the k[th] iteration, ε is the NMSD threshold.

When the normalized mean squared difference (NMSD) between two consecutive volumes reconstructed during the iterations gets lower than a certain threshold level (ε), the iterations of the current resolution stage are terminated and the next one is initialized with the latest reconstruction result. The binning factor was selected as small and integer valued number, 2, concerning computational cost and change in the image during upscaling between the resolution stages. The window size of the regularization filter is kept constant at 3x3x3 for all resolution stages to minimize the resolution loss at the final reconstruction. Since the reconstruction grid size is increased while the filter size is constant, the weight of the filter decreases throughout the resolution stages. In addition, binning of the projection data reduces noise in the images. This noise suppression effect of binning is also weakened throughout the resolution stages since the binning factor decreases. Due to these factors, strongly filtered projections are used to obtain the 3D structure coarsely in the first regularization stages. Each stage is initialized with the result of the previous one after upscaling. The resolution of the reconstruction is enhanced step by step. The reconstruction yields better results in a shorter time with this multiresolution method because of the reduced noise level during the iterations and the reduced number of voxels in the reconstruction grid [5]. Moreover, initializing each regularization stage with a coarse estimate of the image instead of a random or uniform one contributes to the final image quality. The flow diagram of the mMAPEM method is presented in Fig. 2.

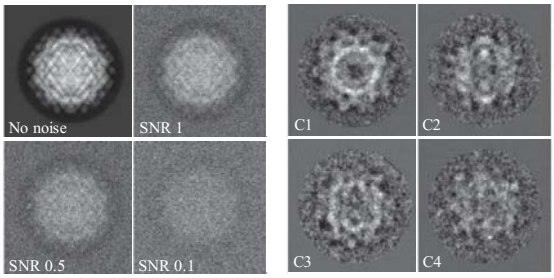

Fig. 3 Input projection images. The images are presented with different noise levels for a single class of the phantom dataset on the left. The class average images for different classes of the experimental dataset are presented on the right. Since each class is composed of different number of images, the SNR values differ from class to class. C1, C2, C3, and C4 are composed of 34, 11, 7, and 6 particle images respectively.

III. Materials

A. Numerical Phantom Dataset

A 3D model of Hepatitis E Virus Like Particle (HEVLP, triangulation number -T = 3) with 182 x 182 x 182 voxels of size of 3.01 Å each was used for the simulations. The projection images of this 3D model were generated and contaminated by mixture of Gaussian and Poisson noise to represent different class average images. The noise also helps avoiding the inverse crime of using the same projector in projection data generation and the image reconstruction. The noise level of the class average images depend on the number and quality of particle images the dataset includes. Therefore, we generated sets of images at different noise levels. The distribution of angles is presented in Fig. 1c. The noise levels were set to the signal to noise ratio (SNR, ratio of signal variance to the noise variance) of 1, 0.5, and 0.1. The generated images with 182x182 pixels are presented in Fig. 3 for a single class of the dataset.

B. Experimental Dataset

The experimental dataset consists of about 1000 cryo EM images of the HEVLP (T=1). The images were classified in EMAN [8]. Then, different sets of class average images were composed to analyze the effect of angular sampling sparsity on the reconstruction results. We used set of 8, 16, and 32 class average images in the experiments. Since the dataset is relatively small, the classes with highest number of particle images are selected while constructing the datasets. The distribution of the Euler angles is presented in Fig. 1d-f. Class average images for 4 different classes are presented in Fig. 3. The input images were 256x256 pixels with pixel size 1.67 Å.

IV. Results and Discussion

The mMAPEM method was compared with the Fourier Reconstruction (FR) method implemented in EMAN2 [9]. The visual and numerical comparison results are presented in Fig. 4 for both phantom and experimental dataset reconstructions. We used central slices for the visual comparison of the reconstructed volumes. For the numerical evaluation, we used Fourier shell correlation (FSC) which is the conventional analysis method in SPR. It calculates the cross-correlation coefficient between two volumes with respect to spatial frequency. It is calculated over shells in the Fourier domain [10]. The FSC curves were calculated between the reconstruction results and the ground truth volume for the phantom dataset. The FSC analysis of the experimental data reconstruction results was realized by dividing the datasets into two partitions as even and odd numbered class average images. Then, the FSC was calculated between the volumes reconstructed using these partitions.

The correlation curves are higher for mMAPEM than for FR consistently for all noise levels of the phantom dataset. The difference between the methods tends to increase as the SNR of the input projection images increases. The SNR of the input projection images depends on the number of particles per each class. If there is sufficiently high number of particle images for each class, mMAPEM can improve the resolution significantly due to its projection gap filling capability. The visual evaluation of the reconstruction results supports the FSC analysis. The images for mMAPEM have less noisy impression than the FR images for all input image noise levels. In comparison with the ground truth, mMAPEM images show details better than the FR images due to noise suppression capability of mMAPEM.

The reconstruction results for the experimental dataset composed of different set of class average images show that mMAPEM provides higher FSC curves than the FR does. The difference between the curves increases with the angular sparsity since mMAPEM can compensate for the missing Euler angles. The visual analysis of the results is in line with the numerical evaluation. Since the images for mMAPEM are less noisy than the FR images, they look sharper compared with the FR images.

The numerical and visual analysis of the reconstructions performed with phantom and experimental datasets demonstrate that the mMAPEM reconstruction method presented in this paper provides an improved reconstruction result for the symmetrical particles even with sparse Euler angle sampling. The method can also be used for reconstruction of nonsymmetrical particles. It can be widely used in the field of SPR to obtain high-resolution images of various particles more accurately with fewer particle images.

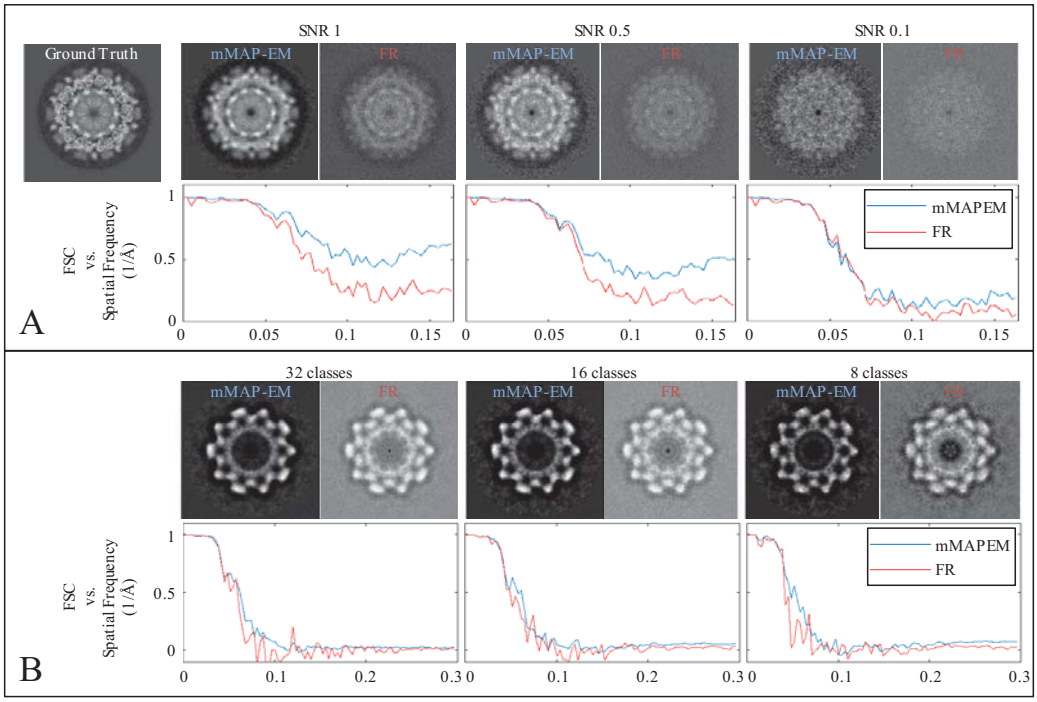

Fig. 4 The analysis of the reconstruction results for the phantom (A) and experimental (B) datasets. The images of the central slices taken from the reconstructed volumes are presented with the FSC curves for noise levels and class average images.

Acknowledgment

This work was supported by Tekes FiDiPro (1913/31/2012).

Conflict of Interest

The authors declare that they have no conflict of interest.

References

[1] "Software Tools For Molecular Microscopy." [Online]. Available: https://en.wikibooks.org/wiki/Software_Tools_For_Molecular_Microscopy.

[2] A. H. Delaney and Y. Bresler, "Globally convergent edge-preserving regularized reconstruction: an application to limited-angle tomography.," *IEEE Trans. Image Process.*, vol. 7, no. 2, pp. 204–21, Jan. 1998.

[3] P. A. Penczek, "Fundamentals of three-dimensional reconstruction from projections.," *Methods Enzymol.*, vol. 482, no. C, pp. 1–33, Jan. 2010.

[4] L. Paavolainen, E. Acar, U. Tuna, S. Peltonen, T. Moriya, P. Soonsawad, V. Marjomäki, R. H. Cheng, and U. Ruotsalainen, "Compensation of missing wedge effects with sequential statistical reconstruction in electron tomography.," *PLoS One*, vol. 9, no. 10, p. e108978, 2014.

[5] E. Acar, S. Peltonen, and U. Ruotsalainen, "Adaptive multiresolution method for MAP reconstruction in electron tomography," *Ultramicroscopy*, vol. 170, pp. 24–34, 2016.

[6] T. Moriya, E. Acar, R. H. Cheng, and U. Ruotsalainen, "A Bayesian approach for suppression of limited angular sampling artifacts in single particle 3D reconstruction.," *J. Struct. Biol.*, vol. 191, no. 3, pp. 318–31, 2015.

[7] S. Alenius and U. Ruotsalainen, "Generalization of median root prior reconstruction.," *IEEE Trans. Med. Imaging*, vol. 21, no. 11, pp. 1413–20, 2002.

[8] S. J. Ludtke, P. R. Baldwin, and W. Chiu, "EMAN: Semiautomated Software for High-Resolution Single-Particle Reconstructions," *J. Struct. Biol.*, vol. 128, no. 1, pp. 82–97, 1999.

[9] G. Tang, L. Peng, P. R. Baldwin, D. S. Mann, W. Jiang, I. Rees, and S. J. Ludtke, "EMAN2: an extensible image processing suite for electron microscopy.," *J. Struct. Biol.*, vol. 157, no. 1, pp. 38–46, Jan. 2007.

[10] M. van Heel and M. Schatz, "Fourier shell correlation threshold criteria.," *J. Struct. Biol.*, vol. 151, no. 3, pp. 250–62, 2005.

The address of the corresponding author:
Author: Erman Acar
Institute: Tampere University of Technology
Street: Korkeakoulunkatu 1
City: Tampere
Country: Finland
Email: ermancr@gmail.com

Publication V

A. Abdollahzadeh*, E. Acar*, S. Peltonen, and U. Ruotsalainen, “Local adaptive wiener filtering for class averaging in single particle reconstruction”, In: Sharma P., Bianchi F. (eds) Image Analysis. SCIA 2017. Lecture Notes in Computer Science, vol 10270. Springer, Cham. (*:equal contribution)

Local Adaptive Wiener Filtering for Class Averaging in Single Particle Reconstruction

Ali Abdollahzadeh[1,2(✉)], Erman Acar[1], Sari Peltonen[1], and Ulla Ruotsalainen[1]

[1] Laboratory of Signal Processing, Tampere University of Technology, P.O.Box 553, 33101 Tampere, Finland
ali.abdollahzadeh@uef.fi
[2] Biomedical Imaging Unit, A.I.Virtanen Institute for Molecular Sciences, University of Eastern Finland, P.O.Box 1627, 70211 Kuopio, Finland

Abstract. In cryo-electron microscopy (cryo-EM), the Wiener filter is the optimal operation – in the least-squares sense – of merging a set of aligned low signal-to-noise ratio (SNR) micrographs to obtain a class average image with higher SNR. However, the condition for the optimal behavior of the Wiener filter is that the signal of interest shows stationary characteristic thoroughly, which cannot always be satisfied. In this paper, we propose substituting the conventional Wiener filter, which encompasses the whole image for denoising, with its local adaptive implementation, which denoises the signal locally. We compare our proposed local adaptive Wiener filter (LA-Wiener filter) with the conventional class averaging method using a simulated dataset and an experimental cryo-EM dataset. The visual and numerical analyses of the results indicate that LA-Wiener filter is superior to the conventional approach in single particle reconstruction (SPR) applications.

Keywords: Electron microscopy · Local adaptive Wiener filter · Class averaging · Single particle reconstruction · Spectral signal-to-noise ratio

1 Introduction

Revealing 3D structures of biomolecular assemblies in their native environment, with sub-nanometer to more recently near-atomic resolution, single particle reconstruction (SPR) is a highly demanded technique in the field of molecular and cellular biology. The technique is especially desired for the structural studies of biomolecules when their crystals are difficult to obtain with sufficient quality for crystallography [1]. SPR uses a collection of cryo-electron microscopy (cryo-EM) images representing the projections of the same particle from different spatial views. The standard procedure is comprised of detecting the particles inside the cryo-EM images, classifying them according to their orientations, averaging the images in each class and reconstructing the particle in 3D. Due to very high radiation sensitivity of the biological specimens and thus low

A. Abdollahzadeh and E. Acar – These authors contributed equally to this work.

P. Sharma and F.M. Bianchi (Eds.): SCIA 2017, Part II, LNCS 10270, pp. 233–244, 2017.
DOI: 10.1007/978-3-319-59129-2_20

maximal allowed electron exposure [2], individual particle images suffer from extremely low signal-to-noise ratio (SNR). In addition, optical characteristic of the microscope that can be summarized in the contrast transfer function (CTF) causes loss of information in the Fourier domain at regular intervals. In order to overcome these problems, large number of images (typically more than 5000) is used in SPR. Therefore, the image processing techniques to classify and merge these images play an important role to reconstruct the particle in 3D with high resolution and accuracy.

The Wiener filter is the optimal estimator of the desired signal from noisy measurements in a stationary Gaussian process by minimizing the mean-squared error [3, 4]. It is used in SPR to obtain class averages with enhanced SNR by merging the images corresponding to the same spatial orientation [5]. The filter utilizes the spectral-SNR (SSNR) of the images in the class averaging process. The ability of the Wiener filter to restore the signal depends on the accuracy of the SSNR estimation. Several studies suggest to replace the SSNR with a constant value in the absence of an accurate SSNR estimate [6, 7]. Alternatively, using other sources of information such as pre-existing low resolution models is another approach to calculate the SSNR [8]. These methods may suffer from bias to the model. Other earlier works for tackling the SSNR problem suggest using the average image as reference to determine the SSNR of each individual image: averaging N micrographs reduces the variance of the noise by a factor of N relative to an individual micrograph, provided that the noise is independent and identically distributed in all images in the set [5]. However, a more recent study demonstrates that the conventional Wiener filter (conv-Wiener filter) fails in the optimal estimation of the particle density itself, as the particle is substantially surrounded by signal-free solvent region in the raw data images. Therefore, the output of conv-Wiener filter is optimal considering the whole image, but not when the particle, i.e. the region of interest, is considered only [9]. Their modified version of the Wiener filter is designed to optimize the signal estimate within a predefined mask region.

In this paper, we present a modified Wiener filter to merge the micrographs and determine the class average images in SPR. Since the optimality of the Wiener filter is based on the assumption that the signal is stationary and the additive noise is Gaussian distributed, violation of this condition reduces the denoising accuracy of the filter. It is easier to satisfy these conditions locally rather than globally as different locations of the experimental EM micrographs may contain diverse distributions. This insight motivated us to alter conv-Wiener filter into a local adaptive one. This filter is extensively used in image/video denoising and it is successful in the sense that it effectively removes noise while preserving important image features such as edges [10]. This definition of the Wiener filter advantages from a sliding window applied throughout the aligned micrograph images to establish a least-squares estimate of the class average. The extraction of the SSNR is implemented based on the average of the projection images. In the next sections, we will formulate the problem and present the qualitative and quantitative evaluation of the proposed method in comparison to the conventional implementation.

2 Materials and Methods

2.1 Datasets

2.1.1 Synthetic Data

Using UCFS Chimera [11], a 3D phantom model was generated from Protein Data Bank (PDB) atomic coordinate data of the 50S ribosomal subunit. The simulated model was a 256 × 256 × 256 voxel array with isotropic voxel size of 1.7 Å/voxel. A 2D noise-free projection was obtained by taking the Radon transform of the phantom in a certain spatial angle. To construct a synthetic dataset, the noise-free projection was firstly contaminated with structural noise. The structural noise represents the irreproducible component of the specimen resulted from ice matrix, thin carbon film or incomplete particles [12]. Then, a mixture of Poisson and Gaussian noise was added to the result to represent the electron scattering statistics and CCD detector noise (see Fig. 1a–d). In each step, noise variance was determined in such a way that the final image shows some extent of similarity to the experimental EM projections. The SNR of the final synthetic image was ∼0.39. We also introduced random rotation in the range of [−1, 1] degree, and random translation of [−1, 1] pixel to the images to represent the alignment errors. Three random synthetic projection images are depicted in Fig. 1d–f. We generated three sets of projection images containing $N = 5$, 30 and 100 micrographs.

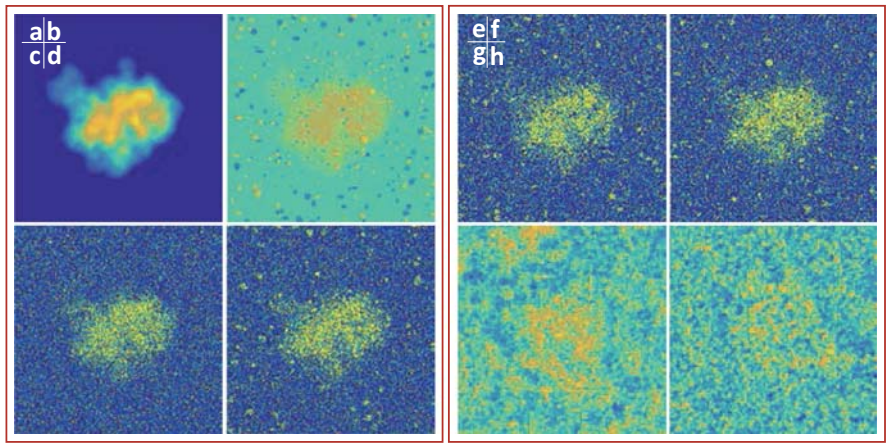

Fig. 1. (a)–(d) Steps of generating a synthetic particle image: (a) 256 × 256 noise-free projection image. (b) Structural noise represents the irreproducible component of the specimen; we added the structural noise to the noise-free projection image before image formation. (c) Noise-free projection image is contaminated with mixture of Poisson and Gaussian noise. (d) Synthetic projection image resulted from contaminating (b) with mixture of Poisson and Gaussian noise; SNR of the synthetic particle images is ∼0.39. (e), (f) 2 random particle images of the synthetic dataset. (g), (h) 2 random particle images of the experimental dataset.

2.1.2 Experimental Data

In order to evaluate the effect of the proposed merging approach on real data, we examined the method on the previously published cryo-EM dataset. The dataset is comprised of 82,575 images of the 50S ribosomal subunit [13]. The images are 100 × 100 pixels with isotropic pixel size of 3.26 Å/pixel. They were CTF-corrected with ACE2, a variation of the ACE1 [14] algorithm. A subset of 10,000 images was randomly selected from the original dataset. Two random projection images are shown in Fig. 1g, h. The 2D translations and the 3D projection angles of the selected particle images were estimated by a reference-based method using rotation-free cross-correlation. The reconstruction result in the cryo-EM dataset was low-pass filtered to 70 Å and used as the reference model. The particle images were classified into 196 classes. In each class, projections are sorted in a descending order based on their consistency with the reference image. We used classes with large number of particle images (over 200 projections) for our experiments.

2.2 Class Averaging Methods

2.2.1 Class Averaging with Conventional Wiener Filter in SPR

Defining a set of N images representing different realizations of the particle images in the same spatial orientation, and considering the additive noise model, the image formation in the Fourier domain can be expressed as:

$$Y^i(\omega) = \mathrm{CTF}^i(\omega) \times \left(M(\omega) + N^i_{strc}(\omega)\right) + N^i_{img}(\omega), i = 1, 2, \ldots, N \tag{1}$$

where ω is a 2D Fourier coordinate and $Y^i(\omega)$ is the i^{th} image of the set. $M(\omega)$ is the signal of interest common to all images, $N^i_{strc}(\omega)$ is the structural noise related to the fluctuations from the sample itself, $N^i_{img}(\omega)$ is the image noise from the measurement process and $\mathrm{CTF}^i(\omega)$ is the contrast transfer function of the i^{th} micrograph. In the continuation, we consider two assumptions: (1) both structural and image noise is considered with an overall term $N^i(\omega)$ [9]; and (2) images are CTF corrected, so that we define CTF = 1. Then, Eq. (1) can be simplified as:

$$Y^i(\omega) = M(\omega) + N^i(\omega). \tag{2}$$

Defining the estimated signal by the Wiener filter as $M(\omega)$, we have:

$$\widehat{M}(\omega) = \sum\nolimits_i W(\omega) Y^i(\omega), \tag{3}$$

$$W(\omega) = \frac{1}{N + 1/\mathrm{SSNR(R)}}. \tag{4}$$

Here, $W(\omega)$ is the Wiener filter coefficients and R is the annulus corresponding to the radial frequency in the Fourier domain [15]. Averaging all the projection images to provide a good estimation for SSNR in Eq. (4), we write:

$$SSNR(R) = \frac{\sum_R \sum_{i=1}^{N} |Y^i(\omega)|^2}{\sum_R \sum_{i=1}^{N} \left| Y^i(\omega) - \frac{1}{N} \sum_{i=1}^{N} Y^i(\omega) \right|^2}. \tag{5}$$

In a previous study, SSNR was divided by a coefficient $f_{particle}$ to optimize the Wiener filter considering only the particle and not the whole image. $f_{particle}$ is defined as the fraction of the image containing the particle [9]. In our implementation of conv-Wiener filter, we also employed $f_{particle}$ in the SSNR calculations.

2.2.2 Class Averaging with Local Adaptive Wiener Filter in SPR

In order to focus on the local regions in the image plane, we extract overlapping blocks with size $s \times s$ in one-pixel-sliding manner in the spatial domain. We treat the set of extracted sub-images independently [16]. To implement the local adaptive Wiener filter (LA-Wiener filter), we can reformulate Eqs. (3)–(5) as:

$$\mathrm{SSNR_{s,x}(R)} = \frac{\sum_R \sum_{i=1}^{N} \left| \mathrm{FT}(y^i_{s,x}) \right|^2}{\sum_R \sum_{i=1}^{N} \left| \mathrm{FT}(y^i_{s,x}) - \frac{1}{N} \sum_{i=1}^{N} \mathrm{FT}(y^i_{s,x}) \right|^2}, \tag{6}$$

$$\hat{\mu}_{s,x} = \mathrm{FT}^{-1} \left(\frac{\sum_{i=1}^{N} \mathrm{FT}(y^i_{s,x})}{N + \frac{1}{\mathrm{SSNR_{s,x}(R)}}} \right), \tag{7}$$

where, FT stands for Fourier transform, $y^i_{s,x}$ denotes an $s \times s$ block, centered at spatial location x of the image y^i in the spatial domain. $\mathrm{SSNR_{s,x}}$ and $\hat{\mu}_{s,x}$ are the SSNR and signal estimate of each block, respectively. After denoising all the blocks separately, they are concatenated to reconstruct the whole image, in which overlapping regions of the blocks are averaged.

2.3 Numerical Analysis Method

Numerically evaluating the quality of the synthetic class averages, we calculated reference-based Fourier ring correlation ($\mathrm{FRC_{ref}}$): the noise-free particle image (Fig. 1a) is the reference image. For the numerical analysis of the experimental data, we used even/odd FRC ($\mathrm{FRC_{e/o}}$) analysis. Therefore, as the particle images of each class are sorted based on their consistency with the reference model, they are divided into even/odd half-sets. The class average of each half-set is calculated and the consistency between the results is calculated by the $\mathrm{FRC_{e/o}}$ curves [17].

3 Results and Discussion

In order to compare LA-Wiener filter with the conventional method of class averaging, we analyzed the result of merging different number of synthetic projection images by means of visual and numerical analysis. The study is extended into the experimental dataset for different number of projections, classes and window sizes.

3.1 Synthetic Dataset

Results of merging 5, 30, and 100 particle images with conv- and LA-Wiener filter are shown in Fig. 2. The window size of 3 × 3 is selected for LA-Wiener filter. Visual impression of the resultant images indicate that the proposed method is better than conv-Wiener filter in all cases. Increasing the number of images, results of LA-Wiener filter are smoother and at the same time contain sharper edges. For instance, the boundary of the L1 stalk of the 50S ribosome is distinguishable from the solvent only with 30 particle images, when LA-Wiener filter is used. The numerical analysis of the results is also in line with the visual impression. The FRC_{ref} curves are measured compared to the noise free projection shown (i.e. ground truth) in Fig. 2. Considering the pixel size as 1.7 Å/pixel and 0.5 cut-off frequency, our proposed method gains at least 2 Å higher resolution compared to conv-Wiener filter for different number of projection images.

3.2 Experimental Dataset

We compared the result of merging different number of particle images ($N_{half\text{-}set}$ = 3, 10, 30, 50 and 100) with conv- and LA-Wiener filter for one class of the experimental dataset. The results are presented in Fig. 3. The window size of 3 × 3 is selected for LA-Wiener filter. Visual evaluation of the results indicate that LA-Wiener filter outperforms the conventional method for all cases, as it does in the synthetic experiment. The performance of LA-Wiener filter enhances considerably by increasing the number of projections. The images merged with LA-Wiener filter are less noisy and the edges were preserved better compared to the conventional merging method. For the numerical analysis, projection images of this class are divided into half-sets and $FRC_{e/o}$ is calculated for each case. Considering 0.5 cut-off frequency and the pixel size of 3.26 Å/pixel, the proposed method gains ∼0 Å, ∼1.5 Å, ∼2 Å, ∼3–4 Å and ∼4–5 Å better resolution compared to conv-Wiener filter for $N_{half\text{-}set}$ = 3, 10, 30, 50 and 100, respectively. In Fig. 4, the superiority of LA-Wiener (window size of 3 × 3) compared to the conventional method is extended to 5 different classes for a fixed number of projection images ($N_{half\text{-}set}$ = 30). Visual impression and $FRC_{e/o}$ measurements of the results indicate that LA-Wiener filter is better than conv-Wiener filter at least by 2 Å for all classes. To evaluate the performance of LA-wiener more thoroughly, all the classes containing over 200 projections (19 classes) were analyzed. From each class, the first 6, 30, and 100 particle images were divided into half-sets ($N_{half\text{-}set}$ = 3, 15, 50). The consistency between resultant merged images of the half-sets were analyzed by $FRC_{e/o}$. Considering the 0.5 cut-off frequency and the pixel size of 3.26 Å/pixel, Fig. 5 plots the

behavior of conv- and LA-Wiener filter in a compact representation. The results indicate that the LA-Wiener filter performs better for all classes: for lower number of images, LA-Wiener filter performs slightly better than conv-Wiener filter, however, increasing the number of projections, considerably enhances the performance of LA-Wiener filter almost for all classes.

The effect of the window size on LA-Wiener filter, for a fixed number of projection images ($N_{half\text{-}set} = 30$) in a single class is shown in Fig. 6. We examined window size of 3×3, 5×5, 7×7, 9×9, and 11×11. The results indicate that enlarging the window

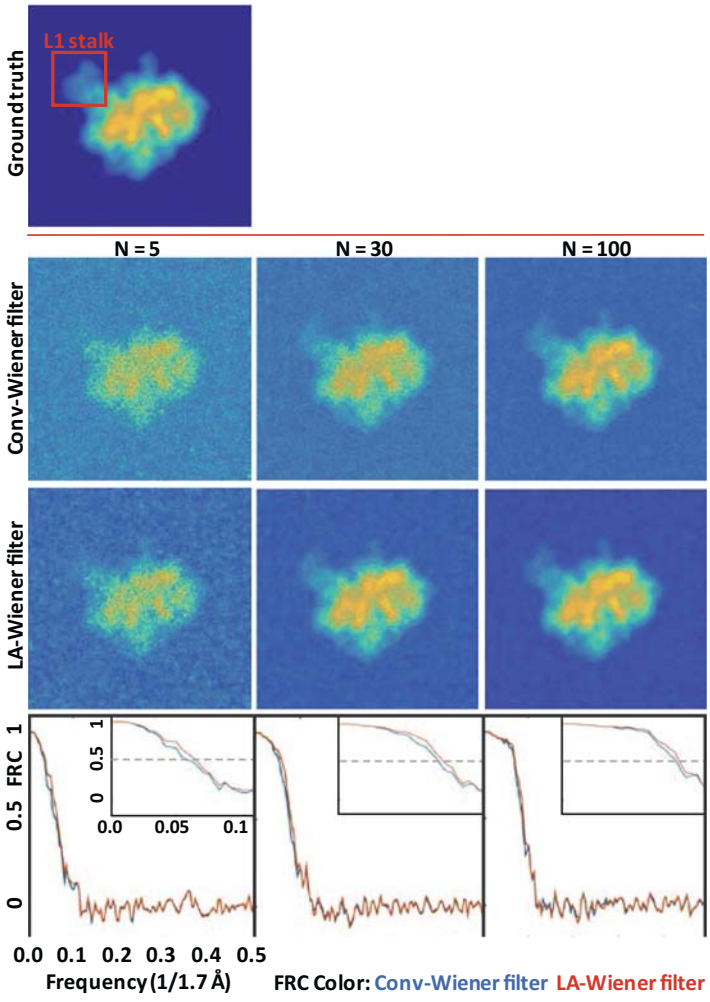

Fig. 2. Visual and numerical analysis of merging different number of projection images from the synthetic dataset. The visual impression of merging N = 5, 30 and 100 particle images indicates that LA-Wiener filter performs better than conv-Wiener filter in denoising and preserving the edges. LA-Wiener filter defines the boundary of the L1 stalk when only 30 projection images are used. Considering 0.5 cut-off frequency and 1.7 Å/pixel, LA-Wiener filter gains at least ~2 Å better resolution compared to conv-Wiener filter.

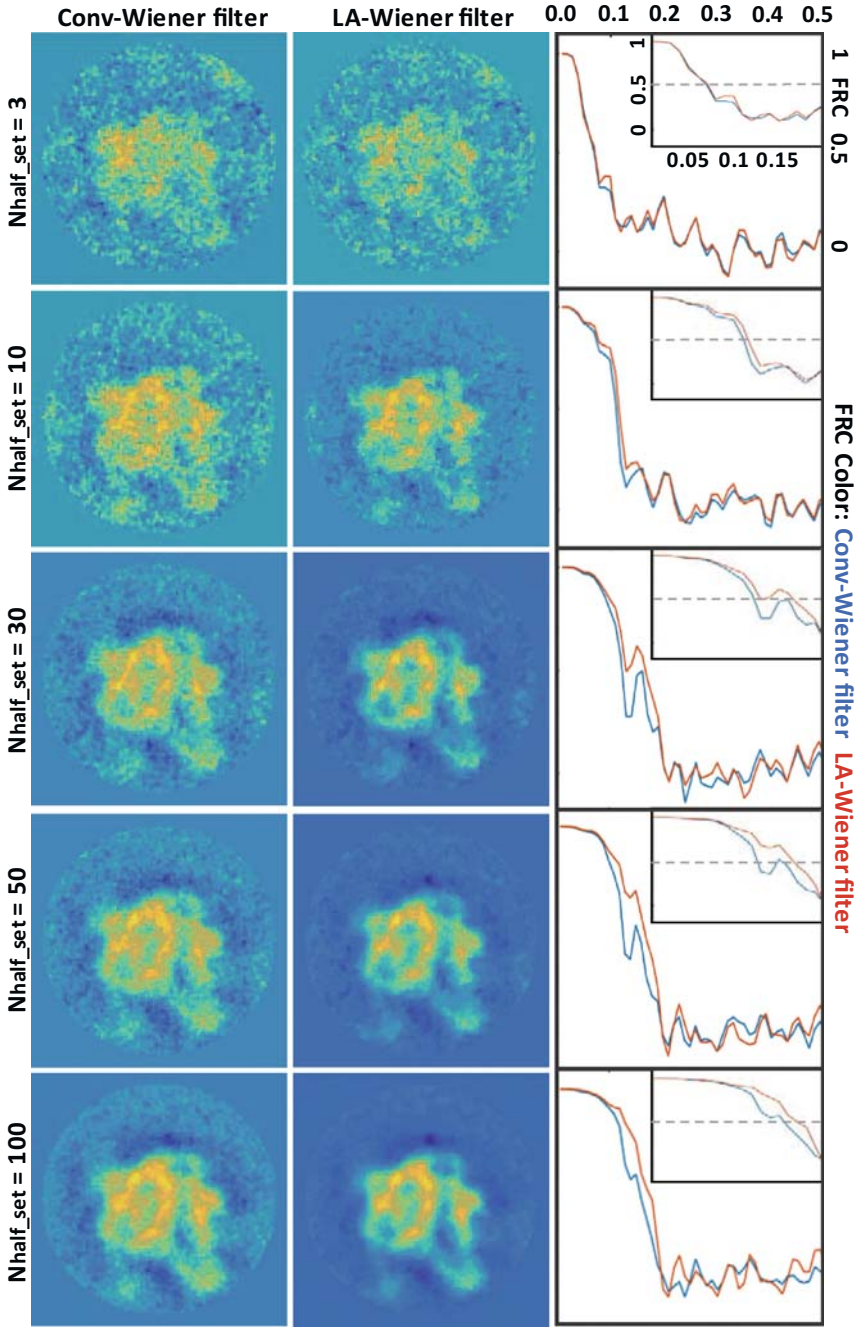

Fig. 3. Visual and numerical analysis of merging different number of projection images from the experimental dataset. The visual impression of merging $N_{half\text{-}set}$ = 3, 10, 30, 50 and 100 projection images of one class indicates that LA-Wiener filter performs better than conv-Wiener filter. Considering the pixel size of 3.26 Å/pixel, the $FRC_{e/o}$ curves imply that LA-Wiener filter gains at least ∼0 Å, ∼1.5 Å, ∼2 Å, ∼3–4 Å and ∼4–5 Å better resolution compared to conv-Wiener filter for $N_{half\text{-}set}$ = 3, 10, 30, 50 and 100, respectively.

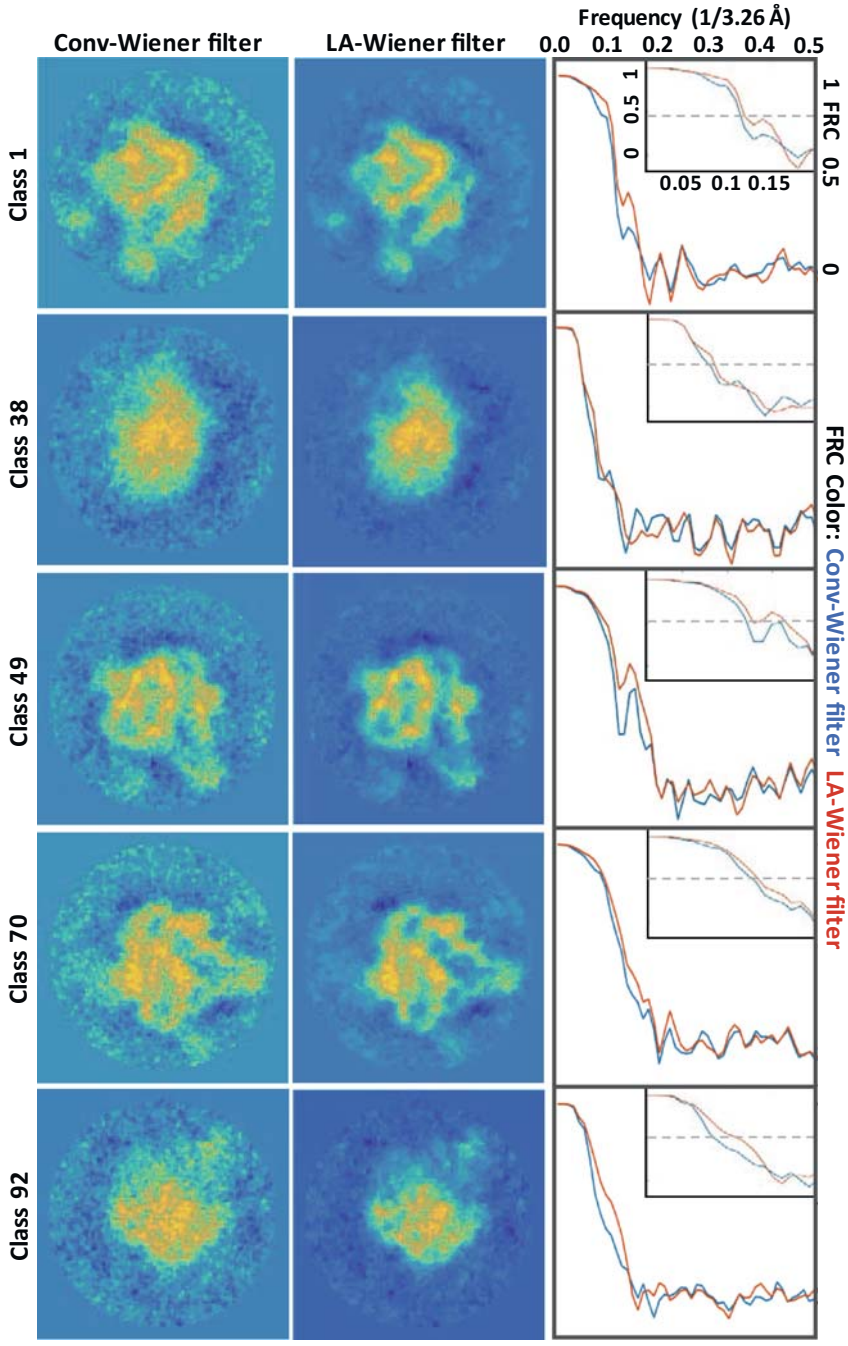

Fig. 4. Visual and numerical analysis of merging $N_{half\text{-}set}$ = 30 projection images for different classes of the experimental dataset. The results of merging 30 projection images by conv- and LA-Wiener filter for different classes indicate that LA-Wiener filter performs better than the conventional implementation of the Wiener filter. Considering 0.5 cut-off frequency and pixel size of 3.2 Å/pixel, LA-Wiener filter gains $\sim$2 Å better resolution compared to conv-Wiener filter in all classes.

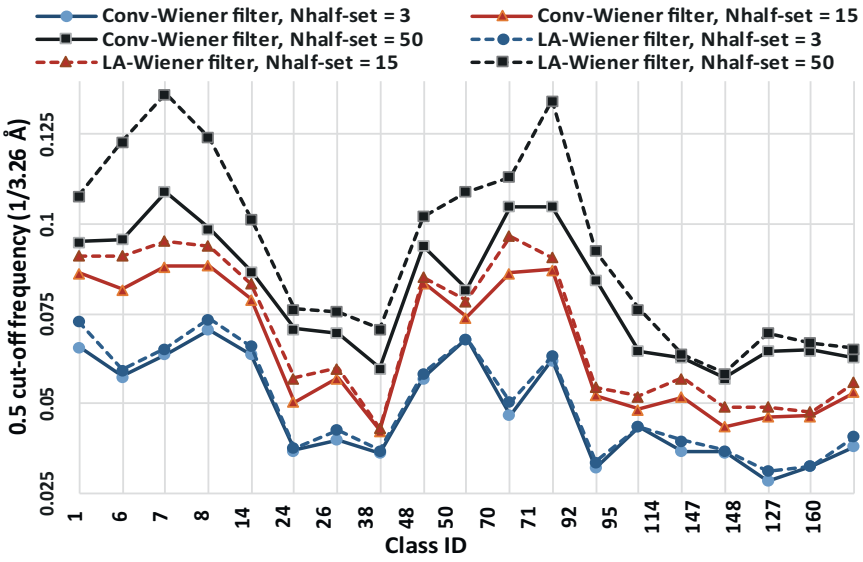

Fig. 5. $FRC_{e/o}$ 0.5 cut-off frequency of conv- and LA-Wiener filter for different number of projection images and classes. The results for $N_{half\text{-}set}$ = 3, 15, and 50 particle images in 19 classes indicate that LA-Wiener filter outperforms the conventional approach in class averaging. Increasing the number of particle images boosts the performance of LA-Wiener filter.

size smooths the merged particle images without preserving the edges. The $FRC_{e/o}$ curves verify the visual impression as well. Increasing the window size, enhances the consistency in low frequencies ($<\sim 0.1/3.26$ Å), while declines the consistency in medium frequencies ($\sim 0.1/3.26$ Å < frequency < $\sim 0.2/3.26$ Å).

The selection of the window size is a compromise between the bias and variance of the estimation. We determined the proper window size based on visual assessment and overall behavior of the FRC curves. A large moving window oversmooths the results in which some details will be lost, i.e. high bias, since regions with different statistical characteristics are enclosed in one frame. On the other hand, applying a very small window size means not to include adequate partition of the signal inside the window. In such a case, the output of LA-Wiener filter contains high variance [16]. Our study agrees with this conclusion, as the results of merging with window size of 3×3 contains lower bias and higher variance compared to the results of 11×11 window size. In practice, the quality of the micrographs determines how to compromise between the bias and variance of the estimation, and so the window size. Noisier projections require larger windows to generate smoother class averages (Fig. 6).

The computational time of the algorithm increases with the increment of the image size, number of the particle images and the size of the sliding window. Using 4-core Intel CPU 3.41 GHz machine with 64 GB RAM, processing time of LA-Wiener filter in MATLAB for 30 synthetic particle images of size 256×256 with window size of 3×3 and 5×5 is 7.5 and 8.3 s, respectively.

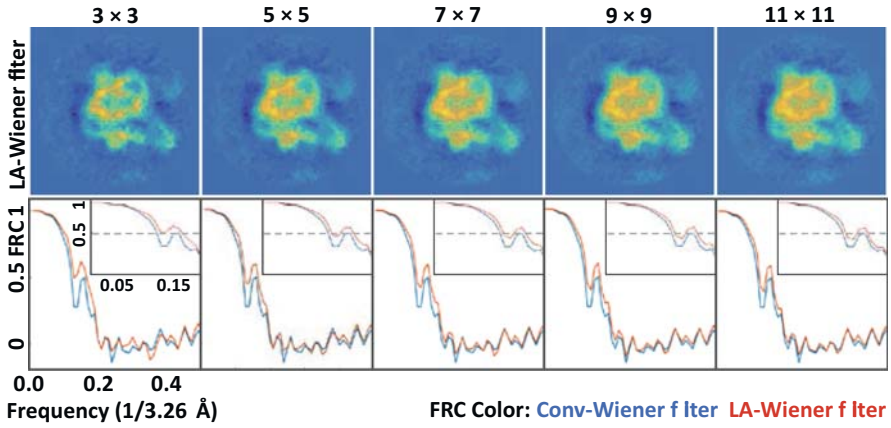

Fig. 6. Effect of window size on LA-Wiener filter. Window size of 3×3, 5×5, 7×7, 9×9 and 11×11 is assessed for a fixed number of projection images ($N_{half\text{-}set} = 30$) in a single class. The results indicate that increasing the window size of LA-Wiener filter blurs the merged particle images. The $FRC_{e/o}$ curves are in line with the visual impression: enlarging the window size enhances the consistency in low frequencies ($< \sim 0.1/3.26$ Å), while declines the consistency in medium frequencies ($\sim 0.1/3.26$ Å $<$ frequency $< \sim 0.2/3.26$ Å).

4 Conclusion

In this paper, we introduced LA-Wiener filter for merging a set of cryo-EM images in the class averaging step of SPR. To reformulate conv-Wiener filter, we considered local minimization of the mean-squared error by employing a sliding window throughout the image plane. As statistical properties exhibit more homogeneity in smaller blocks compared to the whole image, LA-Wiener filter performs more accurately compared to the conventional implementation of the Wiener filter. We verified the superiority of our proposed method for both synthetic and experimental datasets, when different number of projection images are included and for different classes to show its application for variety of cases in cryo-EM.

References

1. Frank, J.: Three-Dimensional Electron Microscopy of Macro-molecular Assemblies: Visualization of Biological Molecules in Their Native State. Oxford University Press, New York (2006)
2. Reimer, L., Kohl, H.: Transmission Electron Microscopy Physics of Image Formation. Springer, New York (2008)
3. Kuan, D.T., Sawchuk, A.A., Strand, T.C., Chavel, P.: Adaptive noise smoothing filter for images with signal-dependent noise. IEEE Trans. Pattern Anal. Mach. Intell. **7**, 165–177 (1985)
4. Lee, J.S.: Digital image enhancement and noise filtering by use of local statistics. IEEE Trans. Pattern Anal. Mach. Intell. **2**, 165–168 (1980)

5. Unser, M., Trus, B.L., Steven, A.C.: A new resolution criterion based on spectral signal-to-noise ratios. Ultramicroscopy **23**, 39–51 (1987)
6. Grigorieff, N.: FREALIGN: high-resolution refinement of single particle structures. J. Struct. Biol. **157**, 117–125 (2007)
7. Zeng, X., Stahlberg, H., Grigorieff, N.: A maximum likelihood approach to two-dimensional crystals. J. Struct. Biol. **160**, 362–374 (2007)
8. Tang, G., Peng, L., Baldwin, P.R., Mann, D.S., Jiang, W., Rees, I., Ludtke, S.J.: EMAN2: an extensible image processing suite for electron microscopy. J. Struct. Biol. **157**, 38–46 (2007)
9. Sindelar, C.V., Grigorieff, N.: An adaptation of the Wiener filter suitable for analyzing images of isolated single particles. J. Struct. Biol. **176**, 60–74 (2011)
10. Jin, F., Fieguth, P., Winger, L., Jernigan, E.: Adaptive Wiener filtering of noisy images and image sequences. In: International Conference on Image Processing, pp. III-349–III-352. IEEE (2003)
11. Pettersen, E.F., Goddard, T.D., Huang, C.C., Couch, G.S., Greenblatt, D.M., Meng, E.C., Ferrin, T.E.: UCSF Chimera—a visualization system for exploratory research and analysis. J. Comput. Chem. **25**, 1605–1612 (2004)
12. Baxter, W.T., Grassucci, R.A., Gao, H., Frank, J.: Determination of signal-to-noise ratios and spectral SNRs in cryo-EM low-dose imaging of molecules. J. Struct. Biol. **166**, 126–132 (2009)
13. Voss, N.R., Lyumkis, D., Cheng, A., Lau, P.W., Mulder, A., Lander, G.C., Brignole, E.J., Fellmann, D., Irving, C., Jacovetty, E.L., Leung, A., Pulokas, J., Quispe, J.D., Winkler, H., Yoshioka, C., Carragher, B., Potter, C.S.: A toolbox for ab initio 3-D reconstructions in single-particle electron microscopy. J. Struct. Biol. **169**, 389–398 (2010)
14. Mallick, S.P., Carragher, B., Potter, C.S., Kriegman, D.J.: ACE: automated CTF estimation. Ultramicroscopy **104**, 8–29 (2005)
15. Saxton, W.O.: Computer Techniques for Image Processing in Electron Microscopy. Academic Press Inc., New York (1978)
16. Lim, J.S.: Image restoration by short space spectral subtraction. In: IEEE International Conference on Acoustics, Speech, and Signal Processing, pp. 191–197. IEEE (1980)
17. Cardone, G., Grünewald, K., Steven, A.C.: A resolution criterion for electron tomography based on cross-validation. J. Struct. Biol. **151**, 117–129 (2005)

Tampereen teknillinen yliopisto
PL 527
33101 Tampere

Tampere University of Technology
P.O.B. 527
FI-33101 Tampere, Finland

ISBN 978-952-15-4134-6
ISSN 1459-2045